To the Graduate Council:

I am submitting herewith a thesis written by Satyam Anil Mistry entitled "Flow Control Over an Airfoil Using Synthetic Jet." I have examined the final paper copy of this thesis for form and content and recommend that it be accepted in partial fulfillment of the requirements for the degree of Master of Science, with a major in Aerospace Engineering.

Dr. Kivanc Ekici, Major Professor

We have read this thesis
and recommend its acceptance:

Dr. Kivanc Ekici

Dr. Trevor Moeller

Dr. Zhili Zhang

Accepted for the Council:

Dr. Dixie L. Thompson

Vice Provost and Dean of the Graduate School

To the Graduate Council:

I am submitting herewith a thesis written by Satyam Anil Mistry entitled "Flow Control Over an Airfoil Using Synthetic Jet." I have examined the final electronic copy of this thesis for form and content and recommend that it be accepted in partial fulfillment of the requirements for the degree of Master of Science, with a major in Aerospace Engineering.

Dr. Kivanc Ekici, Major Professor

We have read this thesis
and recommend its acceptance:

Dr. Kivanc Ekici

Dr. Trevor Moeller

Dr. Zhili Zhang

Accepted for the Council:

Dr. Dixie L. Thompson

Vice Provost and Dean of the Graduate School

(Original signatures are on file with official student records.)

Flow Control Over an Airfoil Using Synthetic Jet

A Thesis Presented for

Master of Science

Degree

The University of Tennessee, Knoxville

Satyam Anil Mistry

August 2023

Acknowledgements

I want to express my gratitude to my advisor Dr. Kivanc Ekici for his humble guidance and the great care he provided throughout my studies at the University of Tennessee. Along with that, I would also like to thank my co-advisor Dr. Reza Djeddi who provided his guidance initially as I embarked on my thesis journey. Your knowledge and expertise have inspired me to pursue my goals with dedication and enthusiasm. Thank you for challenging me to think critically and encouraging me to explore new ideas and perspectives.

I want to thank my committee members Dr. Trevor Moellor and Dr. Zhili Zhang who have contributed their time, expertise, and valuable insights to the success of this project. Their suggestions and criticism were extremely helpful in determining the project's course and assuring its quality. I am appreciative of the chance to have collaborated with such a talented and dedicated group of individuals.

I am deeply grateful to my grandmother, Laxmiben Mistry, and my parents, Anil and Nayana Mistry, for always supporting me in whatever way they can. I am truly in your debt for providing me with your unconditional love and support while motivating me to achieve great heights. I hope I have made you proud and I will never forget the hardships and struggles you went through so your children can be successful.

I would like to thank my brother, Deep Mistry, for always motivating and challenging me to reach my goals. I really appreciate for always staying by my side through my ups and downs and never giving up on me. I will always remember the great memories we shared and you are the best brother anyone could ask for.

I would like to appreciate Allison Carroll, whose unwavering support and encouragement have been instrumental in helping me achieve my goals. Throughout this journey, Allison has always provided insightful advice and feedback whenever I needed it. Her positivity and enthusiasm have been a driving force behind my success, and I am deeply grateful for her friendship.

I am thankful for all the professors and mentors I had throughout high school and college whose guidance and support have been instrumental in shaping my academic and professional journey.

I would like to thank Julie Knoefel for assisting me throughout my journey in graduate school. Also, thank you for always cheering me on whenever I would stop by your office. I will really miss having conversions about the Good 'Ole Rocky Top with you.

Lastly, I would like to thank all my friends for all the cherished times we have spent together. I am grateful for the laughter, the good times, and the memories that we have shared. Their love and support have been an essential source of strength, and I am blessed to have such amazing friends in my life.

Abstract

In this study, unsteady, turbulent flow over NACA 0015 was analyzed using synthetic jets. The study focused on applying the numerical method using the commercial CFD solver Ansys Fluent. The synthetic jet simulation was carried out for Re = 896,000 for two angles of attack: 10 and 14 degrees. The optimal jet amplitude and jet frequency were determined from a range of amplitudes of 2.0 to 4.0 and frequencies of 0.4 Hz to 1.2 Hz while the jet location, jet angle, and jet width were fixed. The results showed that for both jet angles, the optimal amplitude and frequency were 4.0 and 0.8 Hz, respectively. As the amplitude was increased, the lift-to-drag ratio went up, but the variance in frequency did not impact the aerodynamic coefficients. The flow separation was observed at various instances for the synthetic jet, which showed that when suction was applied the separation was delayed, and the opposite was true for injection. On average, the separation was delayed for both angles with the use of a synthetic jet. Additionally, the impact of steady injection and suction jets was examined. The results were similar to before where the injection jet did not improve the force characteristics, but suppression increased the lift-to-drag ratio by 53.91% for the 10-degree case and 42.40% for the 14-degree case. The separation location remained the same for the injection jet at 10 degrees. However, with the suction jet, the flow did not separate. In the post-stall angle case, both steady injection and suction delayed separation.

Table of Contents

List of Tables

List of Figures

Nomenclature

A	jet amplitude
C	chord
C_D	drag coefficient
C_i	constant
C_L	lift coefficient
C_P	pressure coefficient
CFD	Computational Fluid Dynamics
D	drag force
d	distance from wall
dt	physical time step size
DBD	Dielectric Barrier Discharge
F	jet frequency
f_i	function
g	gravity; constant
GPU	Graphics Processing Unit
GUI	Graphics User Interface
HPC	High Performance Computing
I	unit tensor
ICE	Innovative Control Effectors
k	turbulent kinetic energy
L	lift force
LES	Large Eddy Simulation
M	Mach number
$NACA$	National Advisory Committee for Aeronautics

p	pressure
Re	Reynolds number
S	magnitude of the vorticity
$SIMPLEC$	Semi Implicit Method for Pressure Linked Equation - Consistent
SST	Shear Stress Model
T	period
t	time
U_∞	freestream velocity
$\vec{u}$	velocity vector
u_{jet}	jet velocity
u, v, w	velocity components
x, y, z	Cartesian coordinates
$ZNMF$	Zero Net Mass Flux
α	angle of attack
β	angle between freestream and local jet surface
ϵ	turbulent dissipation rate
θ	jet angle
μ	dynamic viscosity
$\tilde{\nu}$	eddy viscosity variable
ρ	density
$\vec{\vec{\tau}}$	viscous stress tensor (normal and shear stress)
Ω	mean rotation rate tensor
ω	rate of dissipation per unit turbulent kinetic energy

Subscripts

b	basic
i, j, k	nodal point index
L	laminar
T	turbulent
v	viscous
w	wall
∞	freestream

Superscripts

T	transpose

Chapter 1: Introduction

Over the past few decades, the ability to understand aerodynamic flow control and its implementation in various applications has significantly increased. The applications extend from the military to civilian sectors, and the research for more improvements still remains of great interest. In 1904, Prandtl established flow control science by introducing the boundary layer theory, explaining the physics of separation, and describing various experiments in which a boundary layer was controlled. In the next few decades, stimulated by the war, flow control played a key role in accomplishing the requirement of developing quick, highly maneuverable, efficient aircraft, missiles, ships, submarines, and torpedoes. In the late 1900s, there was a shift from military to civilian applications, and the availability of fast and inexpensive computers made it possible to solve problems numerically [7].

One may ask why engineers want to control the flowfield. Well, some of the benefits of flow control include drag reduction, lift improvement, mixing enhancements, and noise mitigation [8, 9]. There are two distinct techniques used to control fluid flow in a variety of applications: passive and active flow control. Many of the earlier works that focused on flow optimization used passive techniques. The term "passive flow control" refers to the modification of fluid flow without the need for external energy input by the use of geometric parameters or surface coatings. Because of its low cost, flexibility, and success in a range of applications, this technology has attracted a lot of interest recently. These include morphing the airfoil geometry, adding vortex generators and riblets, or adding porous coatings that change the pressure gradient thereby delaying turbulence and preventing flow separation over the airfoil's upper surface [10–13]. Some examples of passive flow techniques can be seen in Figure 1.1.

On the other hand, active flow control involves the use of external energy sources to manipulate the fluid flow. More discussion on active flow control can be found in the next section.

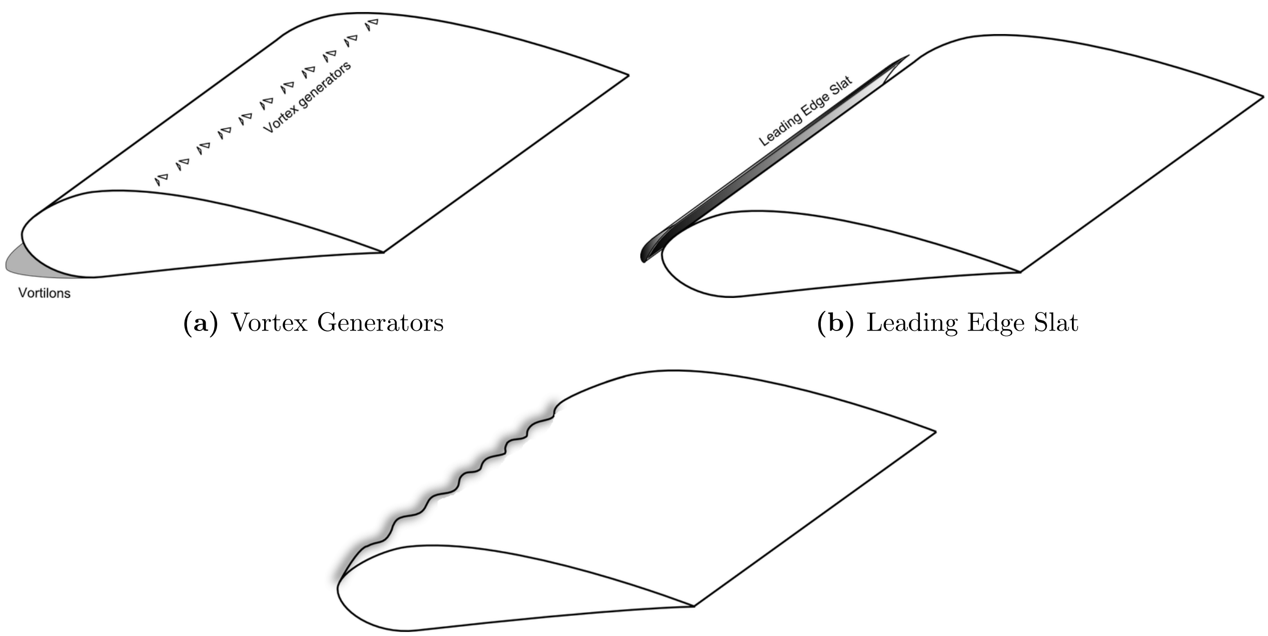

(a) Vortex Generators

(b) Leading Edge Slat

(c) Shape Deformation

Figure 1.1: Passive Flow Control Techniques [1]

1.1 Active Flow Control

Fluid mechanics research on active flow control aims to modify the behavior of fluid flow using actuators and other external devices. Enhancing fluid systems' effectiveness, functionality, and energy usage is the aim of active flow control. This method has been used in several applications, including fuel injectors, heat exchangers, wind turbines, and aircraft wings, to name a few. In recent years, active flow control has gained significant interest due to its ability to reduce energy consumption and emissions, increase aerodynamic efficiency, and extend the lifespan of mechanical components. Additionally, active flow control has been shown to suppress noise making it an attractive option for various industries.

Some of the active flow control techniques include steady and oscillating jets, plasma actuators, and synthetic jets. Steady jets are used to produce a continuous flow in a specific direction while oscillating jets are used to produce periodic disturbances in the fluid flow. A diagram of the two actuators can be seen in Figure 1.2. Out of the two jets, studies have shown that the fluid oscillators are superior in performance compared to steady jets with respect to given parameters [2]. Another technique uses weakly ionized plasma actuators. These actuators are made up of electrodes that are attached to the surface of the airfoil. The electrodes are supplied with high-voltage alternating current, which weakly ionizes the air around them. A body force vector operating on the external flow caused by the ionized air (plasma) and the electric field gradient created by the electrodes might generate a constant or erratic velocity component [14]. An application of the plasma actuator on a NACA 4415 airfoil is depicted in Figure 1.3. Lastly, synthetic jets are a particular kind of fluid flow produced by rotating a membrane or diaphragm inside a fluid-filled chamber. Synthetic jets, in contrast to conventional jets, provide a pulsed or oscillatory flow that is programmable and controllable rather than relying on constant flow of fluid. An oscillating diaphragm, which induces a sequence of vortices that are alternately expelled and drawn back into the cavity, produces the fluid pulses. These fluid pulses emerge through a tiny opening. The

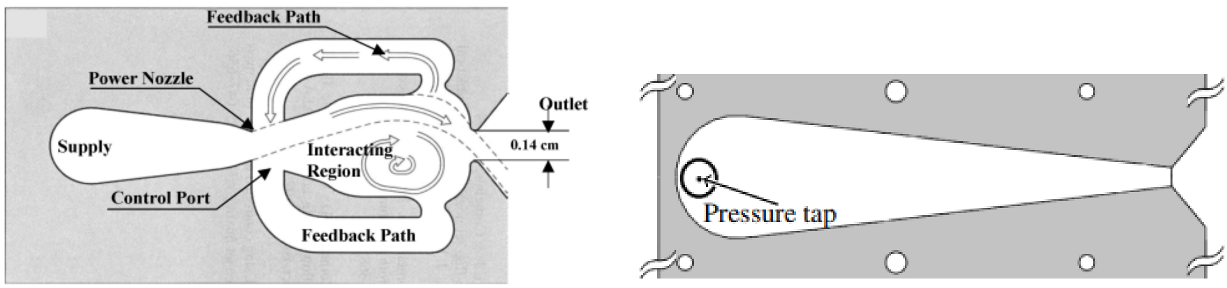

(a) Oscillating Jet **(b)** Steady Jet

Figure 1.2: Sketch of Actuators [2, 3]

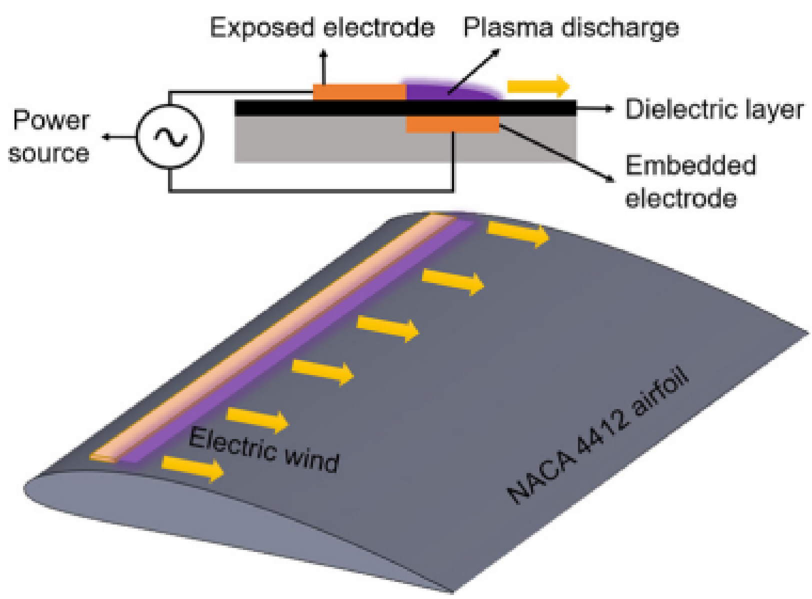

Figure 1.3: Schematic of Plasma Actuator [4]

fluid stream produced by these pulses can be utilized to improve heat transfer or to control the flow around a surface [15]. Figure 1.4 illustrates a typical synthetic jet device.

There are several advantages of using active flow control techniques instead of passive flow control. First, active flow control can be used to enhance efficiency and consume less energy by increasing lift and decreasing the drag on an object's surface. If one considers that even a 1% reduction in global aircraft fuel consumption is worth around 1.25 million dollars per day in direct operational costs (in 2002), the prospect of boosting efficiency and simplifying hydraulically operated systems (such as high-lift systems) is highly alluring [16]. Because of this, lowering the average overall drag by just a few percent could result in annual savings of several billion dollars, have a substantial positive impact on the environment, and allow for greater speed, range, and endurance. Next, using active flow control flow noise may be reduced, which can be very useful in aircraft and transportation applications. For example, Koop et. al. [17] investigated the possibility of reducing noise at the flap side edge by blowing air into the vortical flow structure. The flow visualization at the flap side edge revealed that the vortical structure becomes quite complex and unstable in the absence of flow control. This supported the notion that the flap side-edge vortex dominates the mechanism for sound generation. The vortex was no longer visible in the velocity field when the flow control is activated, and the vorticity is nearly entirely dispersed. Lastly, active flow control can improve the stability of fluid systems by reducing turbulence and can increase the maneuverability of fluid systems by controlling the flow. Neistroy et. al. [18] examined the active flow effector-equipped ICE-101 tailless aircraft. During periods of light or moderate turbulence, or periods of light turbulence combined with light or moderate discrete gusts, the control effectors in this ICE design offer stabilizing forces and moments.

Even though there are many advantages to active flow control, there are also many challenges that arise with active flow control. One of the main challenges is that this technique may require significant amounts of power to operate, which can be a limitation in some of the applications. For instance, plasma actuators require high-voltage power supplies,

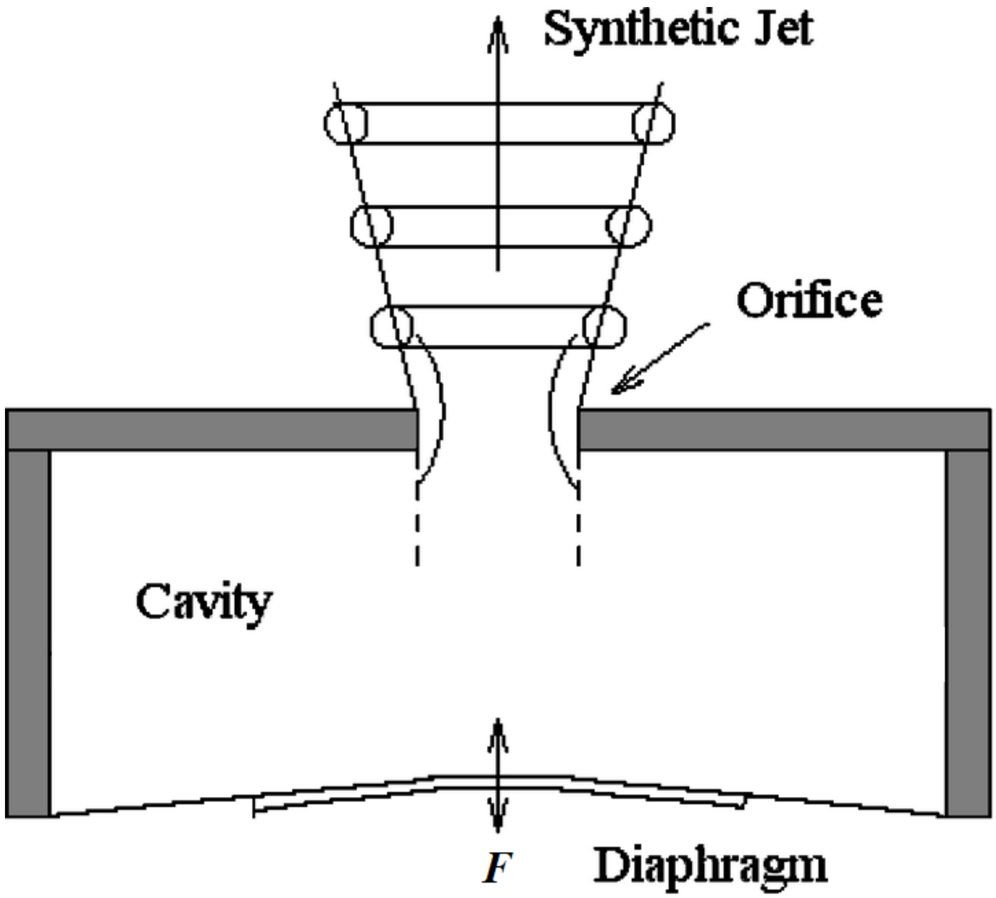

Figure 1.4: Schematic of Synthetic Jet Actuator [5]

which can be expensive and difficult to implement in some systems. A dielectric barrier discharge (DBD) plasma actuator with a dielectric layer of 0.3 mm, 0.6 mm, and 1.12 mm thickness of Katpon consumes 17 Watts, 38 Watts, and 6 Watts of power, respectively, for a peak-to-peak voltage of 7 kV [19]. This is a significantly high amount of voltage being used for the plasma actuator. Moreover, these DBD plasma actuators decrease in performance, or are even subject to failure, in relatively high humidity. Adverse conditions such as drizzle, dew, or dust make them less favorable in certain applications. Earlier publications show that relative humidity higher than 40% shows a reduction in actuator-induced thrust, and an increased friction coefficient (and thus the overall drag on the body) [20, 21]. Lastly, active flow control techniques can be complex and expensive to implement, particularly in large-scale systems. The complexity of modulated input signals needed to achieve closed-loop flow control goals has been shown to be a barrier to the widespread use of synthetic jet actuators for practical flight control [22].

Although active flow control techniques can be quite complex to implement and set up, numerical methods can reduce the complexity in the earlier stages. Early in the 1970s, computational fluid dynamics (CFD) emerged as a powerful method for simulating fluid flows by combining computer technology, applied mathematics, and physics. The modeling of transonic flows was made possible by the introduction of more powerful mainframes. The introduction of multigrid and other numerical acceleration techniques made it possible to compute inviscid flows inside the turbomachinery or past fully assembled aircraft designs. The focus shifted to the more challenging simulations of viscous flows governed by the Navier-Stokes equations, leading to the development of various turbulence models. Implicit approaches were developed to address flow problems such as the hypersonic flow past re-entry vehicles, which required accurate gas modeling. The modeling of combustion and steam condensation became essential for the development of efficient steam turbines and low-emission gas turbines, respectively. Grid generation techniques improved as the geometric complexity of arrangements grew. Unstructured grid generators and flow solvers promised faster setup times and solution-based grid adaptation. Nowadays, a wide range of disciplines, including architecture, meteorology, oceanography, astronomy, biology, oil recovery, aerospace, turbomachinery, automobiles, and ships, frequently employ CFD methodologies [23]. Despite its advancements, CFD still has a lot of challenges, including modeling turbulence and combustion, heat transfer, effective methods for solving viscous flows, and automated grid generators. CFD, however, presents fresh possibilities for design optimization. Due to these reasons, a numerical approach has been employed in this study.

1.2 Literature Survey

Over the past couple of decades, there have been numerous studies in active flow control. Both experimental and computational studies, especially those relating to injection, suction, and/or synthetic jet over the airfoils have been highlighted in this section.

Huang et. al. [24] examined the flow control over the NACA 0012 at an angle of attack of 18 degrees at Re = 500,000 using injection and suction techniques at the leading and trailing edges. Three different parameters, jet location, amplitude, and angle, were investigated over a wide range. In contrast to injection, suction was shown to increase lift by forming an extended pressure (C_p) zone on the airfoil's upper surface. Blowing frequently was shown to decrease performance compared to baseline. Downstream blowing enhanced the properties of lift and drag, however, lower amplitudes were preferable. While small blowing amplitudes seem to be the best option for downstream tangential blowing, the ideal control amplitudes for perpendicular suction lie between 0.01 and 0.2. Perpendicular suction at the leading edge is superior to other suction circumstances for increasing the lift when location and angle factors are combined, while tangential injection at downstream locations is superior to other injection situations for boosting lift.

Yousefi et. al. [25] also numerically analyzed the effects of tangential and perpendicular blowing for the NACA 0012 airfoil at Re = 500,000 for various angles of attack. In that study, jet width and jet amplitude were varied. The results showed that when the blowing amplitude increases, the lift-to-drag ratio increases, and the separation point is moved downstream. This is also true for cases with an angle of attack greater than 10 degrees; for angles less than 10 degrees, it has a negative effect on the lift-to-drag ratio. The lift-to-drag ratio continually grows in the tangential blowing when the blowing jet width increases, and it continuously decreases in the perpendicular blowing when the blowing jet width increases. Finally, with tangential blowing conditions of 0.5 blowing amplitude, 4% jet width, and 18 degrees angle of attack, the lift-to-drag ratio was raised by 17%.

Liang et. al. [26] analyzed the flow with an injection jet on the upper surface of the NACA 0012 airfoil. This study was conducted by varying the jet amplitude (0.1, 0.3, and 0.5) and jet location (20%C, 50%C, and 80%C) at Re = 1,000,000 for angles of attack of 0, 10, 16, and 18 degrees. The results showed that a constant perpendicular blowing with a 0.1 blowing amplitude at 80%C is beneficial at angles of attack more than or equal to the stall angle. However, for angles of attack less than the stall angle, it had no benefit on the aerodynamic properties. Leading-edge injection enhances lift by creating bigger vortices and more circulation around the airfoil, but it also worsens the leading-edge pressure and detaches the flow. On the other side, downstream blowing can boost lift and decrease drag, but a lower amplitude is preferable since it has been observed that the lift and drag characteristics became worse when the blowing amplitude is raised beyond 0.1.

In another study, Djedjiga et.al. [27] investigated the injection jet flow control method at Re = 218,000 by studying the influence of jet angle (0, 30, and 45 degrees) and jet amplitude (from 0.1 to 1.0) for the NACA 4415 airfoil. The study also focused on the effects of suction and a combination of both injection and suction actuators. The results showed that for blowing, the lift-to-drag ratio increased with the amplitude. However, the opposite effect was noted when the jet angle was increased. The dual jet actuators performed better than the single jet for an amplitude of 0.1, and jet angle of 0 degrees, and delayed the stall from 14 degrees to 17 degrees. There were, nonetheless, less intuitive observations for the suction cases. For an amplitude of 0.1 and an angle of 0 degrees, the lift-to-drag ratio was lower than the one with injection, and for stall and post-stall angles, the ratio was lower than the baseline model. This is unusual in the sense that many other publications note that suction usually produces a higher ratio than injection.

Speaking of suction, the study by Azim et. al. [28] focuses on the delay of boundary layer separation by suction using CFD analysis at M = 0.6. Unlike previous studies, this study used suction pressure slots instead of velocity slots starting from 48%C to 70%C for various angles of attack. According to the results of the numerical analysis of NACA 4412, suction near the trailing edge causes the longest separation delay. Suction at 68%C of the airfoil changes the formation of the separation bubbles from 70%C to 96%C of the airfoil at a suction pressure of 65 kPa. Lift to drag ratio is 35% larger than that of suction at 80 kPa because suction at lower pressure causes a delay that occurs much farther downstream than at higher pressure.

The underlying mechanism of flow control, such as the suppression of the separation bubble and reduction of the upper surface pressure to increase the lift and decrease the drag, was studied by Genc et. al. [29]. Control of flow over NACA 2415 airfoil was studied at Re = 200,000 for $\alpha = 8$ degrees. The numerical simulations included single or multiple injection and suction jets at various locations on the upper surface with multiple jet ratios and angles. The study also compared how different turbulence models can accurately predict the location of the separation bubble. For single-blowing or suction scenarios, the $k-\omega$ SST model suppresses the separation bubble, but the $k - k_L - \omega$ transition model only pushes the bubble downstream in the suction case. Independent of the injection sites, smaller injection velocity ratios effectively suppress the separation bubble more than bigger injection ratios. For suppression, larger suction velocity ratios are preferable to smaller suction ratios. Perpendicular jet angles for suction instances and oblique jet angles for blowing provide better outcomes, respectively. Since the blowing jet negatively affects the top surface flow, it is generally found that the blowing jet flow control is worse than the suction case. Both transition methods for simultaneous injection and suction eliminate the separation bubble, increasing lift and decreasing drag. Yet, single suction jets continue to produce the best results because blowing jets seem to be inhibiting their effectiveness.

Much research [30, 31] has been conducted with simultaneous injection and suction. The term for these kinds of simulations is a co-flow jet in which there is an injection slot close to the leading edge and a suction slot close to the trailing edge, as shown in Fig 1.5. Chng et. al. [32] studied the flow on Clark-Y airfoil using both experimental and computational methods at various angles of attack. The experimental results showed that as the momentum coefficient, which depends on jet velocity, jet mass flow rate, freestream density and velocity, and projected wing area, increases, the lift increases significantly. However, for lower angles of attack, the lift is less sensitive to change. This is in agreement with the results from Julian et. al. [33] who showed that higher injection rates increase the lift coefficient significantly. Increasing the mass flow rate also increased the drag coefficient meaning the lift-to-drag ratios were higher for smaller flow rates.

Goodarzi et. al. [34] investigated the active flow control on NACA 0015 airfoil for angles of attack of 12 to 17 degrees at Re = 455,000. The study was carried out using Ansys Fluent over a range of parameters: jet amplitude (1.0, 2.0, and 6.0), jet locations (10%C, 30%C, and 50%C), and jet angles (0, 30, and 45 degrees). The results showed the optimal jet was tangential, and simulated results and experimental findings agreed well. Evaluating various blowing applications revealed that the lift coefficient improves more efficiently when the jet is located close to the trailing edge, whereas the drag coefficient exhibits the opposite pattern. Simulations revealed that while raising jet velocity ratios has an amplifying effect on the lift-generating process, it does not always have a consistent impact on the drag coefficient. It was discovered that blowing significantly affects how long the suction side of the airfoil takes to separate.

The research by Kitsios et. al. [35] presents a numerical analysis that investigates the effect of angle of attack and the application of aerodynamic control using zero-net-mass-flux (ZNMF) jets on the boundary layer characteristics of an airfoil. A ZNMF jet that spans

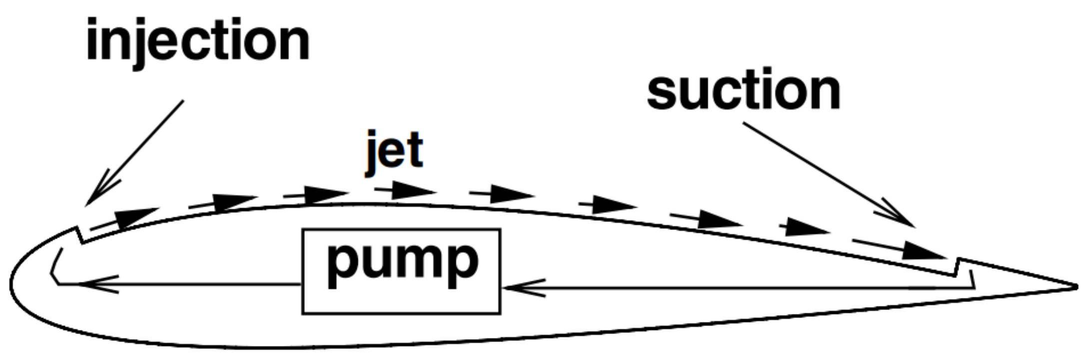

Figure 1.5: Schematic of Co-Flow Jet [6]

the entire leading edge of a NACA 0015 airfoil with the flow arrangement is normal to the surface. The validity of the 2-D simulation and 3-D LES given was determined using the studies of Tuck and Soria [36]. Prior to separation, the 2-D and 3-D models' velocity profiles and instantaneous streamwise vorticity plots at $\alpha = 18$ were comparable, allowing the use of the 2-D data to show how the boundary layer characteristics change. The separation point moved toward the leading edge as α was increased, and momentum thickness grew. The separation point was slightly pushed downstream by the ZNMF jet, which also reduced momentum thickness.

Akcayoz [37] optimized the synthetic jet location, angle, and frequency on NACA 0015 airfoil at Re = 896,000. The optimization was based on increased L/D ratio and was conducted for angles of attack of 10, 14, and 18 degrees. The instantaneous and phase-averaged flowfields, changes in aerodynamic load over time, and the position of the separation point were all examined in order to explore the computational findings. Based on the optimization, the synthetic jet performed best at post-stall angles of attack, greatly improving the L/D ratio and postponing the separation of separated flows. The greatest value in the design space at all angles of attack was consistently observed to be the optimal synthetic jet velocity. The position of the separation point and the optimal synthetic jet location was shown to move across the leading edge as the angle of attack increased, and the optimal synthetic jet angle was seen to increase as the angle of attack grew. The optimal synthetic jet frequency was seen to be the least dominant variable for all angles of attack because a lower jet frequency translates into a bigger jet slot size with a constant jet power coefficient (a non-dimensional parameter that is a function of freestream density, jet frequency, jet velocity, and jet length).

Based on Akcayoz's study, Montazer et. al. [38] optimized synthetic jet actuator parameters, such as jet frequency, jet length, jet velocity, and jet location, to control flow around the NACA 0015 airfoil at two angles of attack: 13 degrees (i.e. the stall angle) and 16 degrees (i.e. the post-stall angle). The objective of the study was to maximize the aerodynamic performance of the airfoil by solving the unsteady Reynolds-Averaged Navier-Stokes equations at Re = 896,000. The response surface methodology and flow solver were combined to maximize the jet performance and to enhance the airfoil's aerodynamic properties. The stall was delayed, and the aerodynamic performance (lift-to-drag ratio) was enhanced by 29%. Lift-to-drag ratio experienced a 66% improvement in the post-stall region as a result of the reattachment of the recirculation zone on the airfoil's suction side. It was found that as the angle of attack increased, the ideal length of the synthetic jet became shorter. As the synthetic jet actuator was utilized, the separation point went closer to the tailing edge on the upper surface. Between angles of attack of 13 and 16 degrees, it was discovered that the ideal actuation jet frequency and jet outlet velocity were decreasing. The synthetic jet was shown to be the most efficient at post-stall angles of attack, considerably improving the lift-to-drag ratio and delaying flow separation.

Furthermore, Parthasarathy et. al. [39] also performed flow control enhancement over NACA 0015 airfoil at Re = 896,000 for an angle of attack of 20 degrees. The jet location and the jet width were fixed while the jet frequency, velocity, and angle were varied. The results showed that the operating frequency becomes more irrelevant for lift enhancement at greater amplitudes and smaller angles. For optimal properties, the frequency must be kept to a minimum for lower angles and smaller amplitudes. At lower angles of injection, the lift values appear to be only minimally sensitive to the frequency of operation. But it's fascinating to see that when the angle widens, the graph's concavity shifts from practically zero to concave upward.

Chapter 2: Numerical Method

2.1 Flow Solver

The numerical simulation of the flow control over the airfoil is performed by a commercial CFD solver, Ansys Fluent. The solver uses CFD to model fluid flow, heat and mass transfer, chemical reactions, and other related phenomena. The CFD process is streamlined from pre- to post-processing in a single graphic user interface (GUI). Fluent is renowned for its broad physics modeling features, which include fluid-structure interaction, combustion, single- and multiphase flows, and turbulence modeling. It is particularly well-known for its ability to scale effectively on high-performance computing (HPC) systems, enabling it to solve large models by making use of many processors. Additionally, Fluent offers a variety of solver options, such as pressure- and density-based solvers that cover low-speed to hypersonic flows as well as a pressure-based native GPU solver.

Since the jet is being modeled as synthetic, a pressure-based transient solver is used to examine the airflow. Fluent solves the conservation of mass and momentum equations for all flows, an energy equation for flows involving heat transfer and compressibility, and a species conservation equation for flow involving species mixing or reactions. If the flow is turbulent, additional transport equations are modeled. However, for this study, only the conversation of mass and momentum equations are considered along with an eddy viscosity model based on the Spalart-Allmaras turbulence model. The formulation for the conservation equations and the turbulence model can be seen in section 2.2 and 2.3, respectively.

In our simulations, the material properties were kept as solver defaults. The fluid was taken to be air with a density of 1.225 kg/m^3 and a viscosity of 1.7894E-05 kg/m-s. SIMPLEC (Semi-Implicit Method for Pressure Linked Equations-Consistent) method was used for pressure-velocity coupling. In this method, the pressure-correction under-relaxation factor can be applied to improve convergence, but for this study, it was kept at a default value of 1.0. Next, the Least Squares Cell-Based gradient was applied. The gradients are necessary for computing secondary diffusion terms and velocity derivatives. The least-squares method is first-order accurate and is also consistent, meaning that, regardless of the type of elements, the gradient of a linear function is computed to round-off error. Additionally, the computational costs are comparable to the Green-Gauss approach.

Lastly, the solution was obtained using a second-order method. In Fluent, the face values are required for convection terms and must be interpolated from the cell center values which are calculated using an upwind scheme. The upwind refers to the face value that is computed based on the values of the upstream cells in the direction of the fluid flow. For momentum and turbulent viscosity, the second-order upwind scheme was selected. Using this approach, the second-order accuracy in the cell faces is achieved through the Taylor series expansion of the cell-centered solution. For time discretization, the second-order implicit method was selected.

2.2 Governing Equations

As stated above, Fluent solves conservation equations for mass and momentum. Here, the incompressible conservation equations [40] are presented in an inertial reference frame.

The incompressible continuity equation can be written in differential form as:

$$\nabla \cdot \vec{u} = 0 \tag{2.1}$$

where $\vec{u}$ is the fluid velocity vector. For incompressible flows, density is constant, so all derivatives of the density are zero.

The incompressible conservation of momentum equation can be written in differential form as :

$$\rho \left[\frac{\vec{u}}{\partial t} + \nabla \cdot (\vec{u}\vec{u}) \right] = -\nabla p + \nabla \cdot \left(\vec{\vec{\tau}} \right) + \rho \vec{g} \tag{2.2}$$

where the term on the left-hand side is density times rate of change of velocity. On the right-hand side, the first term is the net pressure force, the second term is the total shear force, and the third term is for gravitational forces.

The stress tensor is given by

$$\vec{\vec{\tau}} = \mu\left[\left(\nabla\vec{u} + \nabla\vec{u}^T\right) - \frac{2}{3}\nabla\cdot\vec{u}I\right] \tag{2.3}$$

where the second term on the right-hand side is volume dilation and I is unit tensor.

2.3 Turbulence Model

Ansys Fluent offers a variety of turbulence models users can choose from. For this study, the one-equation Spalart-Allmaras model was employed. The Spalart-Allmaras model, which utilizes a transport equation and solves for eddy viscosity variable $\tilde{\nu}$, was formulated using a Galilean invariant, dimensional analysis, and selected empirical results, which used wakes, flat-plate boundary layers, and 2D mixing layers [41]. Compared to two-equation models, the Spalart-Allmaras model shows good convergence in simpler aerodynamic flows. The Spalart-Allmaras model is relatively computationally efficient compared to some of the other turbulence models. However, this model is best suited for external aerodynamics and may be inaccurate for certain types of flows or under certain conditions.

The Spalart-Allmaras turbulence model [42] can be written in differential form as:

$$\begin{aligned}\frac{\partial\tilde{\nu}}{\partial t} + \frac{\partial}{\partial x_j}(\tilde{\nu}u_j) =& C_{b1}\tilde{S}\tilde{\nu} \\ &+ \frac{1}{\sigma}\left\{\frac{\partial}{\partial x_j}\left[(\mu_L + \tilde{\nu})\frac{\partial\tilde{\nu}}{\partial x_j}\right] + C_{b2}\frac{\partial\tilde{\nu}}{\partial x_j}\frac{\partial\tilde{\nu}}{\partial x_j}\right\} \\ &- C_{w1}f_w\left(\frac{\tilde{\nu}}{d}\right)^2\end{aligned} \tag{2.4}$$

where the turbulent eddy viscosity is computed from:

$$\mu_T = f_{v1}\tilde{\nu} \tag{2.5}$$

On the right-hand side of Eq. 2.4, the first term represents the turbulent eddy viscosity production, the second term represents the diffusion, and the third term represents the near-wall turbulence destruction. The subscript b stands for "basic," w stands for "wall," and v stands for "viscous."

The following formulas are used in the evolution of the production term:

$$\begin{aligned}
&\tilde{S} = f_{v3}S + \frac{\tilde{\nu}}{\kappa^2 d^2} f_{v2}, \\
&f_{v1} = \frac{\chi^3}{\chi^3 + C_{v1}^3}, \qquad f_{v2} = 1 - \frac{\chi}{1 + \chi f_{v1}}, \\
&\chi = \frac{\tilde{\nu}}{\mu_L}
\end{aligned} \tag{2.6}$$

where S is the magnitude of the vorticity:

$$S = \sqrt{2\Omega_{ij}\Omega_{ij}} \tag{2.7}$$

and Ω_{ij} is the mean rotation rate tensor which is defined by

$$\Omega_{ij} = \frac{1}{2}\left(\frac{\partial u_i}{\partial x_j} - \frac{\partial u_j}{\partial x_j}\right) \tag{2.8}$$

The destruction of the eddy viscosity term is evaluated using the following equations:

$$\begin{aligned}
&f_w = g\left(\frac{1 + C_{w3}^6}{g^6 + C_{w3}^6}\right)^{1/6}, \\
&g = r + C_{w2}(r^6 - r), \qquad r = \frac{\tilde{\nu}}{\tilde{S}\kappa^2 d^2}
\end{aligned} \tag{2.9}$$

Finally, the constants in Eqs. 2.4-2.9 have the following values:

$$
\begin{aligned}
&C_{b1} = 0.1335, \qquad C_{b2} = 0.622, \\
&C_{v1} = 7.1, \qquad \sigma = 2/3, \qquad \kappa = 0.4187, \\
&C_{w1} = \frac{C_{b1}}{\kappa^2} + \frac{1 + C_{b2}}{\sigma}, \qquad C_{w2} = 0.3, \qquad C_{w3} = 2.0
\end{aligned}
\tag{2.10}
$$

2.4 Grid Generation

In this study, a structured, C-type grid was utilized to analyze the flow around the airfoil. The grid was generated using the commercial software, Pointwise. In contrast to a single extrusion, this C-grid was generated using three H-grids. The process for creating the grid was as follows. First, the NACA 0015 profile was created using the NACA airfoil generator. [43] Then, a fixed number of points were selected for the upper and lower side of the airfoil. The same number of points were also selected for the downstream, upper, and lower boundaries. The points on the upstream boundary corresponded to the points on the airfoil. The wall spacing was kept uniform with a value of 1.0E-5 to ensure a y+ value of less than 1.0.

For this study, three different meshes were examined with the following dimensions: 401x101, 801x201, and 1201x301. For all of these meshes, the grid extended from -10 chords upstream to 15 chords downstream, and the upper and lower boundary extended 10 chords from the airfoil. Upon completing the grid convergence study, see 4.1, the middle mesh, 801x201, was chosen which comprised 360,599 nodes.

There were two different sections of the airfoil which contained clustered regions: at 10%C and at 43%C. This was to ensure proper data was collected in the synthetic jet region. Even with the clustered region, the dimensions were kept to 801x201 for the experiment grid. The domain can be seen in Figures 2.1 and 2.2.

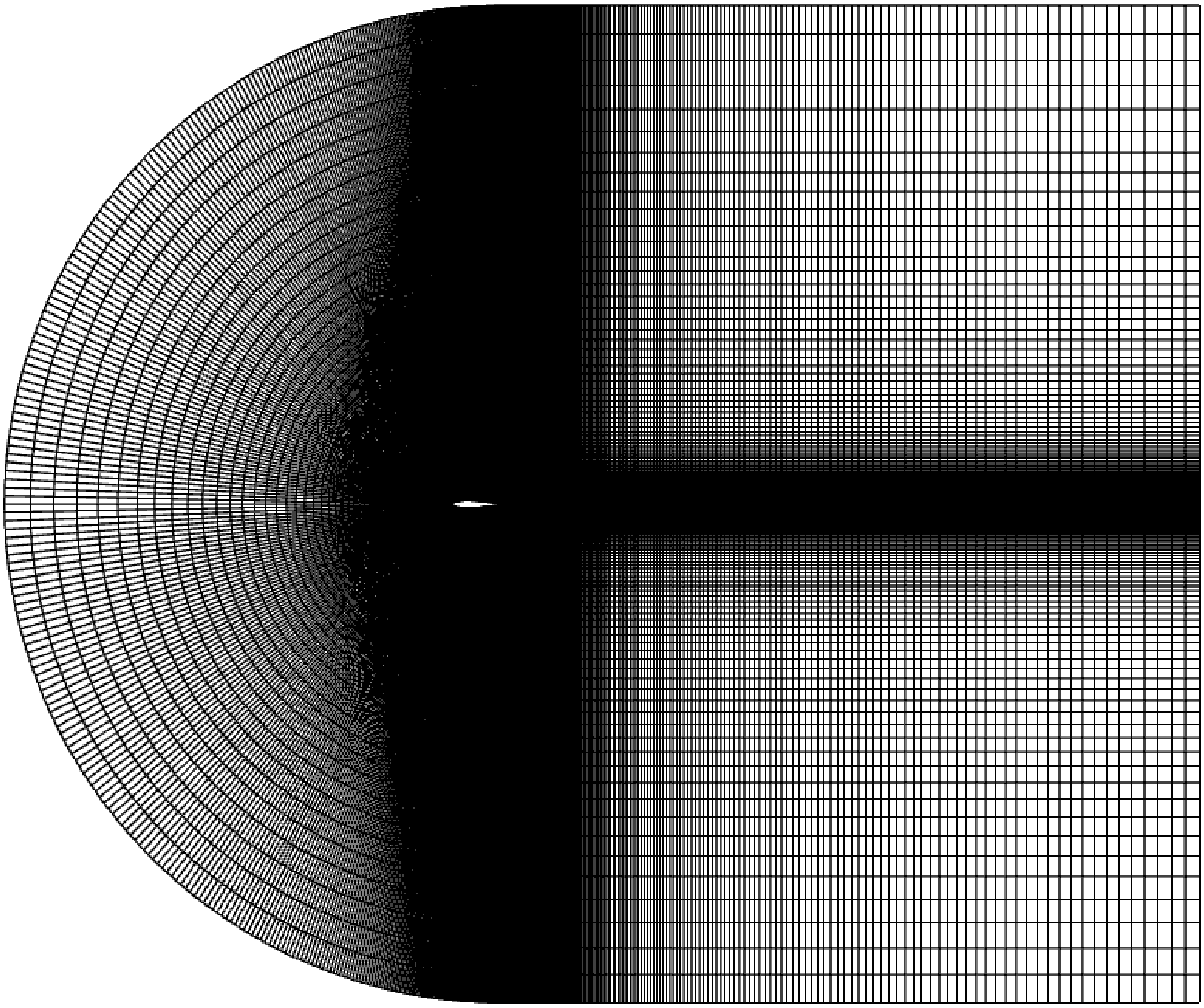

Figure 2.1: Computational Domain

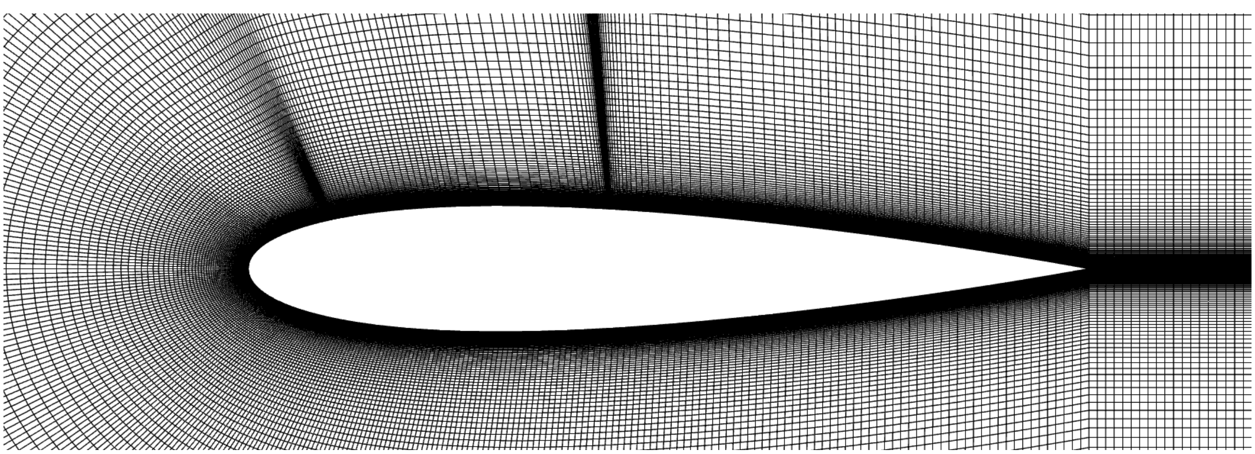

Figure 2.2: Mesh Around the Airfoil

2.5 Boundary Conditions

In Fluent, users can select up to 10 different types of boundary conditions. In this study, only three types of boundary conditions were used: velocity inlet, pressure outlet, and viscous wall, as shown in Figure 2.3.

Velocity inlet boundary condition was used to define the flow velocity at the far-field. Here, the flow direction was implemented in terms of components, so that the airfoil angle of attack can be accounted for. The inlet velocity components can be seen below.

$$\begin{aligned} X - Component : u = U_\infty * cos(\alpha) \\ Y - Component : v = U_\infty * sin(\alpha) \end{aligned} \tag{2.11}$$

where U_∞, 13.0889 m/s, is calculated based on the Reynolds number of 896,000 using the following definition

$$Re = \frac{\rho U_\infty C}{\mu}. \tag{2.12}$$

All other properties displayed in the velocity inlet dialog box were kept as defaults besides the turbulent viscosity ratio. The turbulent viscosity ratio, μ_t/μ, is defined as the ratio of the turbulent viscosity and laminar viscosity. The turbulent viscosity is calculated by the turbulence model and the lane viscosity is calculated from the material panel. In this study, the turbulent viscosity ratio was set to 1.0.

Pressure outlet boundary condition was used at the exit. When backflow occurs during iteration, using a pressure outlet boundary condition rather than an outflow condition often leads to a faster rate of convergence. Similar to the velocity inlet conditions, all the properties were kept at their default values.

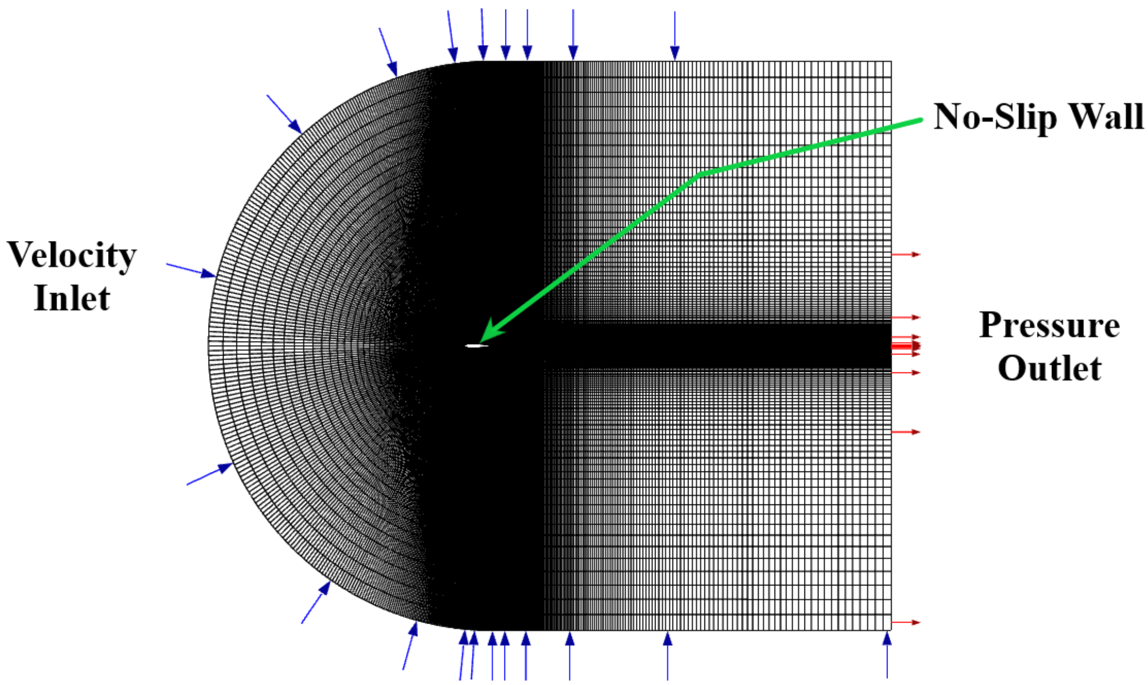

Figure 2.3: Boundary Conditions

Lastly, the wall boundary condition was used for the airfoil. Since the flow is viscous, the no-slip boundary condition was enforced at the wall by default. When the jet was enabled, a velocity inlet boundary condition was used. The details of the synthetic jet can be seen in the following section.

2.6 Modeling of Synthetic Jet

Unlike the airfoil boundary, which acts as a no-slip wall, the synthetic jet boundary introduces flow into the field. Figure 2.4 depicts the synthetic jet implementation on the airfoil. In Fluent, the jet boundary is modeled as a "velocity inlet" and the "Components" method is selected for velocity vectors. This method gives the user an option to input the x- and y-components. The definition of the jet velocity components are given in Eqn. 2.13.

$$\begin{aligned} X - Component: u = 0.5 * U_\infty * A * cos(\theta + \beta) * sin(2\pi F t) \\ Y - Component: v = 0.5 * U_\infty * A * sin(\theta + \beta) * sin(2\pi F t) \end{aligned} \tag{2.13}$$

In the equations above, A is the ratio of jet velocity to the freestream velocity, θ is the angle between the local jet surface and the jet entrance velocity, β is the angle between the freestream velocity direction and the local jet surface, F is the jet frequency, and t is the physical time. The sine function controls the oscillatory motion of the synthetic jet based on frequency and physical time.

In Figure 2.5, the jet profile is depicted as a sinusoidal function. However, in this study, the parabolic profile was not implemented. Rather, a rectangular profile, or a "top hat" distribution (as shown in Figure 2.6), was implemented. To ensure the same amount of flow is injected, the area of the sinusoidal function was calculated which came out to a value of 0.5. As a result, the jet velocity is reduced by a factor of 0.5.

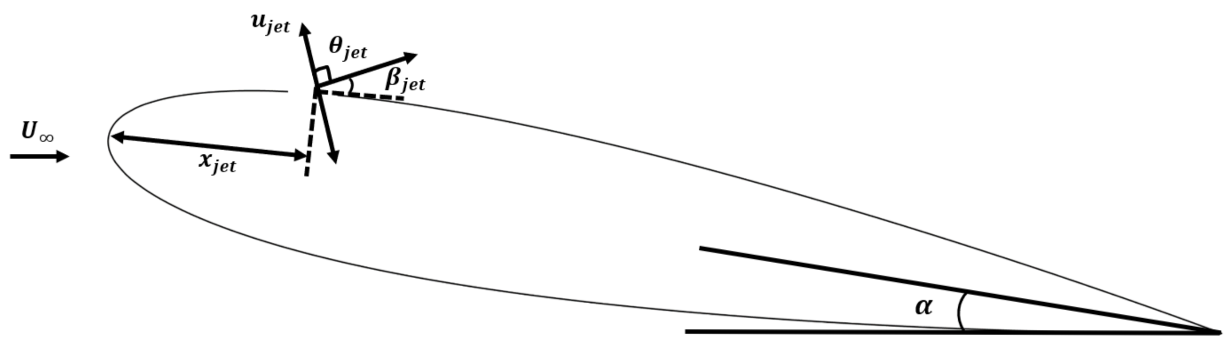

Figure 2.4: Synthetic Jet Representation

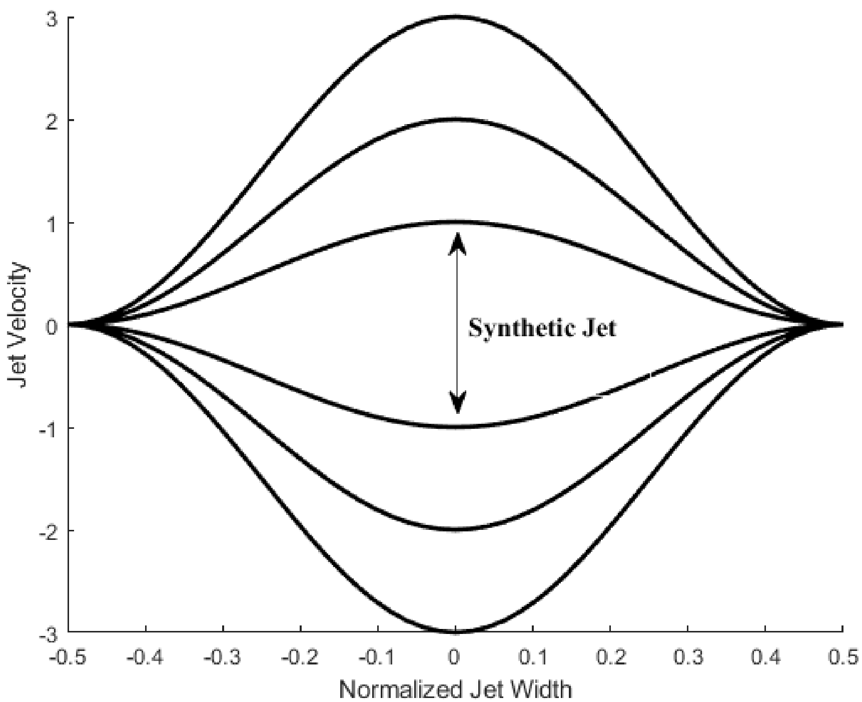

Figure 2.5: Sinusoidal Synthetic Jet

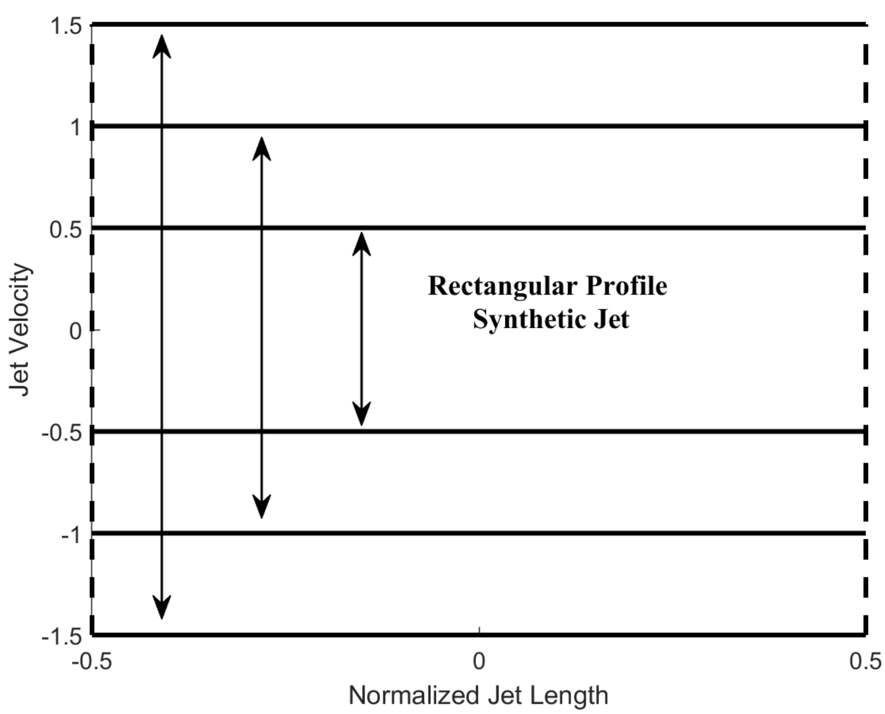

Figure 2.6: Rectangular Jet

Many studies have been conducted regarding the length of the jet. Dannenberg and Weiberg [44] examined different jet lengths and found that the lift will not change significantly for suction cases if the length is beyond 2.5% chord length. So, for this study, the length of the jet was selected to be 0.2608% of the chord length. This value is calculated from Akcayoz [37] who performed an optimization study using a constant jet power coefficient which is a function of freestream density, jet velocity, jet length, and jet frequency. It is important to note that in this study, different jet amplitudes and jet frequencies were examined, however, the jet length remained constant.

Chapter 3: Thesis Significance

As aircraft evolve, the advantages of flow control have grown in significance. A relatively new application in the commercial aircraft industry proposes a system in which the circulation pattern of a wing is actively regulated by a grid of small oscillating jets with blowing and suction at varying magnitudes and frequencies to reduce the upper surface normal shock wave, hence lowering drag [29]. The demand for a technique of control with permanent surfaces has increased with the development of stealth. Additionally, in order to save on fuel, economic interests have called for further weight reduction. The desire for higher lift-to-drag ratios is a result of this demand [34]. Hence, the main objective of this thesis is to investigate which set of parameters for the synthetic jet produces optimal results.

As mentioned before, the Fluent solver was compared with the optimized study conducted by Akcayoz. In that study, the jet velocity was fixed, and the jet frequency, jet angle, and jet location were "optimized". For this study, the optimized jet angle and jet location from Akcayoz have been fixed, and different jet velocities and different jet frequencies have been analyzed. The objective of this study is to determine which set of jet velocities and jet frequency produces the maximum lift-to-drag ratio.

Two cases are examined with different angles of attack for a Re = 896,000. For case 1, the angle of attack is 10 degrees, and for case 2, the angle of attack is 14 degrees. For both, the examined jet amplitudes were 2.0, 2.5, 3.0, 3.5, and 4.0, and the jet frequencies were 0.4, 0.8, and 1.2 Hz. Based on the frequency, the time step size was calculated using the following equations:

$$T = \frac{1}{F} \tag{3.1}$$

$$dt = \frac{T}{100} \tag{3.2}$$

to ensure that 100-time steps were taken at each period. The time step sizes were determined to be 0.1571 s, 0.0785, and 0.0524 s for 0.4, 0.8, and 1.2 Hz, respectively. For case 1, the jet location and angle were fixed at 10%C and 28.5 degrees, respectively. The jet location for case 2 was 43%C with a jet angle of 42.5 degrees.

The hypothesis here is that as the jet velocity increases, the lift-to-drag ratio will increase. During many validation cases, it was observed that increasing the amplitude positively impacts the lift-to-drag, and that same reasoning is used for this hypothesis. Looking at Akcayoz's optimization steps, it was seen that with higher frequency, the lift-to-drag ratios increased. Thus, the same hypothesis can be made regarding the frequency; as the frequency increases, the lift-to-drag ratio will increase. Nonetheless, it is important to note that Akcayoz experimented with almost four times the optimal frequency, and did not see the ratio increase significantly. For this study, the frequency was slightly changed, so it may not have as much impact as velocity might have.

Chapter 4: Results and Discussions

4.1 Grid Convergence

In this section, a grid convergence study is performed. First, the pressure distribution with lift and drag coefficients obtained from various grid sizes are shown. Then, the comparison of different turbulence models is performed. For both of these cases, the flow is computed at $\alpha = 14$ degrees without the synthetic jet. Additionally, since the synthetic jet boundary is not used, all of these cases are run as steady instead of transient.

As mentioned before, three different types of meshes were generated: 401x101, 801x201, and 1201x301. Table 4.1 shows the lift and drag coefficients for different grid resolutions. As one can see, the lift slightly increased as the grid resolution was increased, and for drag, there was a minimal change with respect to the resolution. The pressure coefficient is plotted in Figure 4.1. All of the simulations agreed well with one another. As a result, the medium mesh was chosen for this study.

Next, two different turbulence models were compared, Spallart-Allmaras and $k - \omega$ SST (shear stress transport). This SST model of Menter [45, 46] is a combination of the k-ω model of Wilcox [47] and a high Reynolds number k- ϵ model. This model provides an accurate prediction of flows with strong adverse pressure gradients and of pressure-induced boundary layer separation. The $k - \omega$ SST model solves two transport equations, one for the turbulent kinetic energy (k) and the one for the specific dissipation rate (ω). Considering that the $k - \omega$ SST model needs to solve two equations, it can be computationally costly compared to Spalart-Allmaras, a one-equation model. Furthermore, the SST model produces a slightly lower lift-to-drag ratio compared to Spalart-Allmaras. This can be seen from the pressure coefficient plot, Figure 4.2, and the force coefficient data, Table 4.2. Due to this computational advantage, the Spalart-Allmaras turbulence model was used for this study.

Table 4.1: Grid Properties with Lift and Drag Coefficients

Grid Size	# of points around the airfoil	Total Nodes	C_L	C_D
401x101	401	40,199	1.3257	0.0305
801x201	801	160,399	1.3349	0.0295
1201x301	1201	360,599	1.3385	0.0295

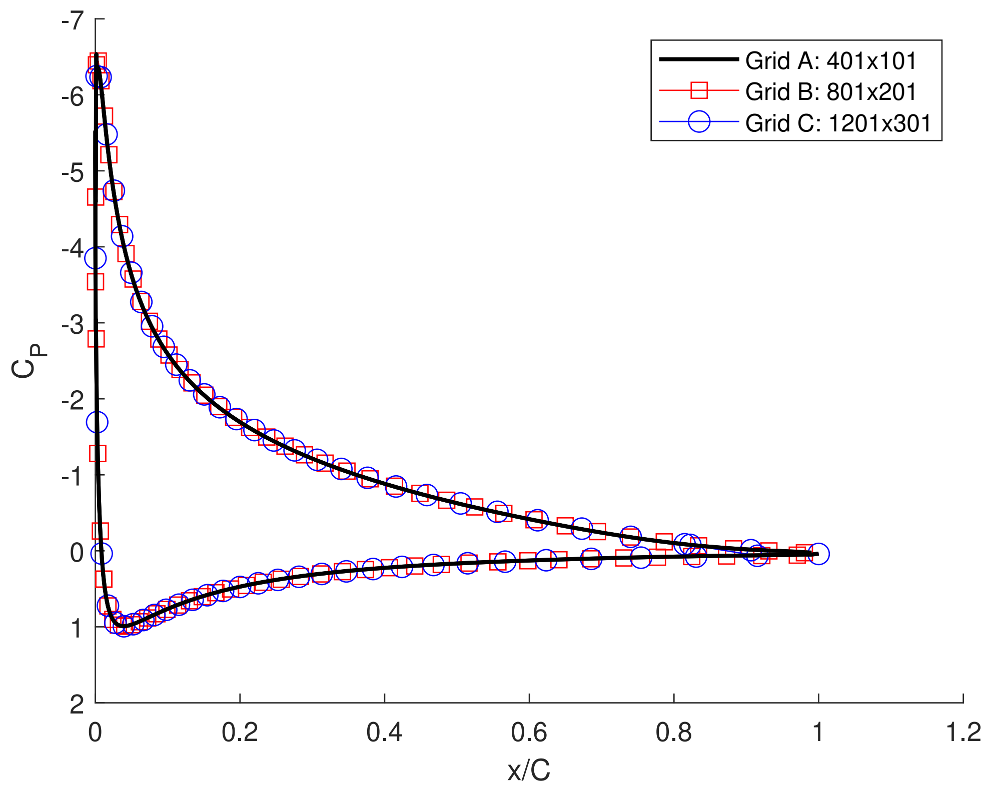

Figure 4.1: Grid Independence Study of the Grids

Table 4.2: Lift and Drag Coefficients for Different Turbulence Models

Turbulence Model	C_L	C_D	L/D
Spalart-Allmaras	1.3349	0.0295	45.22
$k-\omega$ SST	1.2503	0.0311	40.16

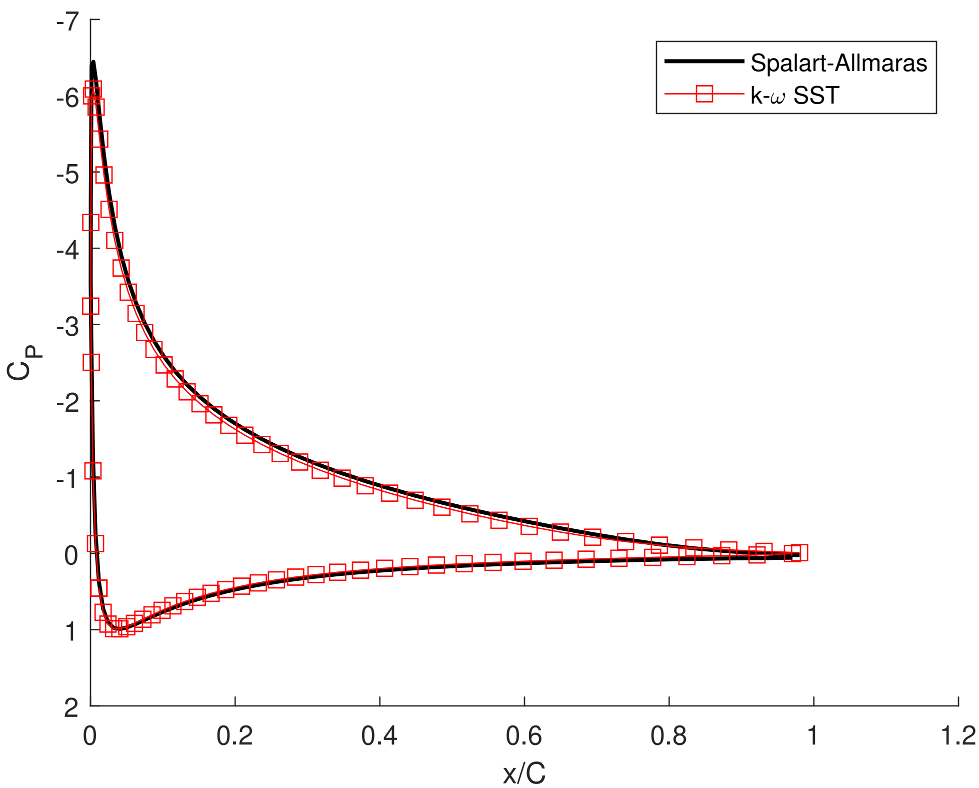

Figure 4.2: Surface Pressure Distribution of Two Turbulence Models

Lastly, the effects of different inlet velocities are compared. Since the inlet velocities were varied, this would also change the Reynolds number. As a result, the viscosity was also varied by the same factor to ensure the Reynolds number does not change. There were two different velocities that were examined besides the base velocity used for this study, 13.0889 m/s. One was half the base velocity, 6.5440 m/s, and the other was double the base velocity, 26.1778 m/s. Table 4.3 shows the force coefficients for different inlet velocities and Figure 4.3 shows the pressure coefficient plot at the three examined velocities. Looking at the pressure coefficient plot, the data for all the inlet velocities were well in agreement with each other. This can be further seen by the little to no discrepancies between the lift and drag coefficients. The lift force changed a little for the base velocity, but different inlet velocities had no impact on the aerodynamic drag. Hence, it can be seen the inlet velocity does not influence the aerodynamic forces as long as the Reynolds number is the same.

4.2 Verification

In this section, the grid and flow solver verifications are performed by comparing the current data to previously published literature. First, Fluent's steady-state results without any jet at $\alpha = 14$ degrees are compared to the results from the in-house External Flow Solver and XFOIL. Then, Fluent's results are compared to the experimental data from Sheldahl et. al. [48]. Next, a sweep study is performed from 12 to 17 degrees with and without steady injection, and the results are compared to Goodarzi et. al. [34]. Lastly, the results using synthetic jet are compared to the results from Akcayoz [37].

Verification and validation are very essential in CFD simulations. The verification evaluation assesses if the conceptual model's computational and programming implementation is accurate and checks for mistakes in computer code. The computer simulation's validity is evaluated to see if it agrees with physical reality. It investigates the science in the models by contrasting them with the findings of experiments. Here the validity of the Fluent was checked with the data from other solvers: External Flow solver and XFOIL. External Flow

Table 4.3: Lift and Drag Coefficients for Different Inlet Velocities

Inlet Velocity (m/s)	C_L	C_D	L/D
6.5440	1.3347	0.0295	45.18
13.0889	1.3349	0.0295	45.22
26.1778	1.3347	0.0295	45.18

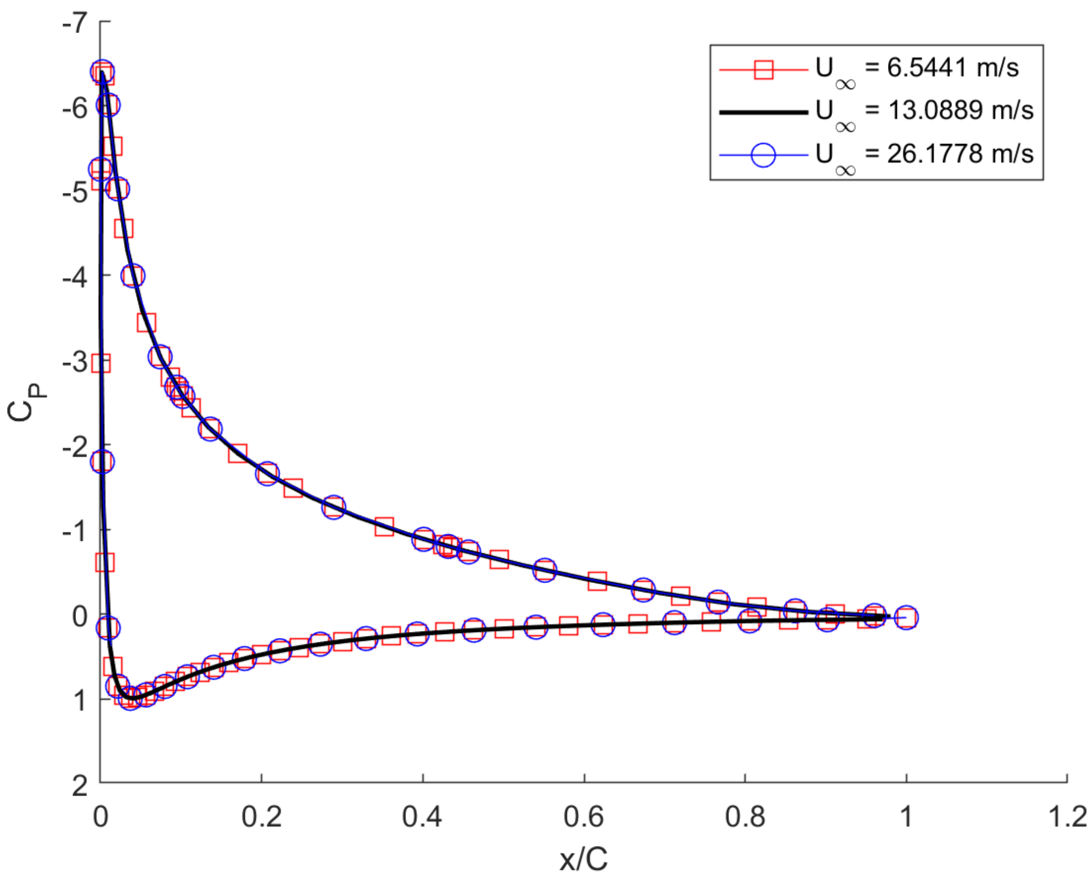

Figure 4.3: Surface Pressure Distribution for Different Inlet Velocities

Solver, originally modeled for 2D flow through a turbine cascade, uses the Navier-Stokes equation to solve both steady and unsteady compressible flows. Since it is a compressible solver, inlet velocity cannot be specified; instead, a Mach number of 0.1 was used to calculate the pressure and force coefficients using a 513x513 O-grid. On the other hand, XFOIL [49] is a computer program used for designing and analyzing subsonic airfoils for both inviscid and viscous cases. It utilizes the e^N method to calculate the lift and drag coefficients for given Reynolds and Mach numbers. The Mach number is again set to 0.1, and Re = 896,000.

For solver validation, the pressure coefficient plots were compared using all three solvers along with the lift and drag coefficients. Looking at Figure 4.4, the pressure coefficients are well in agreement with one another. Furthermore, the agreement can be seen by the lift coefficient in Table 4.4 where they are very close to each other. The drag coefficient shows more difference. There may be several reasons for this difference. First, the grid dimensions are different. Second, the difference could be due to viscous effects as each solver uses a slightly different viscous model. Third, the inlet conditions varied from solvers where for Fluent, freestream velocity was prescribed and for External Flow Solver and XFOIL, the Mach numbers were input. Other than these differences, the Fluent solver produced similar results compared to other solvers.

Additionally, the results of the Fluent solver were compared to the experimental results of Sheldahl et. al. Here, the flow is compared for a Reynolds number of 680,000, and as a result, the inlet velocity was 9.9330 m/s. Figures 4.5 and 4.6 show lift and drag coefficients over various angles of attack for the NACA 0015 airfoil. For the lift coefficient, the trend was similar, however, the stall angle (the angle at which the lift starts decreasing) for the experimental study was 14 degrees, and for the present study, it was after 16 degrees. The drag coefficient, on the other hand, contained a higher discrepancy, but the trend was similar: as the angle of attack increased, the drag increased as well. The disagreement in the results could be due to the reasons provided before. The turbulence model was different in each study. For the numerical analysis, Spalart-Allmaras was used while for the experimental

Table 4.4: Lift and Drag Coefficients for Different Flow Solvers

Turbulence Model	C_L	C_D	L/D
Ansys Fluent	1.3349	0.0295	45.22
External Flow Solver	1.3208	0.0271	48.74
XFOIL	1.3373	0.0247	54.14

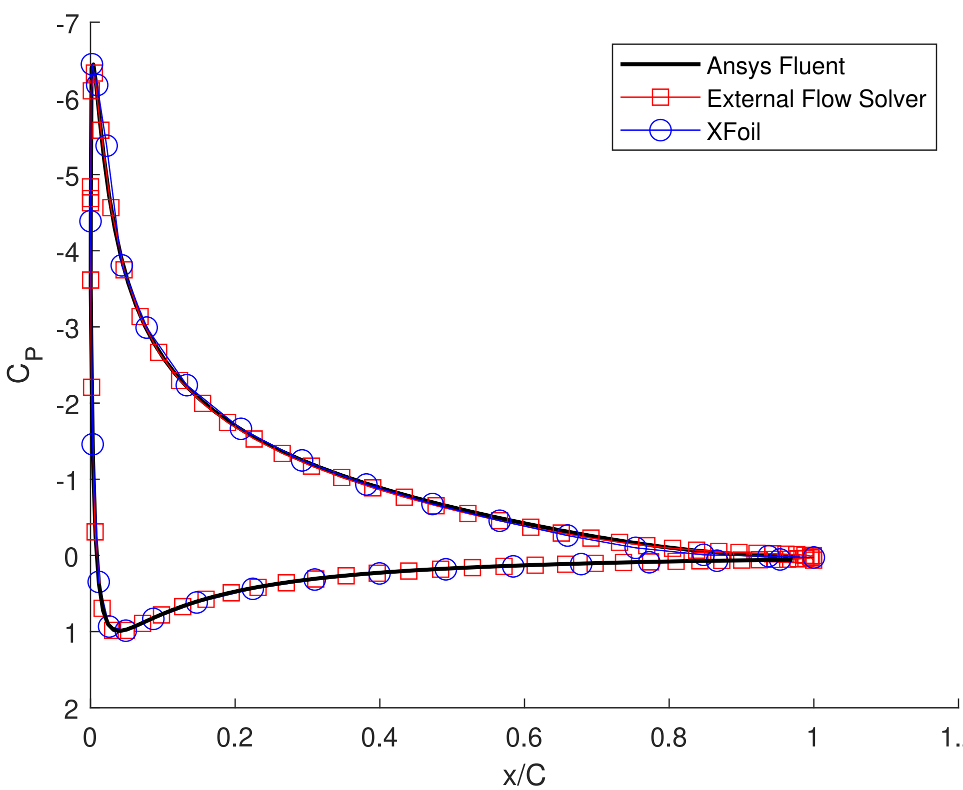

Figure 4.4: Comparison of Fluent, External Flow Solver, and XFOIL

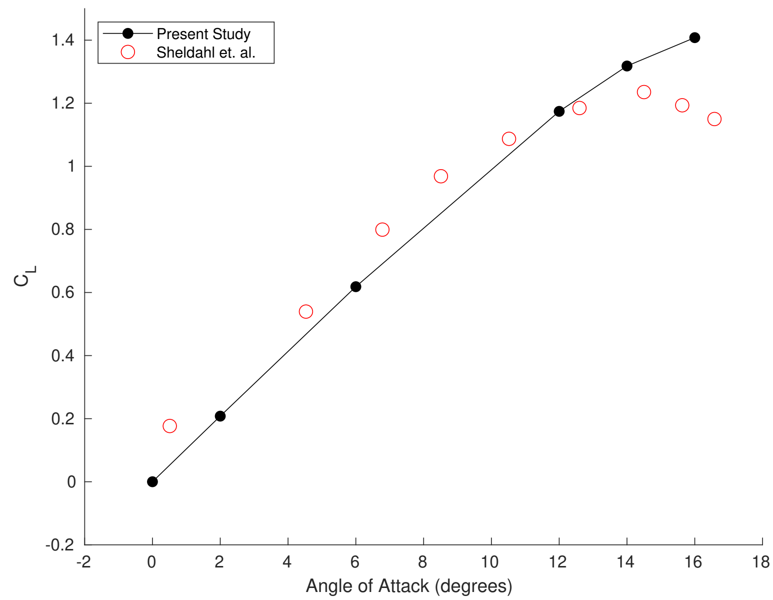

Figure 4.5: Lift Coefficient Comparison for Re = 680,000

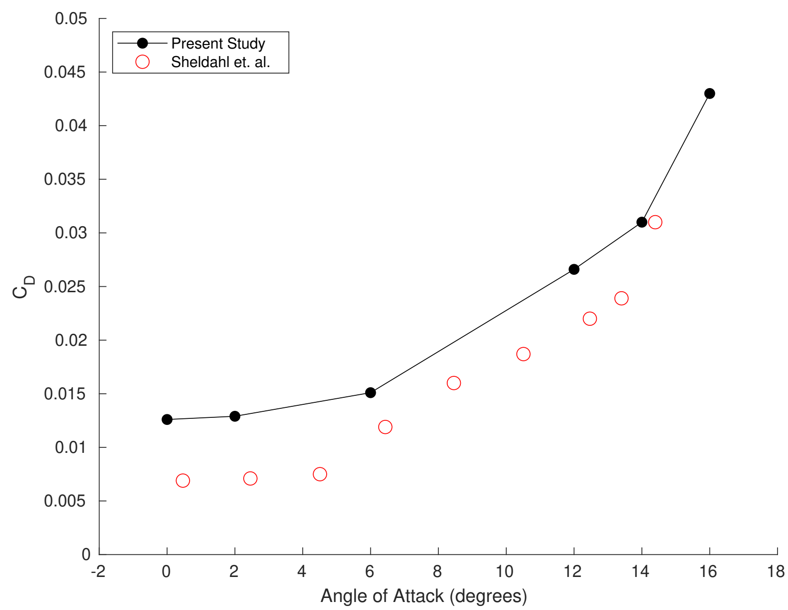

Figure 4.6: Drag Coefficient Comparison for Re = 680,000

study, the data was corrected with a wind-turbulence factor. Overall, the trends were in good accordance with each other.

Next, current data were compared to those previously published in the literature. The validation was performed for a NACA 0015 airfoil without injection to ensure that the flow solver was producing accurate results. First, the current data was compared to Goodarzi et al., who investigated injection on NACA 0015 from an angle of attack of 12 degrees to 17 degrees at Re = 455,000 using Fluent. The sweep study from 12 to 17 degrees was also compared to the XFOIL data. For this case, the inlet velocity was set to 6.6467 m/s, and both the first-order and second-order upwind methods were used along with the SIMPLE-Consistent method in Fluent.

Figure 4.7 shows the lift and drag coefficients from 12 to 17 degrees from the literature, XFOIL, and Fluent calculations. The maximum lift coefficient defines the angle at which the airfoil will stall. By looking at Figure 4.7a, the stall for Goodarzi et al. and the experiment using the second-order method happens at 14 degrees. This is in contrast to the XFOIL and first-order data where the stall happens at 16 degrees. Looking at the drag coefficients, for all cases, the drag increases as the angle of attack increases. As the angle increases, the frontal area exposed to the free stream air increases along with the boundary layer thickness. Eventually, at higher angles of attack, the boundary layer will separate from the surface, leading to an increase in pressure drag, and thus, the drag coefficient. Overall, the numerical data were in acceptable agreement with the literature data and XFOIL data. The first-order method closely resembled Goodarzi et al. while the second-order method resembled XFOIL data.

Now that the baseline (with no injection) cases were in agreement with Goodarzi et al., cases with injection were compared using both first-order and second-order methods for an amplitude of 2.0 at 10%C, 30%C, and 50%C. The results can be seen in Figures 4.8-4.10. Similar to the cases without injection boundary, the first-order results were in better agreement with Goodarzi et al. than the second-order results. For the 10%C case, the

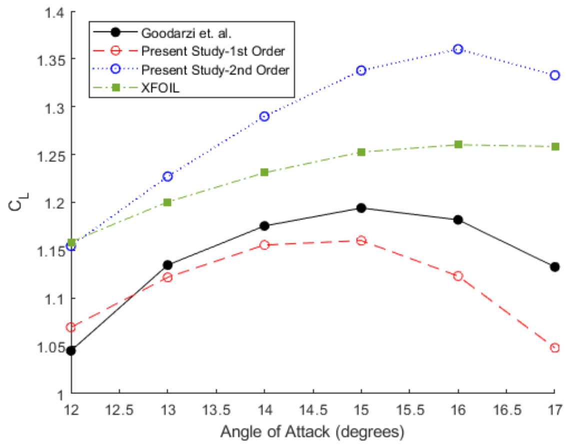

(a) Lift Coefficient

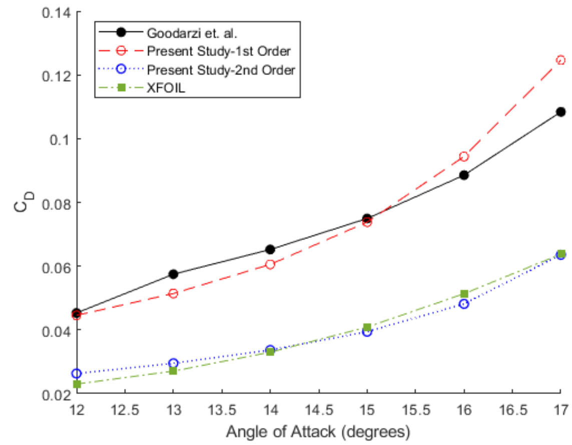

(b) Drag Coefficient

Figure 4.7: Lift and Drag Coefficient Comparison at Re = 455,000

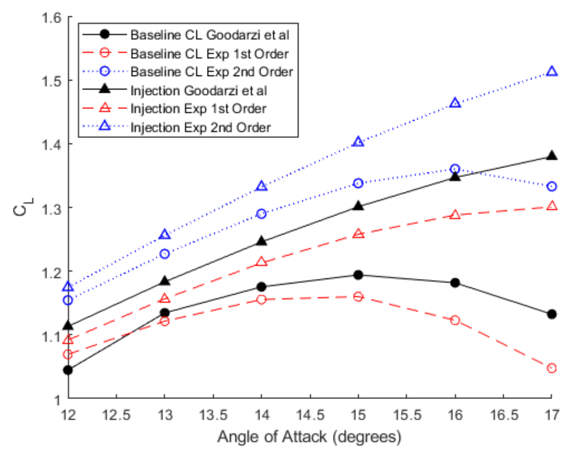

(a) Lift Coefficient

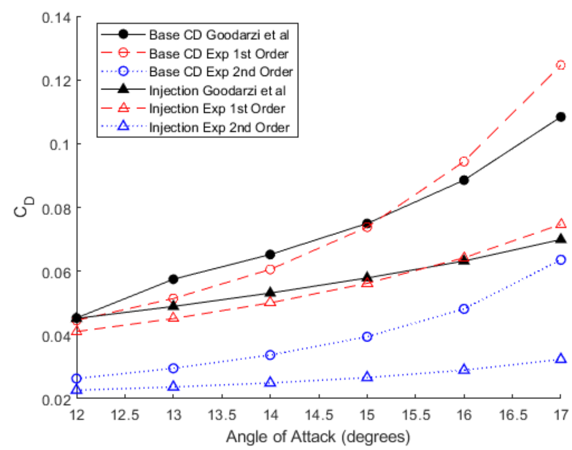

(b) Drag Coefficient

Figure 4.8: Lift and Drag Coefficient Comparison at Jet Location of 10%C

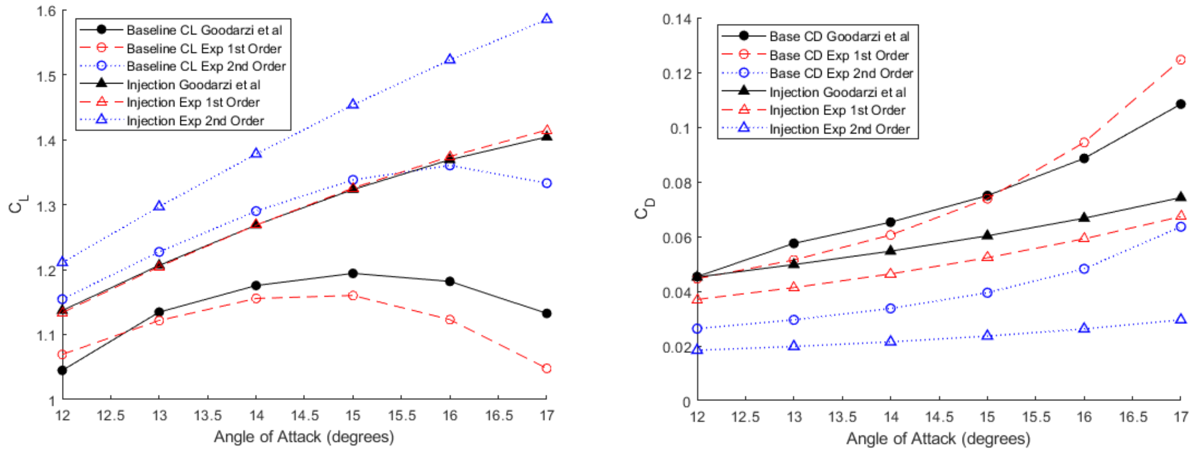

(a) Lift Coefficient **(b)** Drag Coefficient

Figure 4.9: Lift and Drag Coefficient Comparison at Jet Location of 30%C

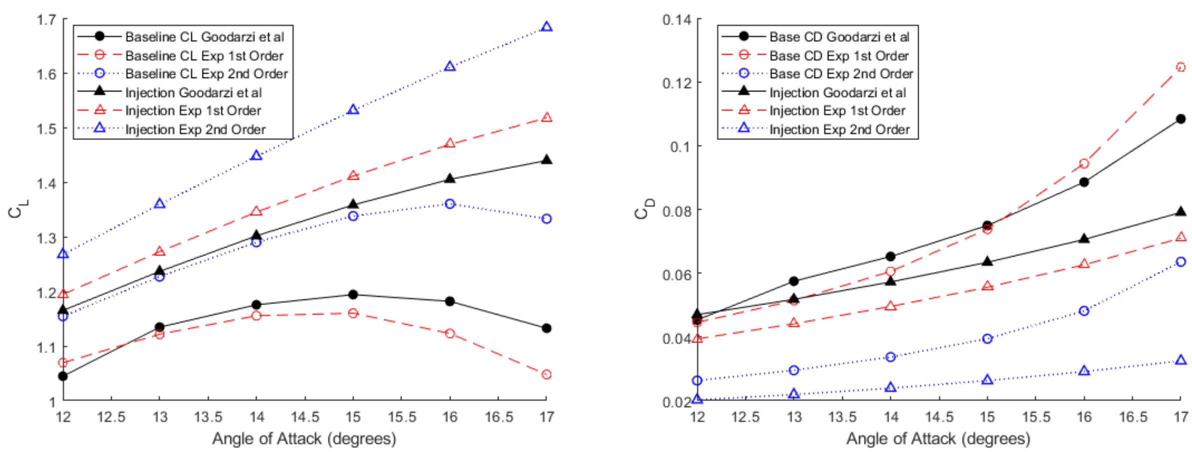

(a) Lift Coefficient **(b)** Drag Coefficient

Figure 4.10: Lift and Drag Coefficient Comparison at Jet Location of 50%C

injection trend for the lift coefficient was similar, however, the first-order method undershot the literature data and the second-order method overshot it. On the other hand, the drag coefficients for the first-order method were in better agreement with Goodarzi et al. data. For the 30%C case, the trends were the same for both methods, but this time, the lift coefficients for the first-order method were in strong conformity with Goodarzi et al. Again the drag coefficient matched well using the first-order method. This case produced the highest lift-to-drag ratios compared to the other two jet locations. The 50%C case had the largest discrepancy between the current data and literature data for both lift and drag coefficients.

Moreover, additional cases were also examined to confirm the validation of the Ansys Fluent solver. Contrary to the previous cases, this case examined the data from Akcayoz, who optimized the synthetic jet location, angle, and frequency on NACA 0015 airfoil at Re = 896,000. Akcayoz optimized for an angle of attack of 10°, 14°, and 18° using parabolic jet velocity profile, as shown in Figure 2.5, which fluctuated based on the input frequency. For this case, only the 14° angle case with a jet amplitude, frequency, angle, and location of 3.0, 0.8 Hz, 42.5°, and 43%C, respectively, was compared. In Fluent, time accurate solver was selected with dt of 0.0785 seconds to capture at least 100-time steps for each period. The inlet velocity was set to 13.08891 m/s, and the second-order upwind method was used for momentum and turbulent viscosity and the second-order implicit method of transient formulation. The solver was run until the periodic behavior was achieved for the lift and drag coefficients. The time average of those values was compared to the baseline coefficients and then to Akcayoz data as seen in Table 4.5. Compared to the baseline case, the present study showed positive results for the synthetic jet cases, i.e. the lift-to-drag ratio increased. Now comparing the present study results to Akcayoz, the lift-to-drag ratio of the present study did not increase as much as Akcayoz. There may be a couple of reasons for this discrepancy: (1) Akcayoz used an in-house developed Navier-Stokes solver and for the present study, the commercial software Fluent was used; and (2) as mentioned above,

Table 4.5: Baseline and Injection Comparison to Akcayoz

	Akcayoz			Present		
	C_L	C_D	L/D	C_L	C_D	L/D
No Jet	1.2700	0.0310	41.10	1.3347	0.0295	45.18
With Jet	1.3400	0.0280	48.50	1.3413	0.0293	45.74
Change (%)	5.80	-10.30	17.90	0.49	-0.74	1.23

Akcayoz used a parabolic jet profile, but for the present study, the parabolic was not used instead a rectangular profile was implemented.

4.3 Synthetic Jet Parameter Study

In the section, the results from the present study are shown. Two cases with different angles of attack, 10 and 14 degrees, were examined at Re = 896,000. For both cases, some parameters, such as jet location, jet angle, and jet width, were fixed while other parameters, like jet amplitude and jet frequency, were varied. For both cases, the examined jet amplitudes were 2.0, 2.5, 3.0, 3.5, and 4.0, and the jet frequencies were 0.4, 0.8, and 1.2 Hz. The fixed parameters can be seen in Table 4.6.

4.3.1 Case 1: $\alpha = 10°$

The results are first presented for an angle of attack of 10 degrees which is the pre-stall angle on the NACA 0015 airfoil. In Figure 4.11, one can see how the jet amplitude and jet frequency affected the aerodynamics coefficients. The effect of the jet amplitude can be clearly seen from the plot. As the amplitude increased, the coefficient of lift increased and the drag coefficient decreased which ultimately increased the lift-to-drag ratio. The jet frequency, however, did not significantly impact the aerodynamic coefficients. Even so, for most cases, the coefficients did not change much as frequency changed. The frequency of 0.8 Hz turned out to be "optimal" since it produced slightly better results compared to other frequencies.

For all the amplitudes, besides 4.0, the lift-to-drag ratio was lower than the baseline (no jet) case. Thus, for the $\alpha = 10°$, the optimal amplitude was 4.0. Figures 4.12-4.14 show the lift and drag coefficients over time for an amplitude of 4.0 and various frequencies. The synthetic jet causes periodic oscillations in lift and drag coefficients. As one can see, the oscillations are not smooth for lower frequencies which is due to the time step selected

Table 4.6: Fixed Parameters for Present Study

Case #	$\alpha(^\circ)$	x_{jet} (%C)	$\theta_{jet}(^\circ)$	L_{jet} (%C)
Case 1	10	10	28.5	0.2608
Case 2	14	43	42.5	0.2608

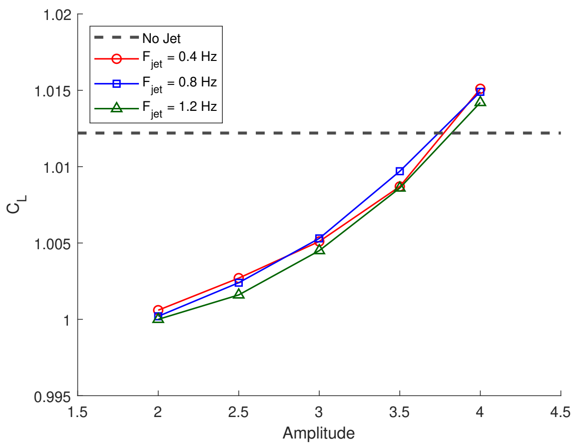

(a) Lift Coefficient

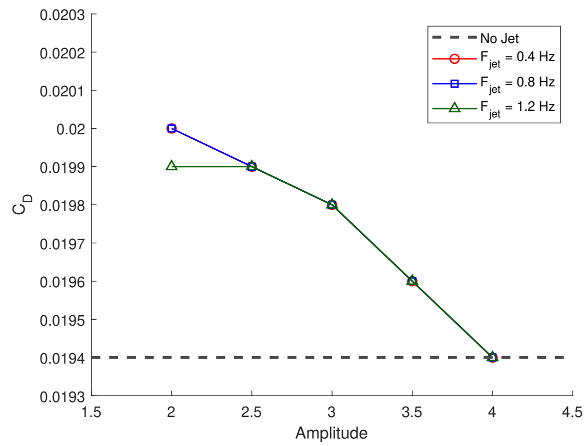

(b) Drag Coefficient

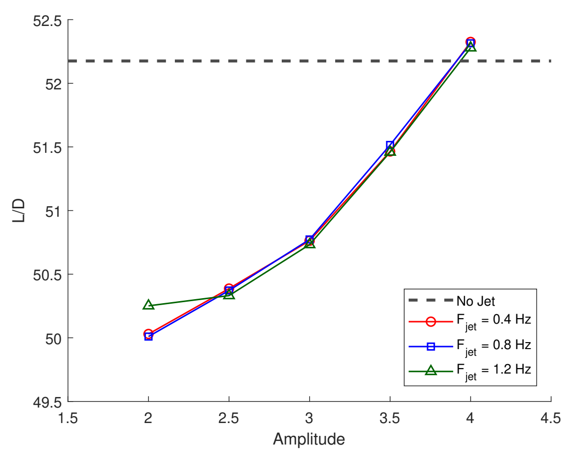

(c) Lift-to-Drag Ratio

Figure 4.11: Aerodynamic Coefficients at $\alpha = 10^\circ$

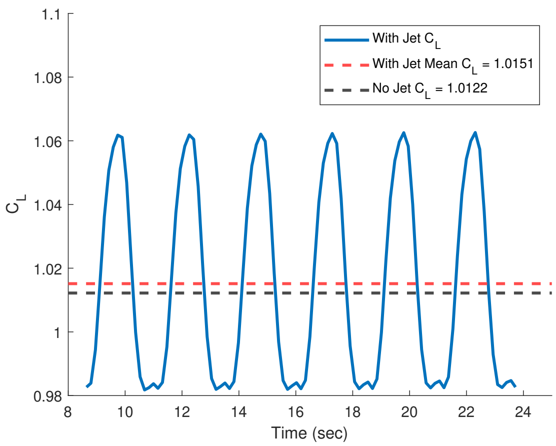

(a) Lift Coefficient

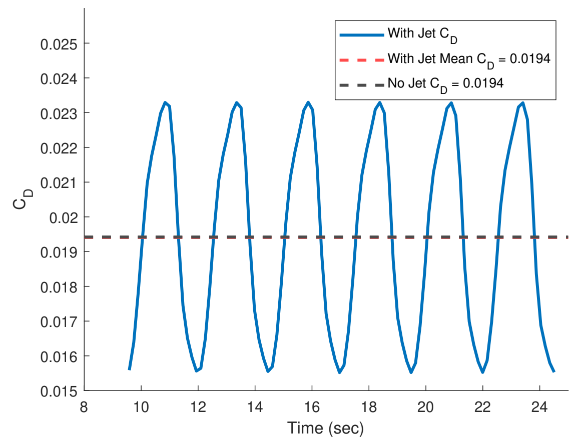

(b) Drag Coefficient

Figure 4.12: Aerodynamic Coefficients at $\alpha = 10°$ for $F_{jet} = 0.4$ Hz and A = 4.0

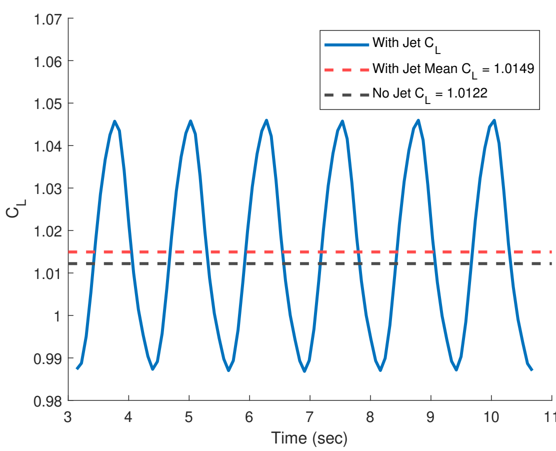

(a) Lift Coefficient

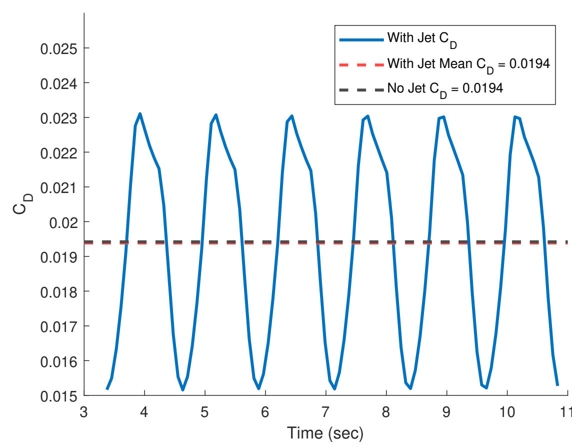

(b) Drag Coefficient

Figure 4.13: Aerodynamic Coefficients at $\alpha = 10°$ for $F_{jet} = 0.8$ Hz and A = 4.0

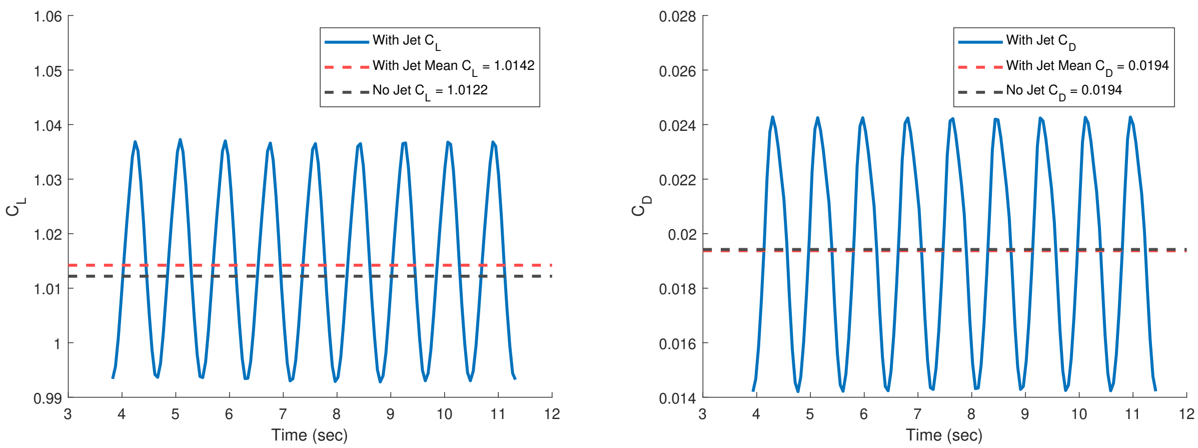

(a) Lift Coefficient **(b)** Drag Coefficient

Figure 4.14: Aerodynamic Coefficients at $\alpha = 10°$ for $F_{jet} = 1.2$ Hz and A = 4.0

for the particular case. As mentioned before, the time step was calculated based on the frequency, and as the frequency increased, the time step decreased. For consistency, the data was obtained for 100-time steps between each period, and if a lower time step was used, more accurate results can be attained. Here, only the results from the A = 4.0 is presented; plots for other amplitudes and frequencies can be seen in the appendix at the end of the document.

Figure 4.15 shows the velocity contours and streamlines for A = 4.0 and $F_{jet} = 0.8$ for one period. The cycle starts with suction, then changes to injection, and returns back to suction. The arrows at the synthetic jet represent the direction of the jet, and the size of the vector represents the magnitude of the jet velocity, i.e. the bigger the vector, the higher the velocity, and vice versa. Figures 4.16 and 4.17 the flow near the leading edge where the synthetic jet is applied. When suction happens, one can see the streamlines are detached just before the jet location, but afterward, the flow is reattached. For the injection case, at t = 12.87 s, the flow is detached post-jet slot, and this was the moment where the lift coefficient was lower and the drag coefficient was higher.

Moreover, one can find out where the separation happens by observing the wall shear stress. The location of the separation happens when the skin friction coefficient is zero. Looking at Figure 4.18, which shows the skin friction coefficient on the suction of the airfoil, the separation for flow without jet happens at 95.45% of the chord length. When injection occurs, the separation is advanced to 94.82%. However, with suction, the flow separation at the exact same location, 96.26%, as the flow without a jet.

Overall, the synthetic jet did not improve the performance much for an angle of attack of 10 degrees. This was seen by a slight improvement in the lift-to-drag ratio for the highest amplitude and a frequency of 0.8 Hz. When air was injected, the results showed a negative effect on the aerodynamic coefficients. Nonetheless, the opposite effect was seen when suction was applied to the jet, but even suction did not delay the separation point. More on how steady injection and suction affect the flow will be seen later. There are several reasons why

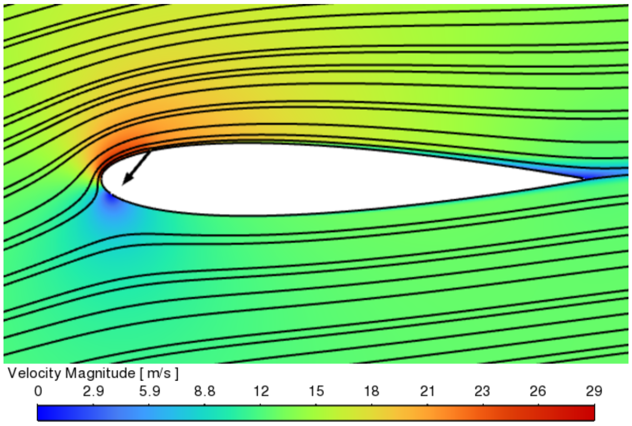

(a) t = 12.25 s

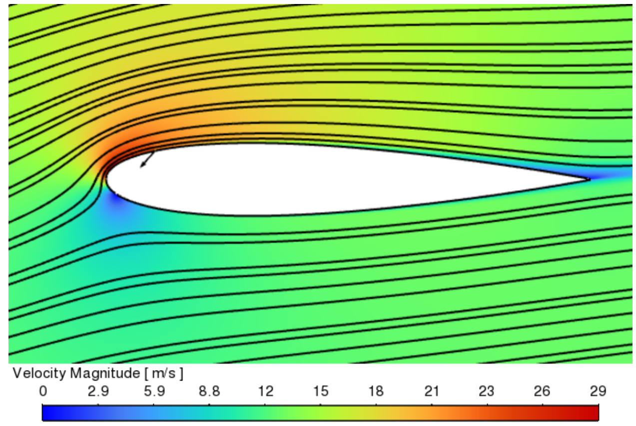

(b) t = 12.40 s

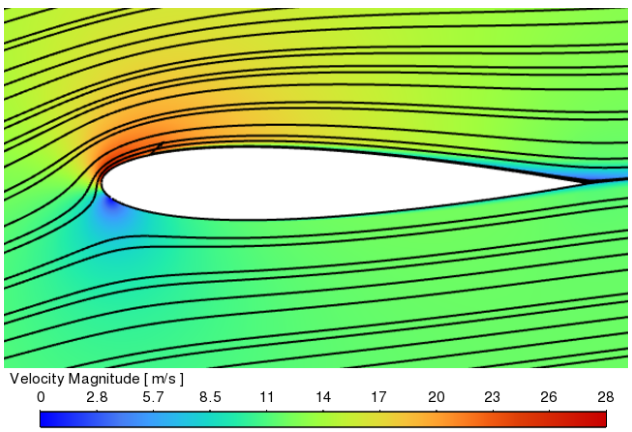

(c) t = 12.56 s

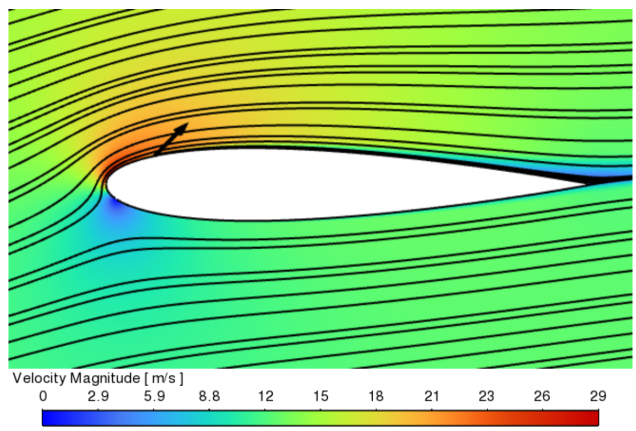

(d) t = 12.72 s

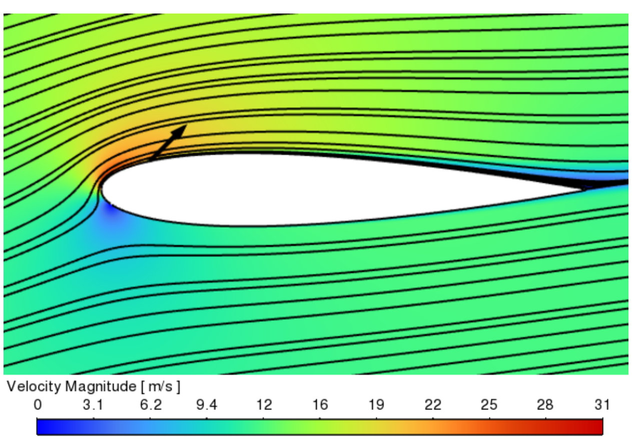

(e) t = 12.87 s

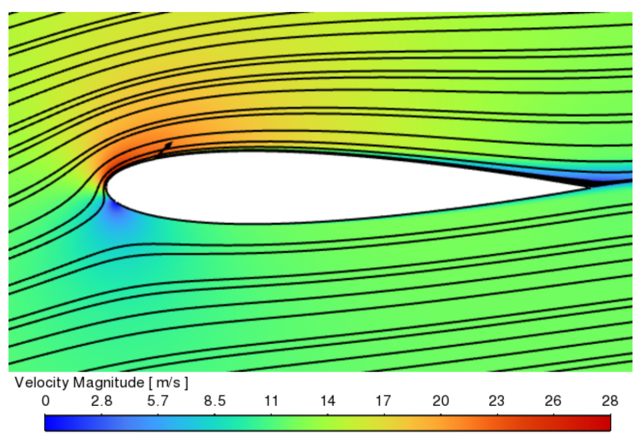

(f) t = 13.03 s

Figure 4.15: Velocity Contours at $\alpha = 10°$

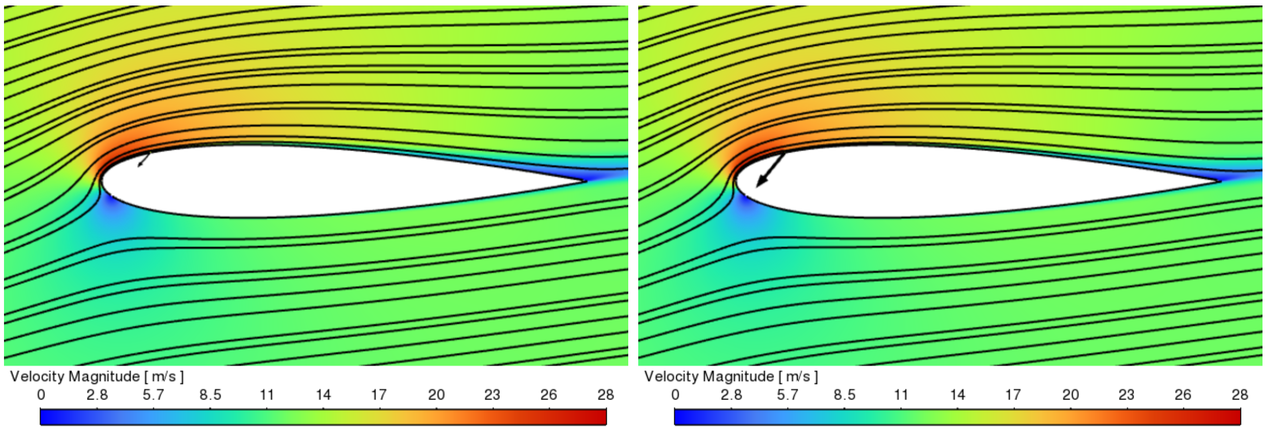

(g) t = 13.19 s

(h) t = 13.35 s

Figure 4.15: continued

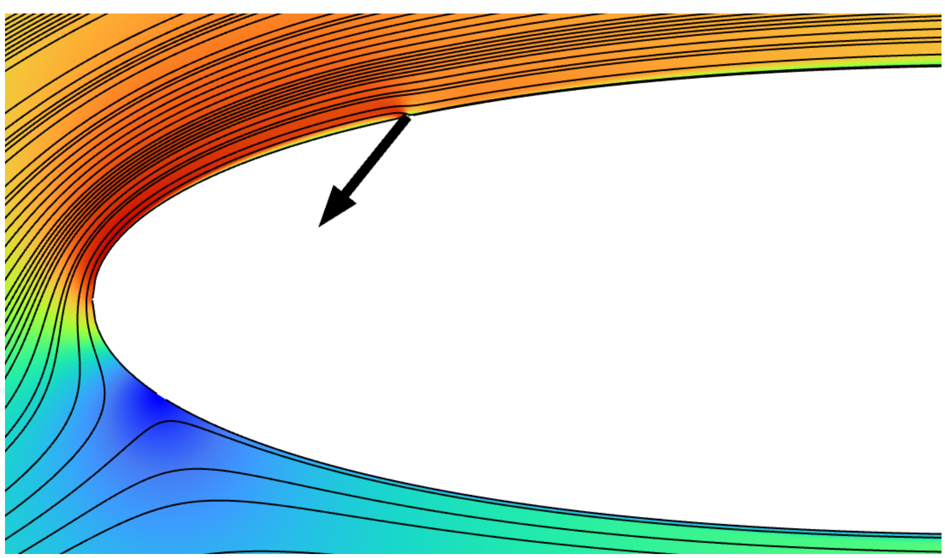

Figure 4.16: Leading Edge at t = 12.25 s for $\alpha = 10°$, $F_{jet} = 0.8$ Hz, and A = 4.0

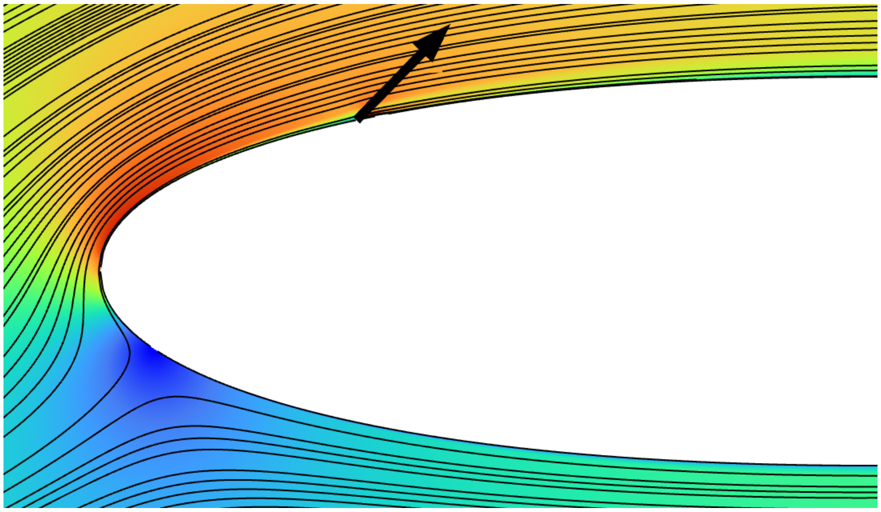

Figure 4.17: Leading Edge at t = 12.87 s for $\alpha = 10°$, $F_{jet} = 0.8$ Hz, and A = 4.0

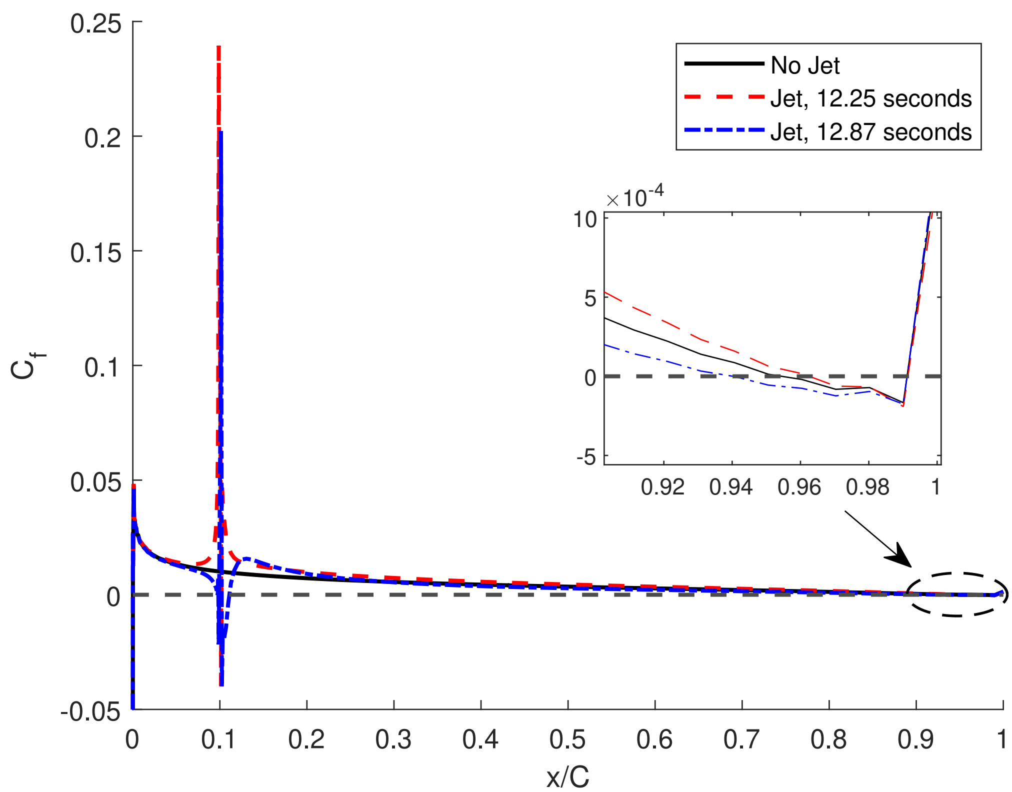

Figure 4.18: With and Without Jet Skin Friction Coefficient at $\alpha = 10°$

the synthetic jet was not optimal for this case: (1) the jet amplitude and frequency were low for this case, and maybe with higher amplitude and/or frequency, the results could be improved; (2) the jet angle and location were not were optimal for the set of amplitudes and frequencies tested, and higher aerodynamics coefficients could be achieved by varying these parameters; and (3) a rectangular profile was selected, but a parabolic profile would have been an ideal choice considering that it does not apply jet spontaneously, instead it slowly ramps up and slowly ramps down at the edges of the slots.

4.3.2 Case 2: $\alpha = 14°$

Compared to Case 1, the 14-degree angle of attack case produced better results shown by the aerodynamic coefficients in Figure 4.19. Looking at the impact of frequency, the lowest frequency produced a higher lift but also produced a higher drag compared to the other two frequencies. It was predicted that a higher frequency will produce higher lift-to-drag ratios, but in fact, the ratio was similar for all frequencies. The frequency of 0.8 Hz performed slightly better as it increased the L/D ratio by 5.39% compared to the baseline ratio while the frequencies of 0.4 Hz and 1.2 Hz increased the ratio by 5.36% and 5.38%, respectively. The impact of jet amplitude was as expected: increasing the amplitude positively impacted the lift-to-drag ratio.

The lift and drag coefficients over time are shown in Figures 4.20-4.22 for the three frequencies at A = 4.0. The plots for other amplitudes and frequencies are provided in the Appendix. Again, the oscillations are not smooth as expected which could be due to a large time step. Another reason may be that 14 degree is a stall angle of attack. This can be seen by the velocity contours, Figure 4.23, for an amplitude of 4.0 at 0.8 Hz. Even though there is some reverse flow at each time level, the flow is more separated when the jet is injecting air compared to when suction happens.

A closer look at the flow near the trailing edge confirms this statement (Figure 4.24). At 12.25 seconds suction is applied, and looking at the velocity streamlines, the flow is

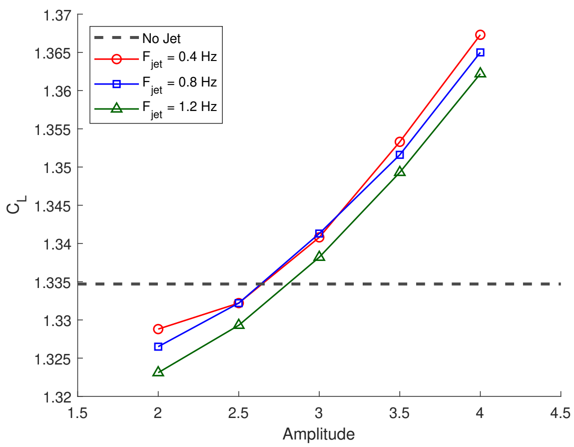

(a) Lift Coefficient

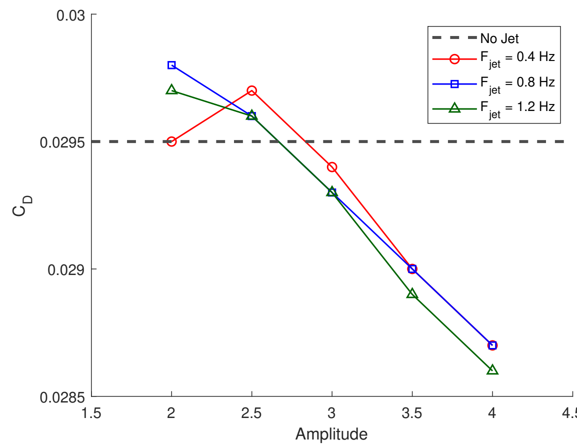

(b) Drag Coefficient

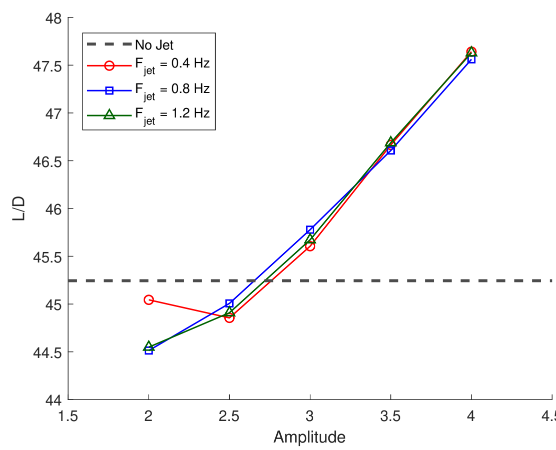

(c) Lift-to-Drag Ratio

Figure 4.19: Aerodynamic Coefficients at $\alpha = 14°$

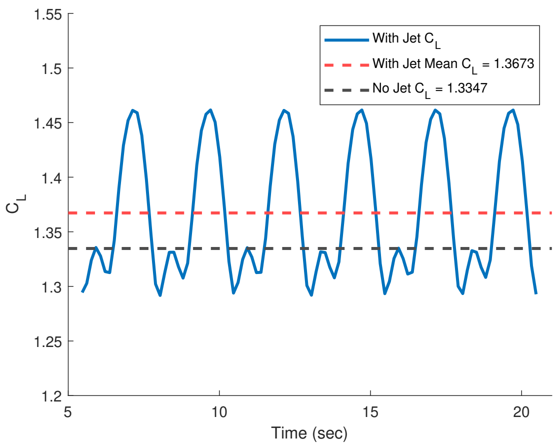

(a) Lift Coefficient

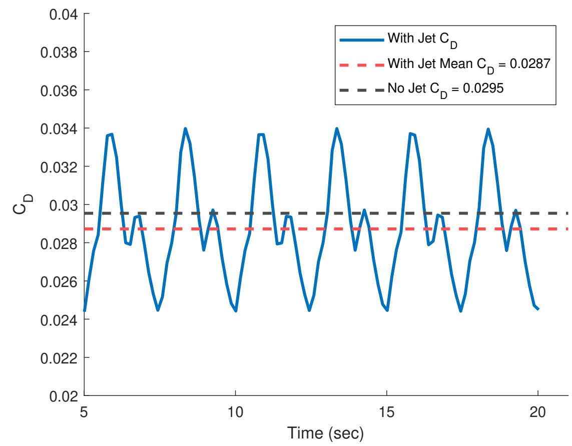

(b) Drag Coefficient

Figure 4.20: Aerodynamic Coefficients at $\alpha = 14°$ for $F_{jet} = 0.4$ Hz and A = 4.0

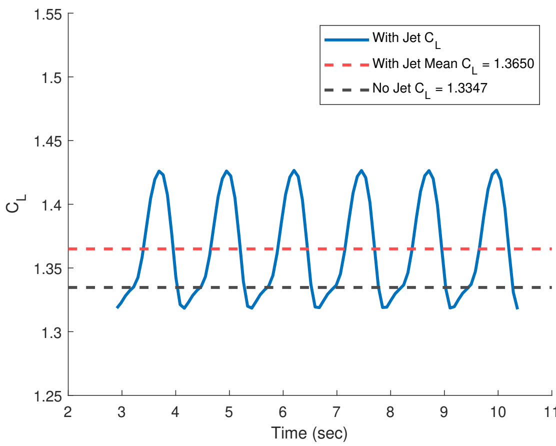

(a) Lift Coefficient

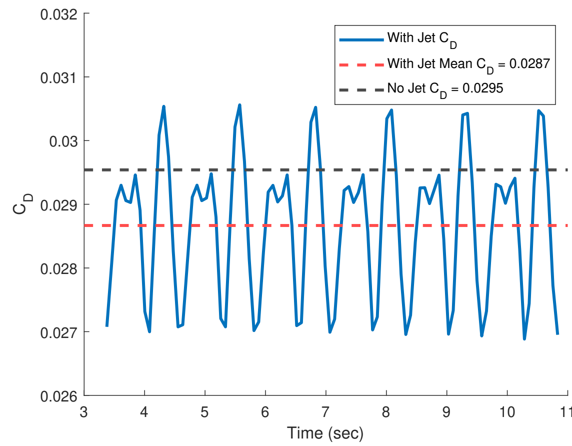

(b) Drag Coefficient

Figure 4.21: Aerodynamic Coefficients at $\alpha = 14°$ for $F_{jet} = 0.8$ Hz and A = 4.0

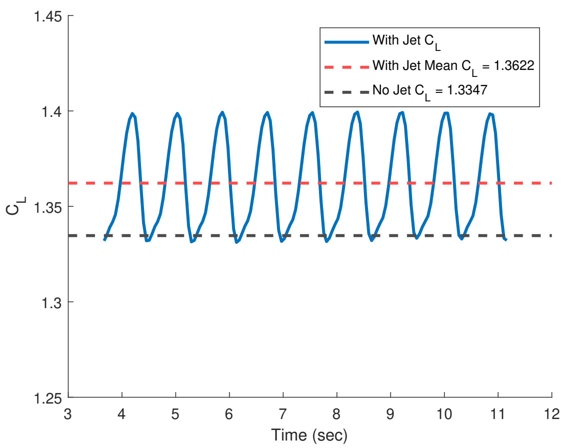

(a) Lift Coefficient

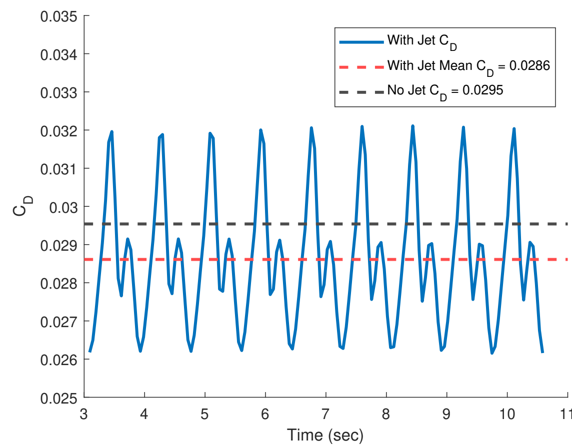

(b) Drag Coefficient

Figure 4.22: Aerodynamic Coefficients at $\alpha = 14°$ for $F_{jet} = 1.2$ Hz and A = 4.0

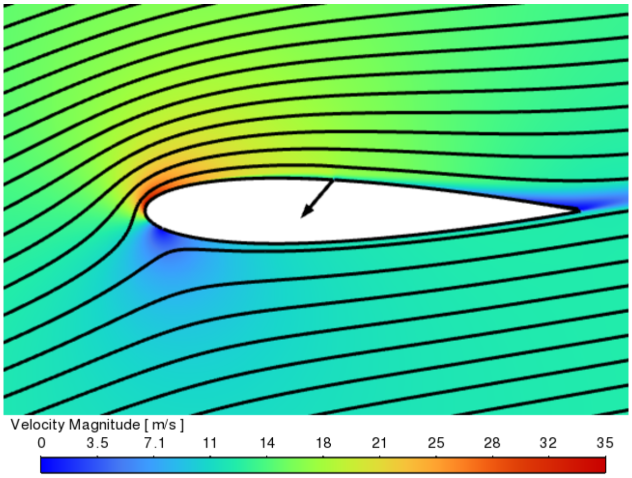

(a) t = 12.25 s

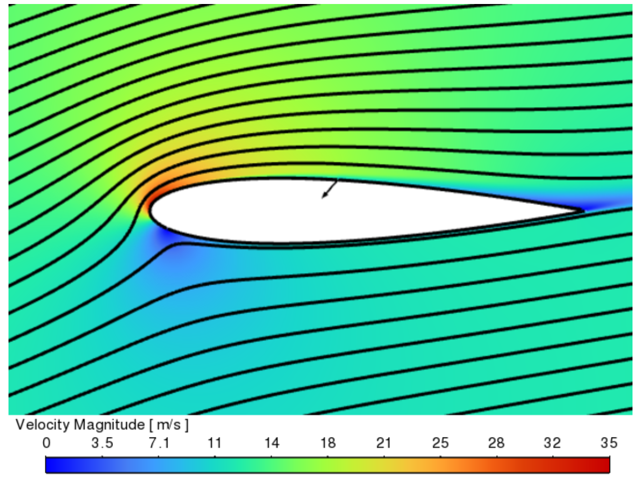

(b) t = 12.40 s

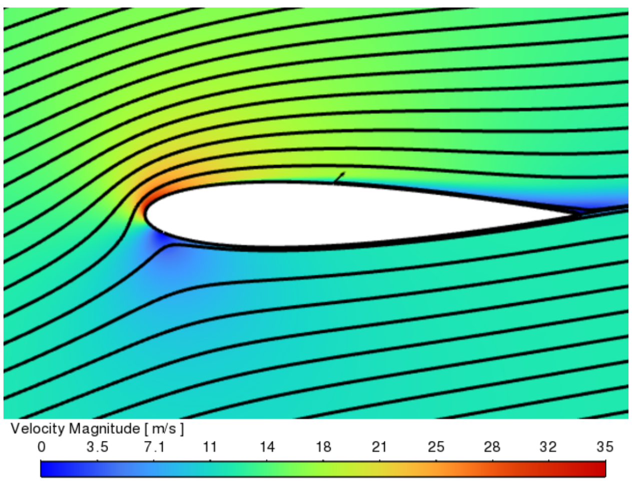

(c) t = 12.56 s

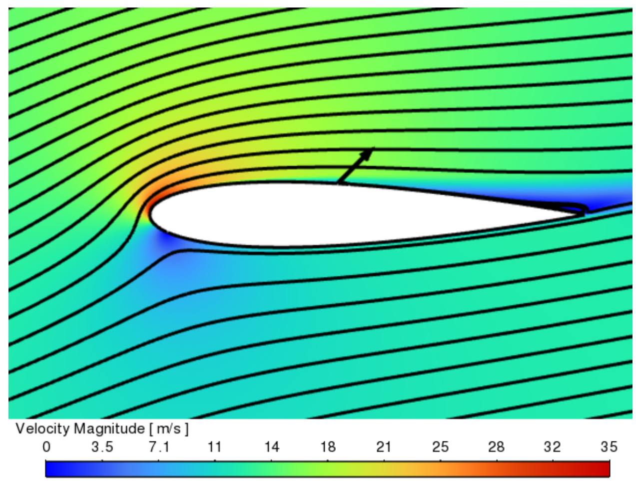

(d) t = 12.72 s

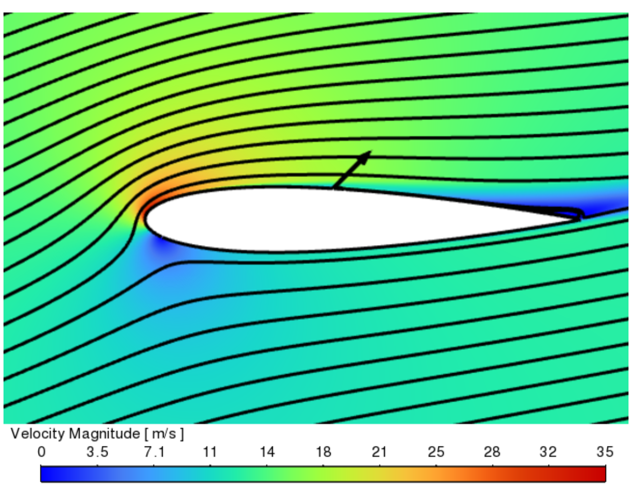

(e) t = 12.87 s

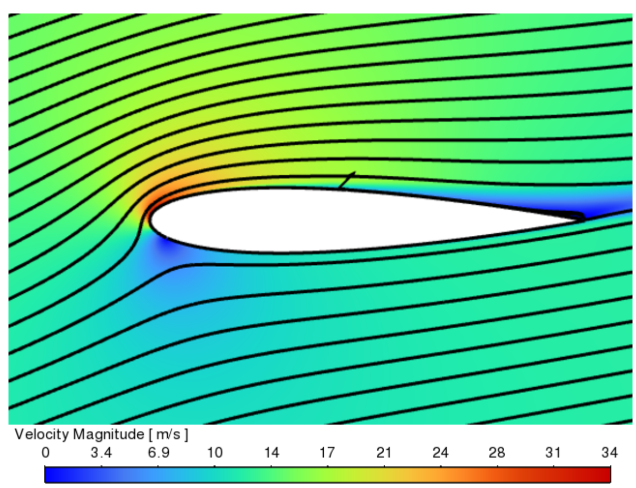

(f) t = 13.03 s

Figure 4.23: Velocity Contours at $\alpha = 14°$

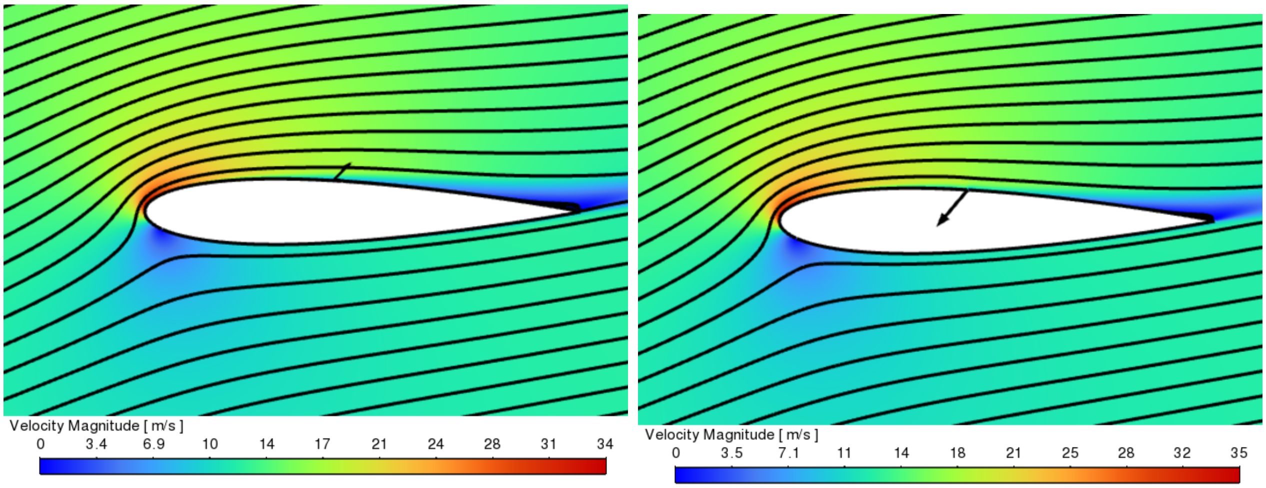

(g) t = 13.19 s

(h) t = 13.35 s

Figure 4.23: continued

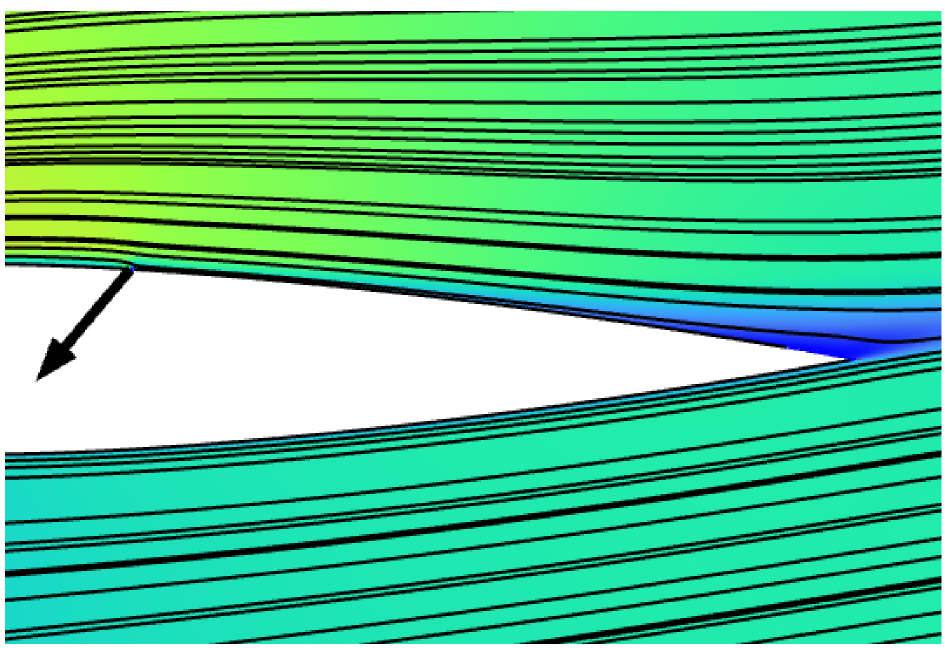

Figure 4.24: Leading Edge at t = 12.25 s for $\alpha = 14°$, $F_{jet} = 0.8$ Hz, and A = 4.0

reattached to the airfoil past the jet location. On the other hand, when the injection is applied at t = 12.87 seconds (Figure 4.25), a separation bubble can be seen at the trailing edge meaning an increase in the drag force.

Additionally, the separation location can be identified from the skin friction coefficient plot shown in Figure 4.26. The separation point for the flow without jet is located at 80.42% of the chord, but when suction happens, the separation point is moved to 89.72%. With the injection, the opposite occurs as the location is advanced to 79.30%. Since these two instances were the two extremes of the synthetic jet the average of the two locations would be the separation point of the synthetic jet. This would still be higher than 80.44% indicating that the synthetic jet will delay the flow separation.

In general, this case produced better results than Case #1. Similar to the 10-degree case, the change in frequency did not have a significant impact on the aerodynamic coefficients, and higher amplitude correlated with higher lift-to-drag ratios. Again, when suction was in play, the flow remained attached, and during injection, the flow separated. Since this case looked at a higher angle of attack, a small vortex was observed near the trailing edge, and in some instances, the vortex seemed to be "washed" away through the use of a synthetic jet.

4.4 Steady Jet Study

In the previous section, the effects of the synthetic jet on the NACA 0015 airfoil are presented where various amplitudes and frequencies were observed. Here, the steady injection and suction jet have been examined at A = 4.0 for the same angles of attack: 10° and 14°. The purpose of this study is to see if steady jets outperform synthetic jet or not. Since these are steady jets, the frequency would be zero, hence, a steady solver is utilized instead of the transient solver.

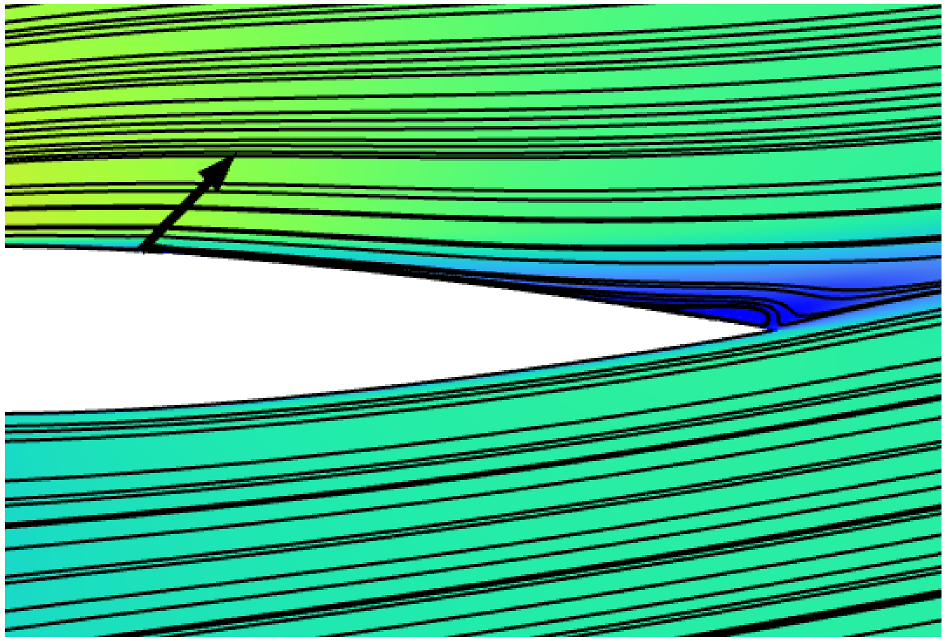

Figure 4.25: Leading Edge at t = 12.87 s for $\alpha = 14°$, $F_{jet} = 0.8$ Hz, and A = 4.0

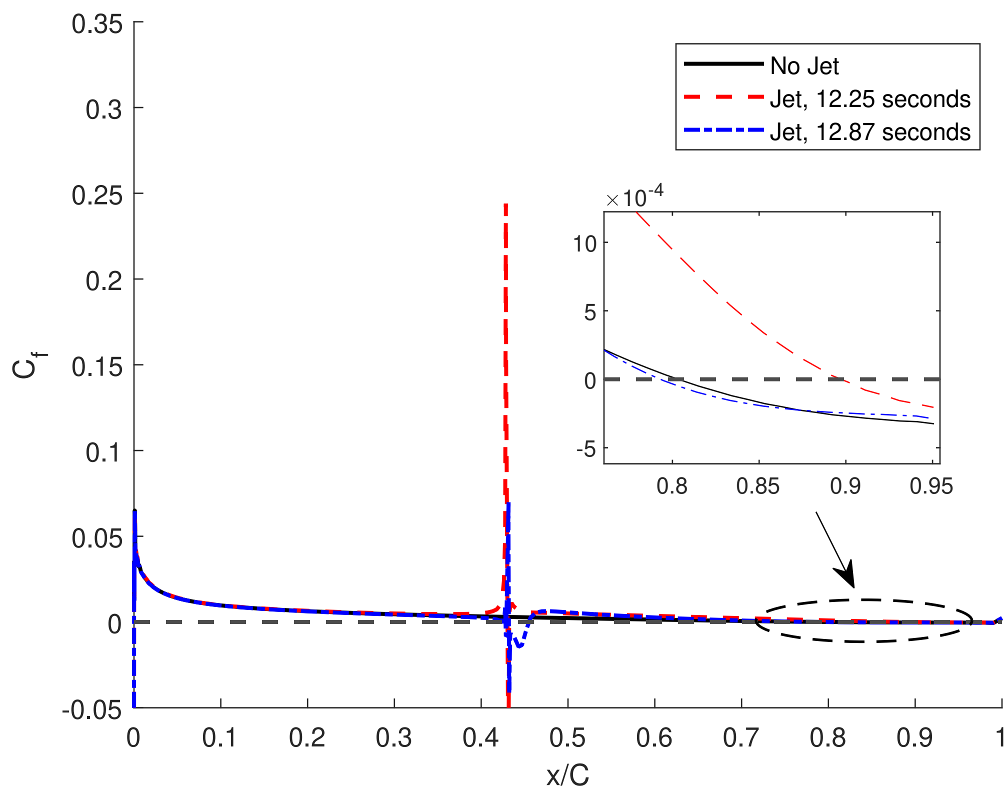

Figure 4.26: With and Without Jet Skin Friction Coefficient at $\alpha = 14°$

4.4.1 Case #1: $\alpha = 10^{\circ}$

First, the steady jet was applied to the pre-stall angle of attack. Table 4.7 shows the aerodynamic coefficients. Here, for the injection jet, the lift was lower and the drag was higher compared to the baseline case, thus, the lift-to-drag ratio was also lower. For the suction jet, the ratio increased by 53.91%; it was even significantly higher than what synthetic jet produced. The reason for this is the flow reattaches to the airfoil surface after the jet which does not cause losses due to vortex shedding. This is confirmed by the flowfield shown in Figure 4.27.

The streamlines for the injection case show that there is a small vortex forming near the trailing edge which may explain the increase in drag coefficient and decrease in lift coefficient. However, for the suction jet, the vortex disappears, and the flow remains attached. The shear stress, or the skin friction coefficient, on the airfoil, reflects this statement. From Figure 4.28, one can see, for the baseline and injection jet, the skin friction coefficient is zero about the same location, 95.45% and 95.08% of the chord length, but for suction, the skin friction coefficient is zero at 99.00%. This means the flow remains attached for the majority of the distance and only separates just before the trailing edge.

Once more, it was seen that suction performs better than injection for this certain set of parameters. This is in agreement with previously published literature [24, 29] where using suction produced higher lift-to-drag ratios than injection cases. Also, the results of both synthetic jet and steady jet show that 10 degrees may not improve the lift-to-drag ratio much unless the amplitude is quite large. On the other hand, the injection jet has shown that it responds better to smaller amplitudes [26]. So, for smaller angles of attack, a lower amplitude maybe be optimal.

Table 4.7: Aerodynamic Coefficients for Baseline and Steady Jet at $\alpha = 10°$

	C_L	C_D	L/D
No Jet	1.0122	0.0194	52.12
Injection Jet	1.0165	0.0236	43.14
Suction Jet	1.0738	0.0134	80.22

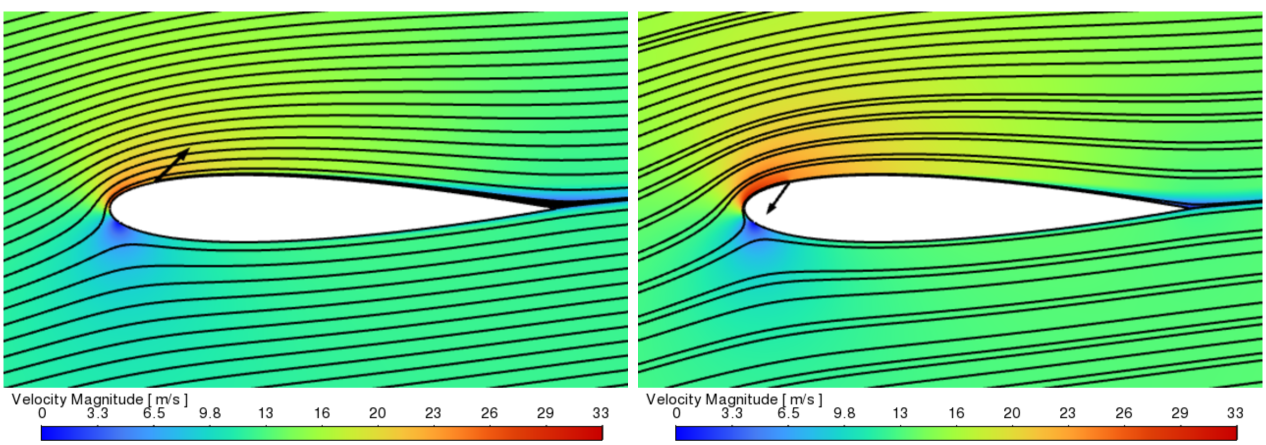

(a) Injection Jet

(b) Suction Jet

Figure 4.27: Velocity Contours of Steady Jet at $\alpha = 10°$

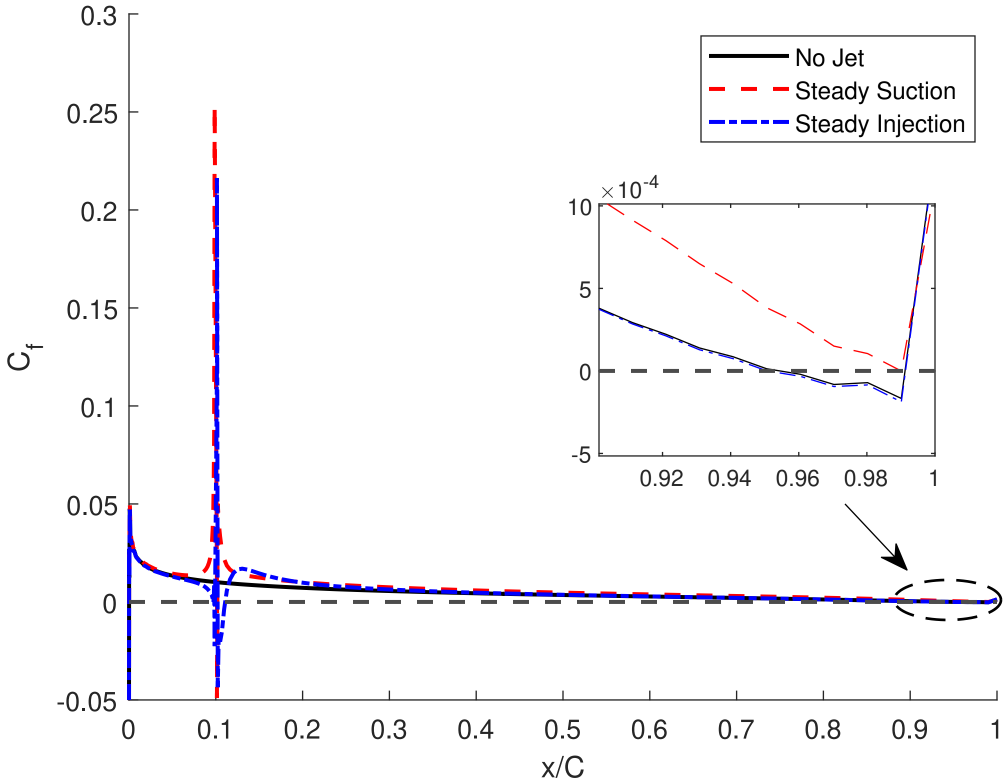

Figure 4.28: Steady Jet Skin Friction Coefficient Comparison at $\alpha = 10°$

4.4.2 Case #2: $\alpha = 14^{\circ}$

The trends for this case are similar to the previous case. With the injection jet, the lift-to-drag ratio, Table 4.8, decreased by 5.63% compared to the baseline case. One difference was here the lift coefficient increased, but the drag coefficient increased as well. As seen before, the suction jet resulted in a 42.40% increase in the lift-to-drag ratio.

Since 14 degrees is a stall angle, there may be some shedding at the trailing edge. When the injection jet is applied, the vortex is still present as seen in Figure 4.29. With a suction jet, the vortex is "washed" out. Something different from previous cases, the separation is delayed with steady injection jet from 80.42% of the chord length to 88.38%, and to 94.91% for suction jet as shown in Figure 4.30.

As seen with the synthetic jet, the selected set of amplitudes work better for the 14-degree case than the pre-stall angle case. The reason for that could be that higher amplitudes are preferable with suction and smaller amplitudes work well with injection jets as shown by Liang et. al. [26]. With smaller amplitudes, a large vortex would not form as it did here with the injection jet which would lead to both higher lift and reduction in drag.

Table 4.8: Aerodynamic Coefficients for Baseline and Steady Jet at $\alpha = 14°$

	C_L	C_D	L/D
No Jet	1.3347	0.0295	45.18
Injection Jet	1.3649	0.0320	42.64
Suction Jet	1.4832	0.0231	64.34

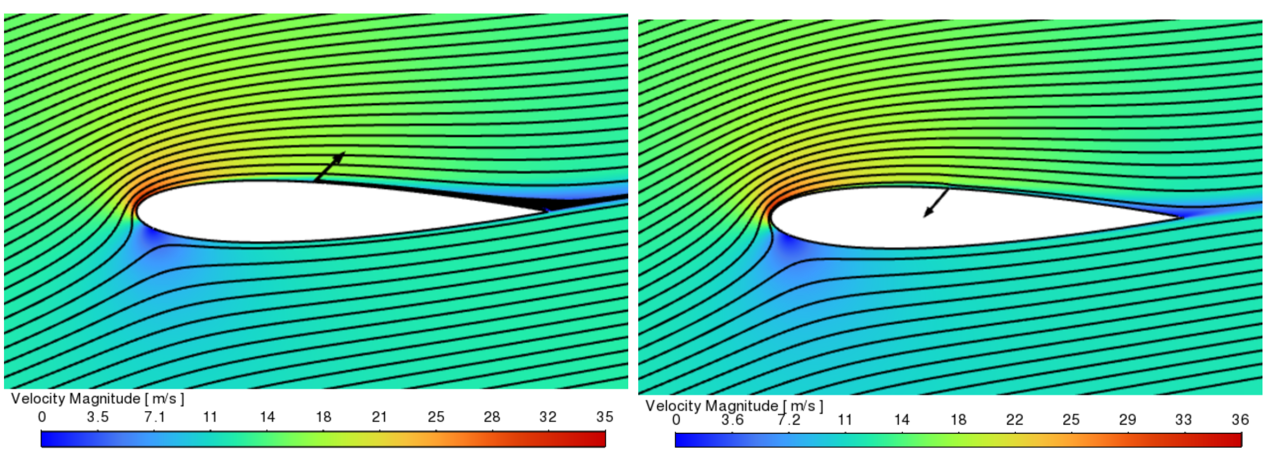

(a) Injection Jet

(b) Suction Jet

Figure 4.29: Velocity Contours of Steady Jet at $\alpha = 14°$

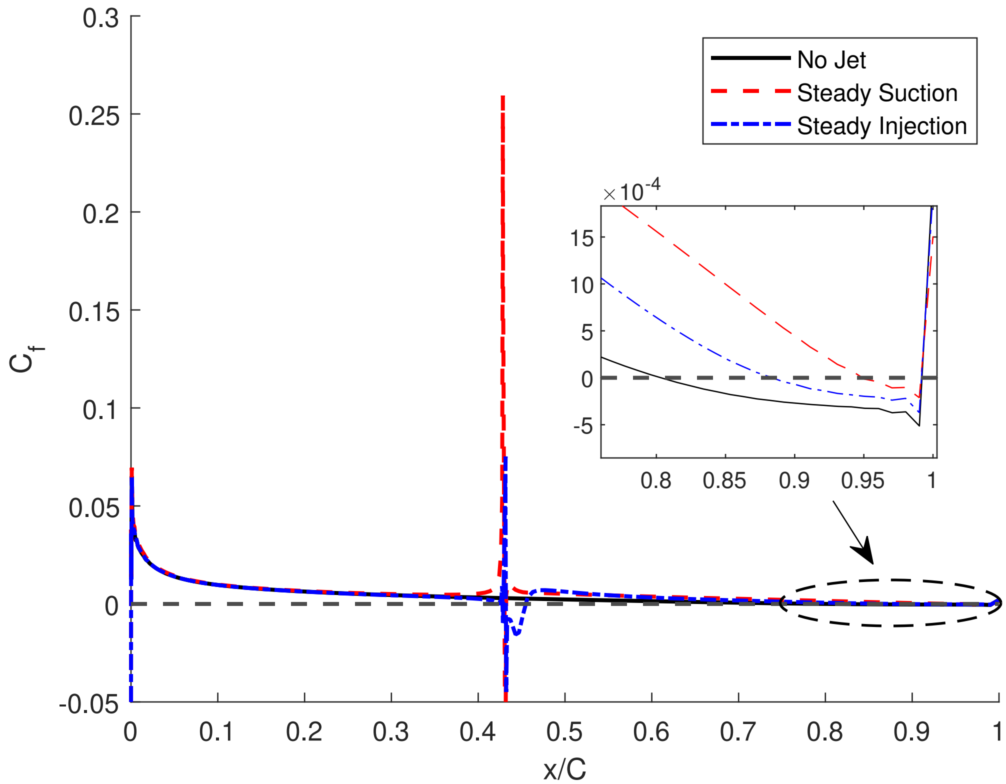

Figure 4.30: Steady Jet Skin Friction Coefficient Comparison at $\alpha = 14°$

Chapter 5: Concluding Remarks

The active flow control over NACA 0015 has been studied with the use of synthetic jets. A numerical approach was chosen to analyze the flow using the commercial CFD solver Ansys Fluent. The study was performed for various jet amplitudes and jet frequencies, while the jet location, jet angle, and jet width were fixed. Ultimately, we tried to determine which set of parameters produces the maximum lift-to-drag ratio.

First, an appropriate grid size was determined by completing a grid convergence study which showed that the mesh of size 801x201 was optimal for this study. Next, two different turbulence models were examined, and Spalart-Allmaras was selected since it was computationally cheaper as it only solves one equation. Then, Fluent solver was verified by comparing the results to those from the in-house External Flow Solver and XFOIL which showed the results were in good agreement with one another. Lastly, the implementation of the steady jet and synthetic jet and its results were compared with the studies of Goodarzi et. al. and Akcayoz. The trends were similar when the results were compared to those studies.

There were two angles of attack that were examined: (1) the pre-stall angle of 10°, and (2) the stall angle of 14°. In the first case, not much improvement was seen in the aerodynamic coefficients when the frequency was varied, and only positive improvement was seen when the jet amplitude was at the highest value of 4.0. A similar situation was seen in the second case as frequency did not make a significant impact when lift-to-drag ratios were higher, this was for jet amplitudes of 3 or higher, than the baseline results. In both cases, it was seen that a jet amplitude and jet frequency of 3.0 and 0.8 Hz, respectively, were most optimal for the selected parameters. Another significant impact of the synthetic jet that was noticed was on average, the use of synthetic jet delayed the separation location for both cases.

Additionally, a study was conducted investigating the influence of steady injection and suction jet for the two cases. In the 10 degree case, the injection jet performed substantially worse than the suction jet and did not even delay the flow from separating. Again for the 14 degrees case, the injection did not improve the lift-to-drag ratio like the suction jet did, but it did delay the flow separation by 7.74% of the chord length. For both cases, given the jet amplitude, location, angle, and width, the suction jet was most optimal more so than even the synthetic jet.

For this study, several parameters were fixed, and only the jet amplitude and frequency were varied. Here, it was seen that a jet amplitude of 4.0 produced the highest lift-to-drag ratio, but amplitudes beyond 4.0 can produce even higher ratios. This can be the goal for future studies to determine the maximum amplitude where the aerodynamic coefficients are better than the baseline case. Since only two parameters were varied for this study, for future studies, it would be beneficial to vary the other parameters as well to determine what the "true" optimal parameters are.

Bibliography

[1] Georgios Pechlivanoglou. *Passive and active flow control solutions for wind turbine blades*. PhD thesis, 01 2013. viii, 2

[2] Christopher Otto, Philipp Tewes, Jesse C. Little, and Rene Woszidlo. Comparison between fluidic oscillators and steady jets for separation control. *AIAA Journal*, 57 (12):5220–5229, 2019. doi: 10.2514/1.J058081. URL https://doi.org/10.2514/1.J058081. viii, 3, 4

[3] Rene Woszidlo, Timo Stumper, C. Nayeri, and Christian O. Paschereit. *Experimental Study on Bluff Body Drag Reduction with Fluidic Oscillators*. 2014. doi: 10.2514/6.2014-0403. URL https://arc.aiaa.org/doi/abs/10.2514/6.2014-0403. viii, 4

[4] Burak Karadag, Cem Kolbakir, and Ahmet Selim Durna. Plasma actuation effect on a naca 4412 airfoil. *Aircraft Engineering and Aerospace Technology*, 93(10):1610–1615, 2021. viii, 4

[5] Hui Tang and Shan Zhong. Incompressible flow model of synthetic jet actuators. *Aiaa Journal - AIAA J*, 44:908–912, 04 2006. doi: 10.2514/1.15633. viii, 6

[6] Ge-Cheng Zha, Wei Gao, and Craig D Paxton. Jet effects on coflow jet airfoil performance. *AIAA journal*, 45(6):1222–1231, 2007. viii, 12

[7] Mohamed Gad-el Hak. Modern developments in flow control. 1996. 1

[8] Mohamed Gad-el Hak. Flow control: The future. *Journal of Aircraft*, 38(3):402–418, 2001. doi: 10.2514/2.2796. 1

[9] MO Julius and OI Alonge. Delay of catastrophic boundary layer separation over naca 23012 airfoil; a numerical study. 1st International Conference on Engineering and Environmental Sciences, Osun . . . , 2019. 1

[10] R. Mukesh, K. Lingadurai, and U. Selvakumar. Airfoil shape optimization using non-traditional optimization technique and its validation. *Journal of King Saud University - Engineering Sciences*, 26(2):191–197, 2014. ISSN 1018-3639. doi: https://doi.org/10.1016/j.jksues.2013.04.003. URL https://www.sciencedirect.com/science/article/pii/S1018363913000159. Thermal and Micro structure Properties. 1

[11] Niels N Sørensen, F Zahle, C Bak, and T Vronsky. Prediction of the effect of vortex generators on airfoil performance. *Journal of Physics: Conference Series*, 524(1):012019, jun 2014. doi: 10.1088/1742-6596/524/1/012019. URL https://dx.doi.org/10.1088/1742-6596/524/1/012019.

[12] M. WALSH. *Turbulent boundary layer drag reduction using riblets*. doi: 10.2514/6.1982-169. URL https://arc.aiaa.org/doi/abs/10.2514/6.1982-169.

[13] Hanru Liu, Mahdi Azarpeyvand, Jinjia Wei, and Zhiguo Qu. Tandem cylinder aerodynamic sound control using porous coating. *Journal of Sound and Vibration*, 334:190–201, 2015. ISSN 0022-460X. doi: https://doi.org/10.1016/j.jsv.2014.09.013. URL https://www.sciencedirect.com/science/article/pii/S0022460X14007433. 1

[14] Martiqua Post and Thomas Corke. *Separation Control on High Angle of Attack Airfoil Using Plasma Actuators*. 2003. doi: 10.2514/6.2003-1024. URL https://arc.aiaa.org/doi/abs/10.2514/6.2003-1024. 3

[15] Ari Glezer and Michael Amitay. Synthetic jets. *Annual review of fluid mechanics*, 34(1):503–529, 2002. 5

[16] S. Scott Collis, Ronald D. Joslin, Avi Seifert, and Vassilis Theofilis. Issues in active flow control: theory, control, simulation, and experiment. *Progress in Aerospace Sciences*, 40(4):237–289, 2004. ISSN 0376-0421. doi: https://doi.org/10.1016/

j.paerosci.2004.06.001. URL https://www.sciencedirect.com/science/article/pii/S0376042104000405. 5

[17] Lars Koop, Klaus Ehrenfried, Andreas Dillmann, and U. Michel. *Reduction of Flap Side Edge Noise by Active Flow Control*. 2002. doi: 10.2514/6.2002-2469. URL https://arc.aiaa.org/doi/abs/10.2514/6.2002-2469. 5

[18] Michael A. Niestroy, David R. Williams, and Jurgen Seidel. *NATO AVT-239 Task Group: Active Flow Control Simulation of the Tailless ICE Aircraft*. 2019. 5

[19] Frederico Rodrigues, José Páscoa, and Filipe Dias. Power consumption characterization of dbd plasma actuators for boundary layer control. 12 2015. 7

[20] Richard Anderson and Subrata Roy. *Preliminary Experiments of Barrier Discharge Plasma Actuators using Dry and Humid Air*. 2006. doi: 10.2514/6.2006-369. URL https://arc.aiaa.org/doi/abs/10.2514/6.2006-369. 7

[21] Michael Wicks and Flint O. Thomas. Effect of relative humidity on dielectric barrier discharge plasma actuator body force. *AIAA Journal*, 53(9):2801–2805, 2015. doi: 10.2514/1.J053810. 7

[22] Jason O Burkholder, Gang Tao, Douglas R Smith, Timothy H Cox, and Christopher J Miller. Active flow control with adaptive design techniques for improved aircraft safety. *CONTRACT*, 2009. 7

[23] Jiri Blazek. *Computational Fluid Dynamics: Principles and Applications (Third Edition)*. Butterworth-Heinemann, 2015. 8

[24] L. Huang, P. G. Huang, R. P. LeBeau, and T. Hauser. Numerical study of blowing and suction control mechanism on naca0012 airfoil. *Journal of Aircraft*, 41(5):1005–1013, 2004. doi: 10.2514/1.2255. URL https://doi.org/10.2514/1.2255. 8, 58

[25] Kianoosh Yousefi and Reza Saleh. The effects of trailing edge blowing on aerodynamic characteristics of the naca 0012 airfoil and optimization of the blowing slot geometry. *Journal of Theorical and Applied Mechanics*, 52:165–179, 2014. 8

[26] Chua Bing Liang, Akmal Nizam Mohammed, Azwan Sapit, Mohd Azahari Razali, Mohd Faisal Hushim, Amir Khalid, and Nurul Farhana Mohd Yusof. Numerical simulation of aerofoil with flow injection at the upper surface. *CFD Letters*, 12(1): 98–110, Jan. 2021. URL https://www.akademiabaru.com/submit/index.php/cfdl/article/view/3133. 9, 58, 61

[27] Amrani Djedjiga, B. Imine, and L. Adjlout. Numerical investigation of flow control on naca4415 airfoil. 8:2321–9009, 01 2020. 9

[28] R Azim, MM Hasan, and Mohammad Ali. Numerical investigation on the delay of boundary layer separation by suction for naca 4412. *Procedia Engineering*, 105:329–334, 2015. 10

[29] Mustafa Genç and Ünver Kaynak. Control of flow separation and transition point over an aerofoil at low re number using simultaneous blowing and suction. In *19th AIAA Computational Fluid Dynamics*, page 3672. 2009. 10, 27, 58

[30] R Abinav, Nandu R Nair, P Sravan, Pradeesh Kumar, and SR Nagaraja. Cfd analysis of co flow jet airfoil. *Indian Journal of Science and Technology*, 9(45), 2016. 11

[31] Srinivasan Siddhamoorthy, Shreesha M., Tanveer Ahmed, and G. Sanjana. Numerical and experimental investigation of co-flow jet technique in clarky-m18 aerofoil. *SSRN Electronic Journal*, 01 2019. doi: 10.2139/ssrn.3511937. 11

[32] TL Chng, A Rachman, HM Tsai, and Ge-Cheng Zha. Flow control of an airfoil via injection and suction. *Journal of Aircraft*, 46(1):291–300, 2009. 11

[33] James Julian, Waridho Iskandar, and Fitri Wahyuni. Aerodynamics improvement of naca 0015 by using co-flow jet. *International Journal of Marine Engineering Innovation and Research*, 7(4), 2022. 11

[34] Mehdi Sheikh Goodarzi, Mojtaba Rahimi, and R. Fereidouni. Investigation of active flow control over naca0015 airfoil via blowing. *Journal of the Aerospace Sciences*, 1: 57–63, 2012. 11, 27, 32

[35] V Kitsios, R Kotapati, R Mittal, A Ooi, J Soria, and D You. Numerical simulation of lift enhancement on a naca 0015 airfoil using znmf jets. In *Proceedings of the Summer Program*, page 457. Citeseer, 2006. 11

[36] A Tuck and J Soria. Micro-jets flow control at the leading edge of a naca 0015 airfoil. In *Proceeding of 1st Forum in Flow Control*, 2004. 13

[37] Eray Akçayöz. Numerical investigation of flow control over an airfoil with synthetic jets and its optimization. Master's thesis, Middle East Technical University, 2008. 13, 26, 32

[38] E Montazer, M Mirzaei, E Salami, TA Ward, FI Romli, and SN Kazi. Optimization of a synthetic jet actuator for flow control around an airfoil. In *IOP Conference Series: Materials Science and Engineering*, volume 152, page 012023. IOP Publishing, 2016. 13

[39] T Parthasarathy and SP Das. Some aspects of flow control over a naca0015 airfoil using synthetic jets. In *Journal of Physics: Conference Series*, volume 822, page 012009. IOP Publishing, 2017. 14

[40] Klaus A Hoffmann and Steve T Chiang. Computational fluid dynamics volume iii. *Engineering education system*, 2000. 16

[41] Jorge E Bardina, Peter G Huang, and Thomas J Coakley. Turbulence modeling validation, testing, and development. Technical report, 1997. 17

[42] P. SPALART and S. ALLMARAS. *A one-equation turbulence model for aerodynamic flows*. 1992. doi: 10.2514/6.1992-439. URL https://arc.aiaa.org/doi/abs/10.2514/6.1992-439. 17

[43] Sarah Hope-Swain. Airfoilgenerator. https://github.com/pointwise/AirfoilGenerator, 2021. Accessed on February 15, 2023. 19

[44] Robert E Dannenberg and James A Weiberg. Section characteristics of a 10.5-percent-thick airfoil with area suction as affected by chordwise distribution of permeability. Technical report, 1952. 26

[45] Florian Menter and Christopher Rumsey. Assessment of two-equation turbulence models for transonic flows. In *Fluid Dynamics Conference*, page 2343, 1994. 29

[46] Florian R Menter. Two-equation eddy-viscosity turbulence models for engineering applications. *AIAA journal*, 32(8):1598–1605, 1994. 29

[47] David C Wilcox. Reassessment of the scale-determining equation for advanced turbulence models. *AIAA journal*, 26(11):1299–1310, 1988. 29

[48] R E Sheldahl and P C Klimas. Aerodynamic characteristics of seven symmetrical airfoil sections through 180-degree angle of attack for use in aerodynamic analysis of vertical axis wind turbines. doi: 10.2172/6548367. URL https://www.osti.gov/biblio/6548367. 32

[49] Mark Drela. Xfoil: An analysis and design system for low reynolds number airfoils. https://web.mit.edu/drela/Public/web/xfoil/, 2022. Accessed on February 15, 2023. 34

Appendix

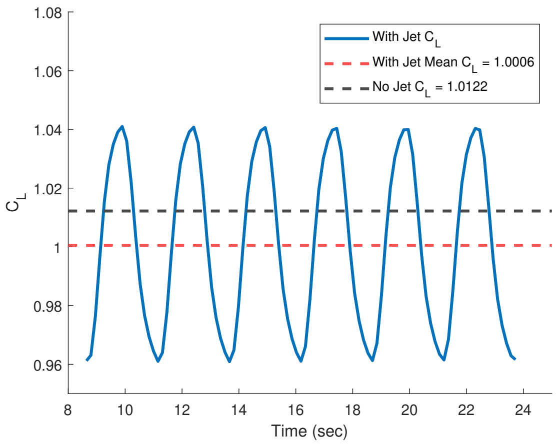

(a) Lift Coefficient

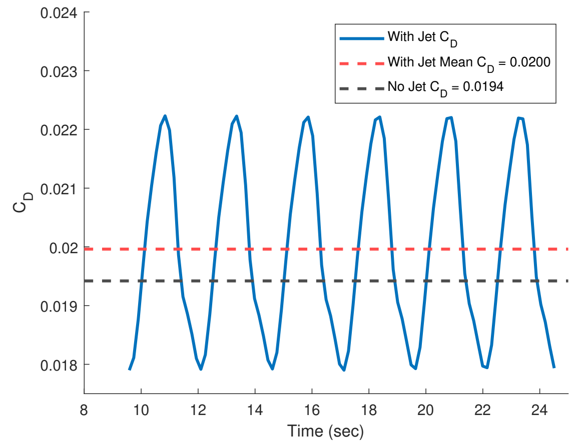

(b) Drag Coefficient

Figure 1: Aerodynamic Coefficients at $\alpha = 10°$ for $F_{jet} = 0.4$ Hz and A = 2.0

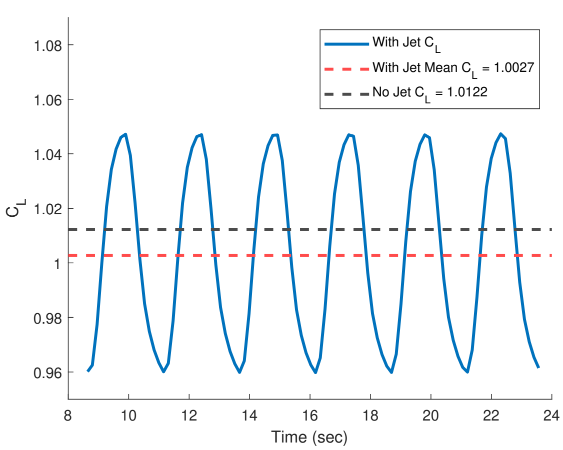

(a) Lift Coefficient

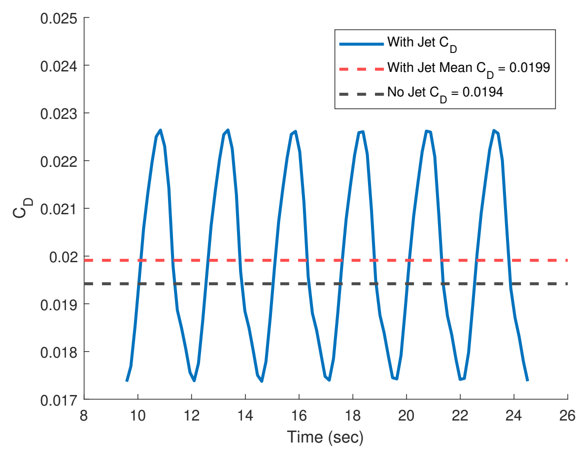

(b) Drag Coefficient

Figure 2: Aerodynamic Coefficients at $\alpha = 10°$ for $F_{jet} = 0.4$ Hz and A = 2.5

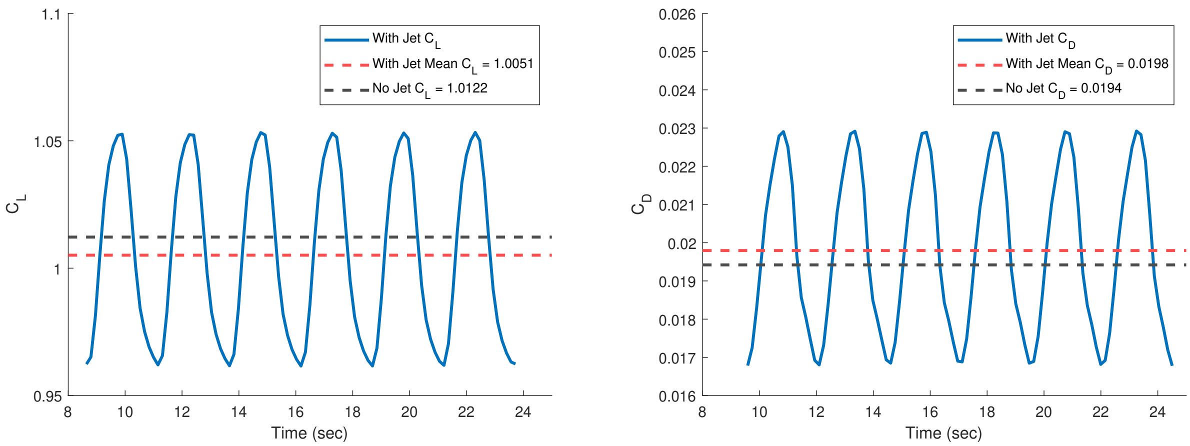

(a) Lift Coefficient **(b)** Drag Coefficient

Figure 3: Aerodynamic Coefficients at $\alpha = 10°$ for $F_{jet} = 0.4$ Hz and A = 3.0

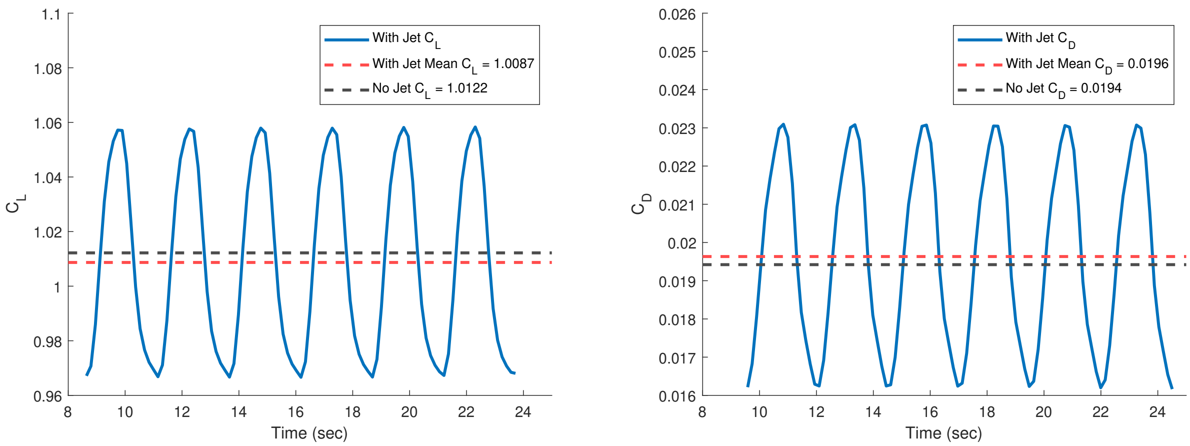

(a) Lift Coefficient **(b)** Drag Coefficient

Figure 4: Aerodynamic Coefficients at $\alpha = 10°$ for $F_{jet} = 0.4$ Hz and A = 3.5

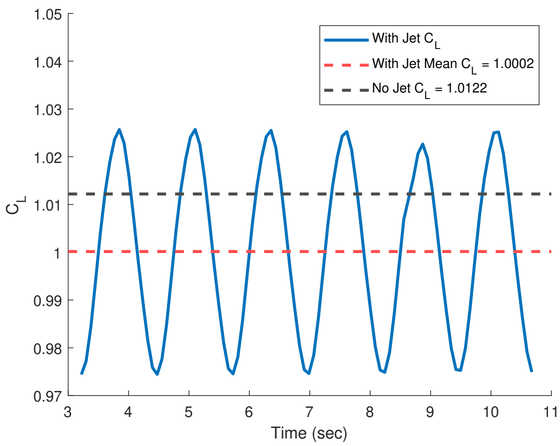

(a) Lift Coefficient

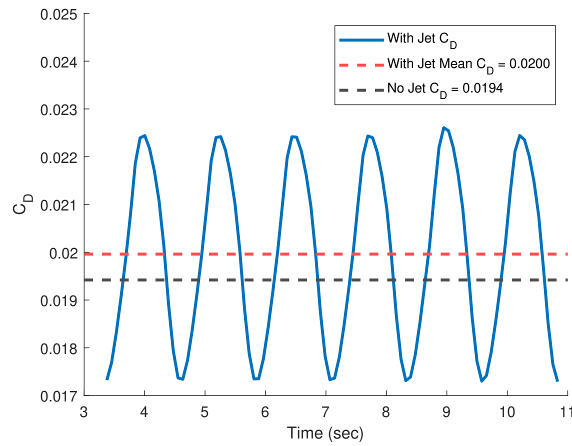

(b) Drag Coefficient

Figure 5: Aerodynamic Coefficients at $\alpha = 10°$ for $F_{jet} = 0.8$ Hz and A $= 2.0$

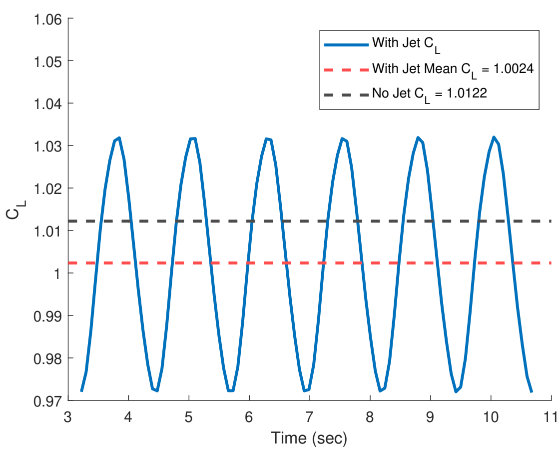

(a) Lift Coefficient

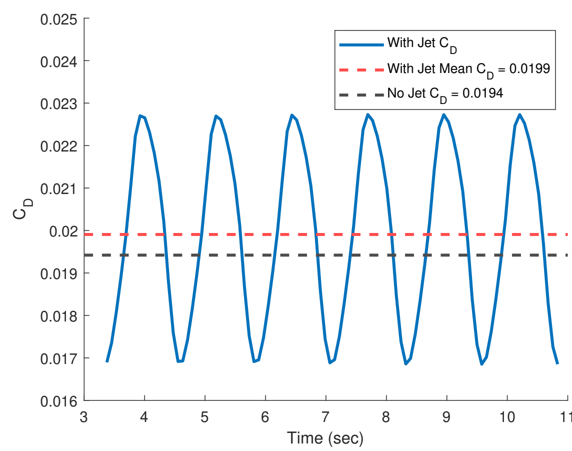

(b) Drag Coefficient

Figure 6: Aerodynamic Coefficients at $\alpha = 10°$ for $F_{jet} = 0.8$ Hz and A $= 2.5$

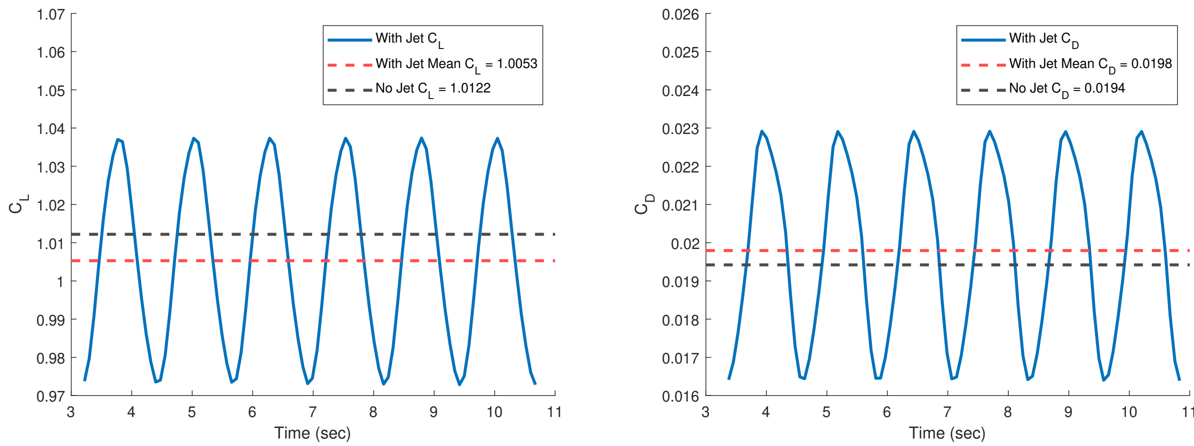

(a) Lift Coefficient **(b)** Drag Coefficient

Figure 7: Aerodynamic Coefficients at $\alpha = 10°$ for $F_{jet} = 0.8$ Hz and A $= 3.0$

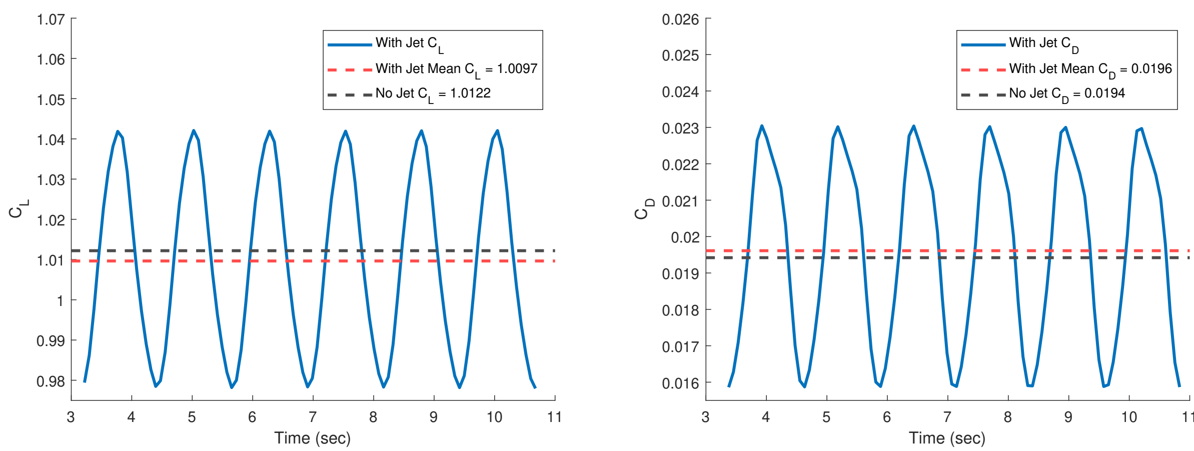

(a) Lift Coefficient **(b)** Drag Coefficient

Figure 8: Aerodynamic Coefficients at $\alpha = 10°$ for $F_{jet} = 0.8$ Hz and A $= 3.5$

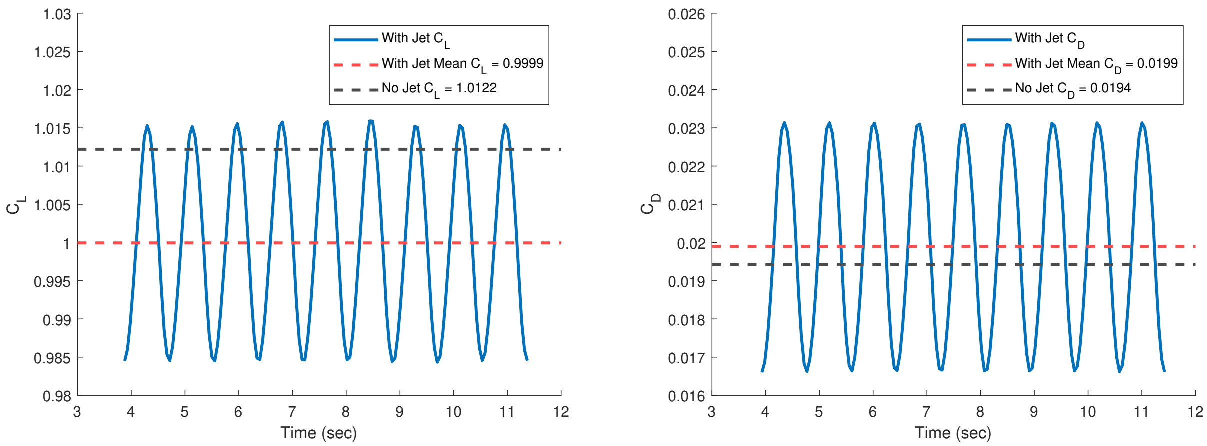

(a) Lift Coefficient **(b)** Drag Coefficient

Figure 9: Aerodynamic Coefficients at $\alpha = 10°$ for $F_{jet} = 1.2$ Hz and A = 2.0

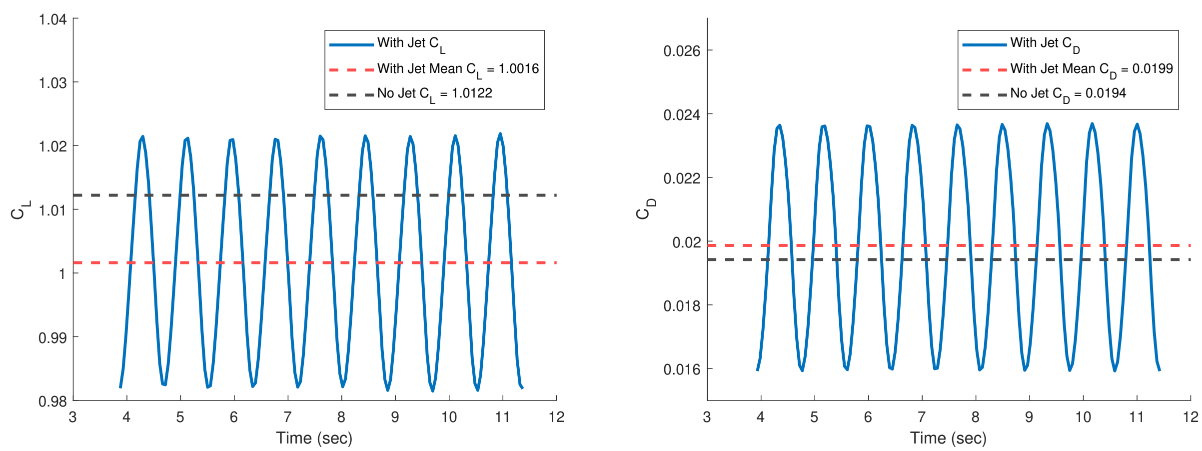

(a) Lift Coefficient **(b)** Drag Coefficient

Figure 10: Aerodynamic Coefficients at $\alpha = 10°$ for $F_{jet} = 1.2$ Hz and A = 2.5

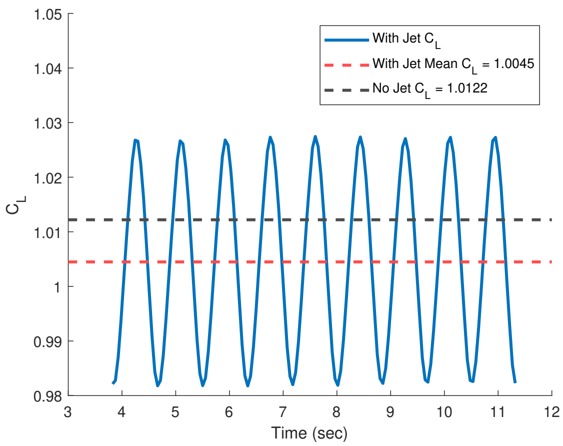

(a) Lift Coefficient

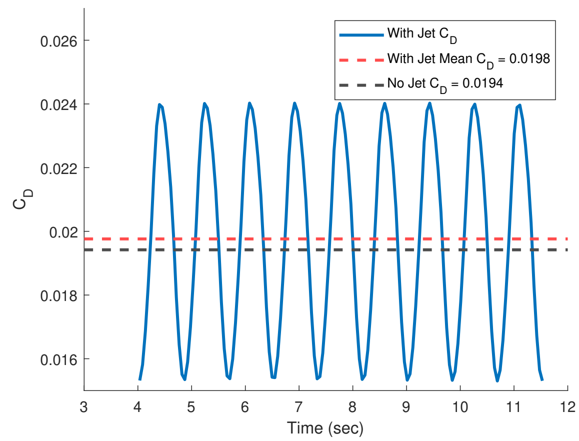

(b) Drag Coefficient

Figure 11: Aerodynamic Coefficients at $\alpha = 10°$ for F_{jet} = 1.2 Hz and A = 3.0

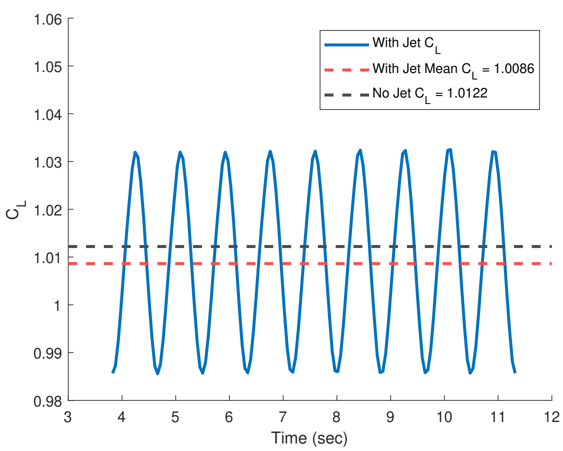

(a) Lift Coefficient

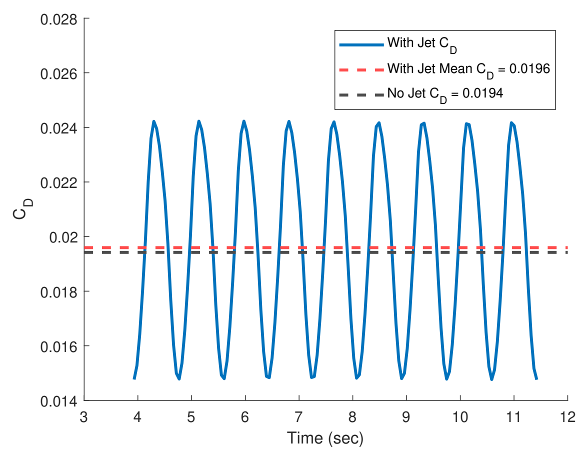

(b) Drag Coefficient

Figure 12: Aerodynamic Coefficients at $\alpha = 10°$ for F_{jet} = 1.2 Hz and A = 3.5

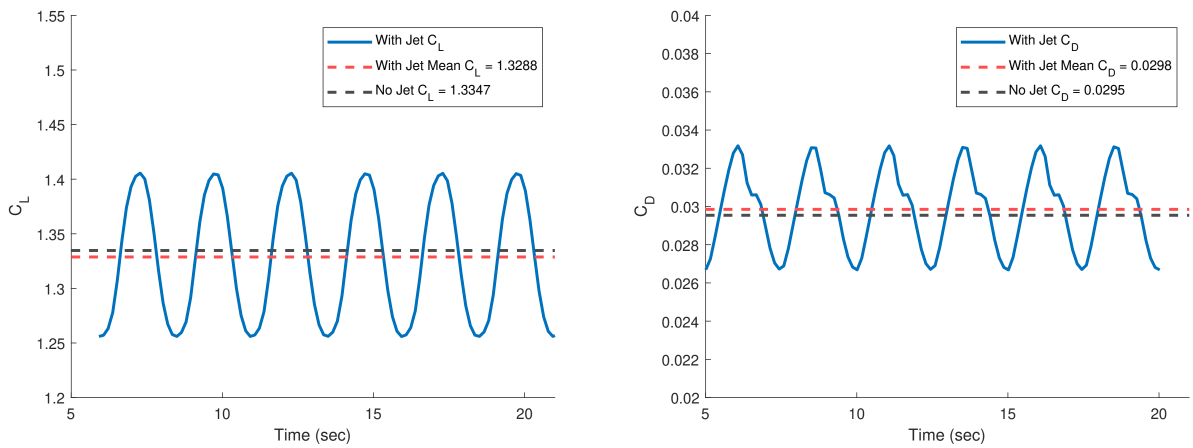

(a) Lift Coefficient **(b)** Drag Coefficient

Figure 13: Aerodynamic Coefficients at $\alpha = 14°$ for $F_{jet} = 0.4$ Hz and A = 2.0

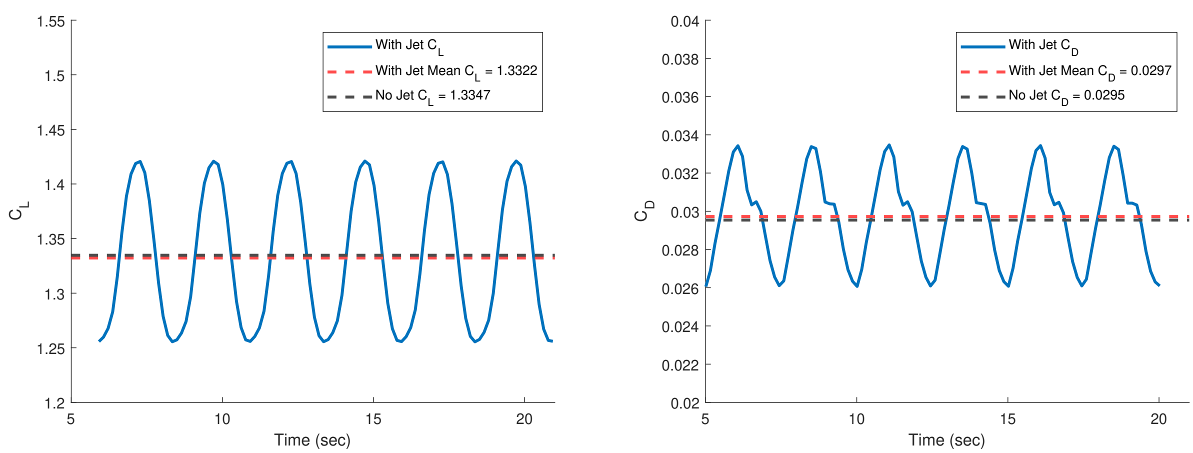

(a) Lift Coefficient **(b)** Drag Coefficient

Figure 14: Aerodynamic Coefficients at $\alpha = 14°$ for $F_{jet} = 0.4$ Hz and A = 2.5

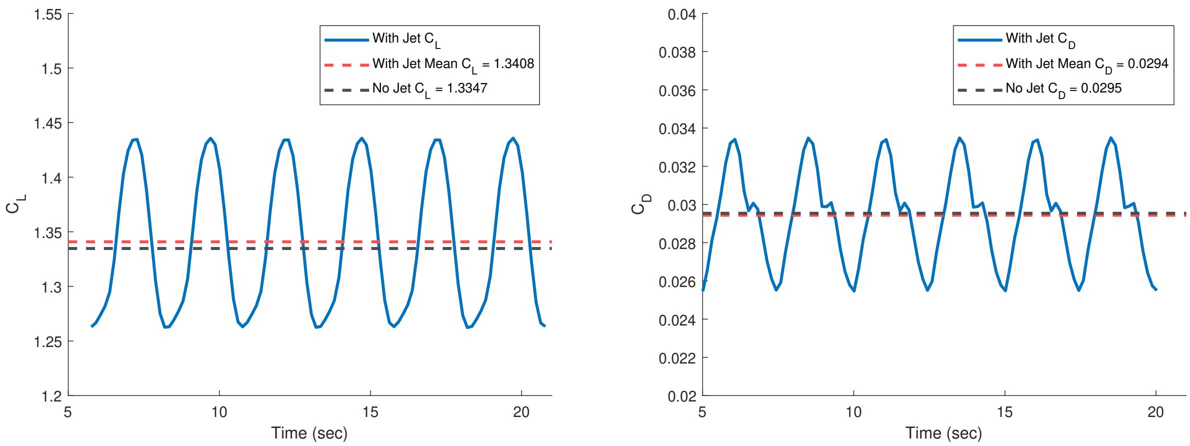

(a) Lift Coefficient **(b)** Drag Coefficient

Figure 15: Aerodynamic Coefficients at $\alpha = 14°$ for $F_{jet} = 0.4$ Hz and A = 3.0

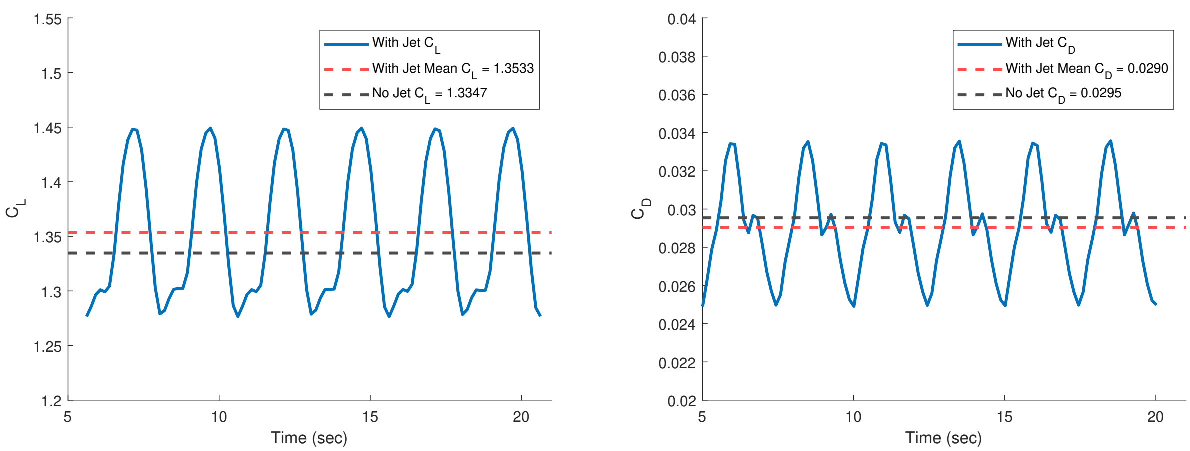

(a) Lift Coefficient **(b)** Drag Coefficient

Figure 16: Aerodynamic Coefficients at $\alpha = 14°$ for $F_{jet} = 0.4$ Hz and A = 3.5

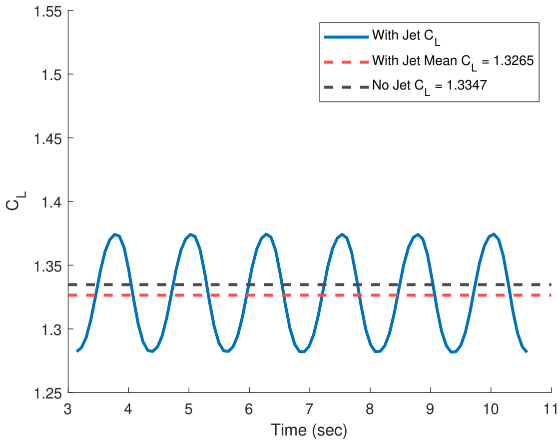

(a) Lift Coefficient

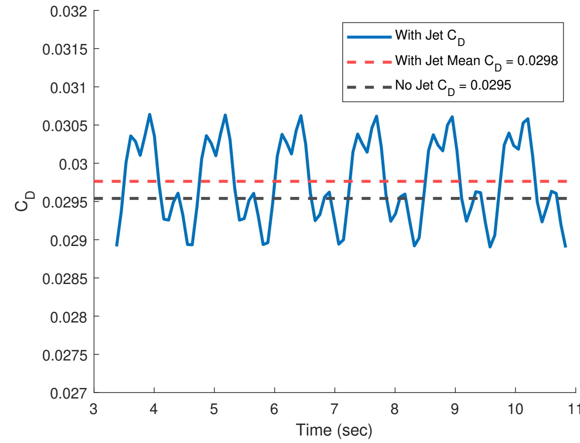

(b) Drag Coefficient

Figure 17: Aerodynamic Coefficients at $\alpha = 14°$ for $F_{jet} = 0.8$ Hz and A = 2.0

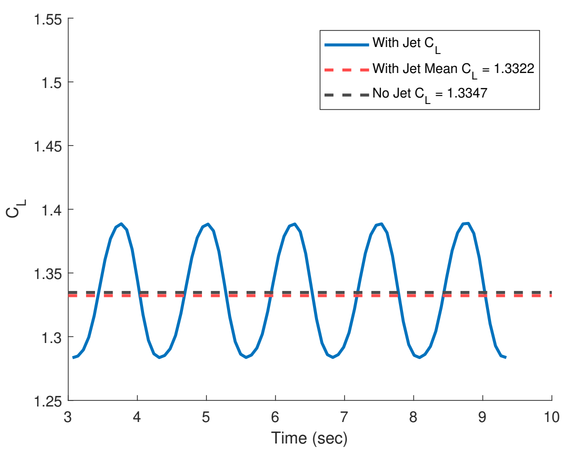

(a) Lift Coefficient

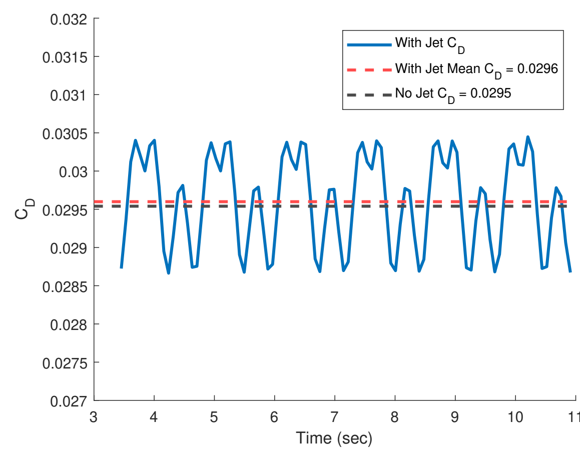

(b) Drag Coefficient

Figure 18: Aerodynamic Coefficients at $\alpha = 14°$ for $F_{jet} = 0.8$ Hz and A = 2.5

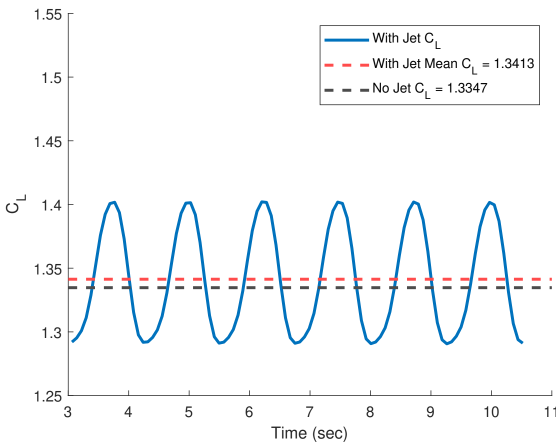

(a) Lift Coefficient

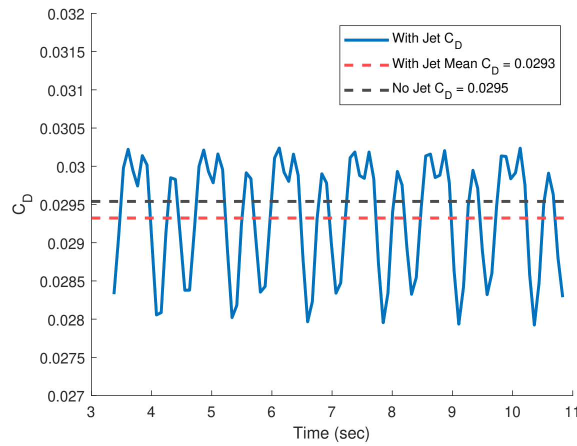

(b) Drag Coefficient

Figure 19: Aerodynamic Coefficients at $\alpha = 14°$ for F_{jet} = 0.8 Hz and A = 3.0

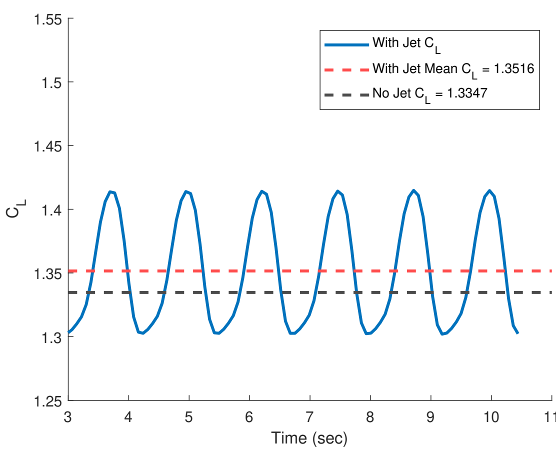

(a) Lift Coefficient

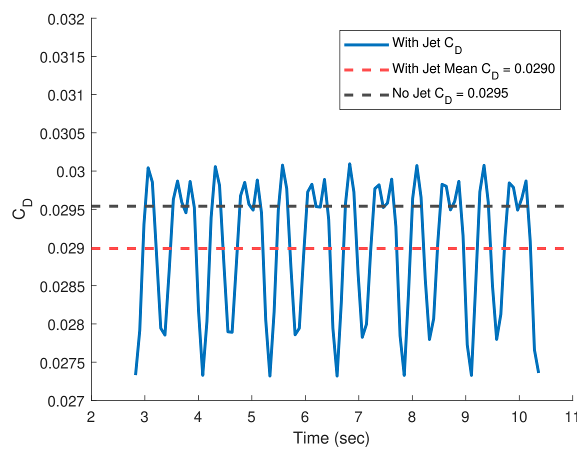

(b) Drag Coefficient

Figure 20: Aerodynamic Coefficients at $\alpha = 14°$ for F_{jet} = 0.8 Hz and A = 3.5

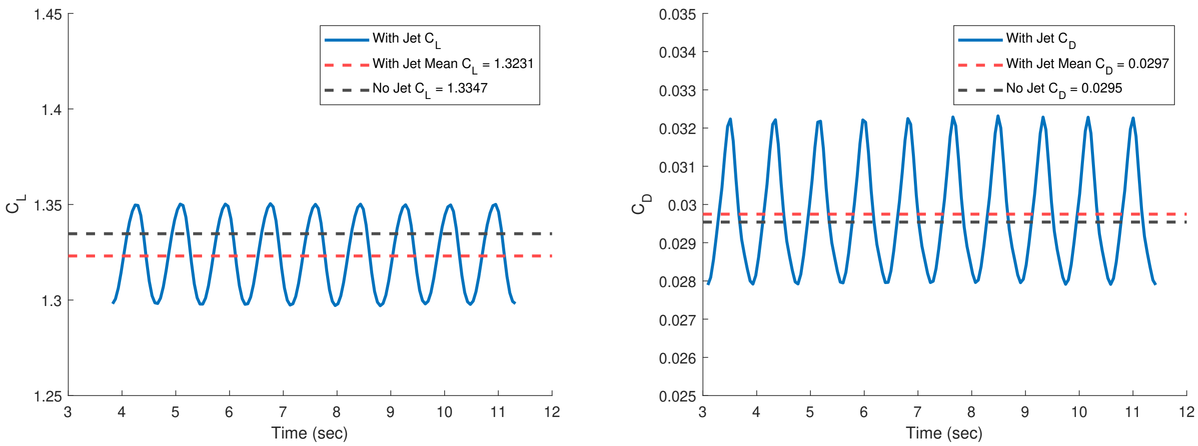

(a) Lift Coefficient **(b)** Drag Coefficient

Figure 21: Aerodynamic Coefficients at $\alpha = 14°$ for F_{jet} = 1.2 Hz and A = 2.0

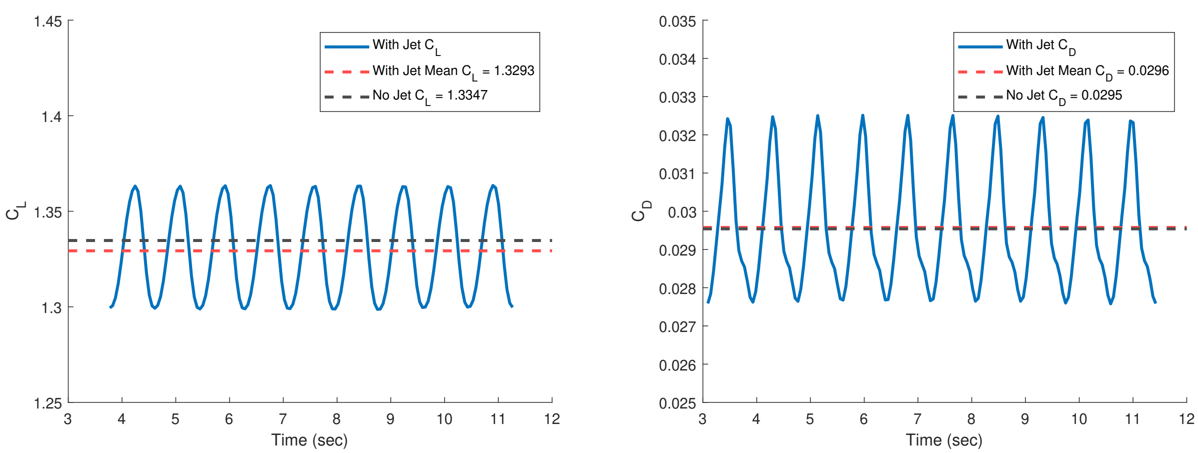

(a) Lift Coefficient **(b)** Drag Coefficient

Figure 22: Aerodynamic Coefficients at $\alpha = 14°$ for F_{jet} = 1.2 Hz and A = 2.5

h!]

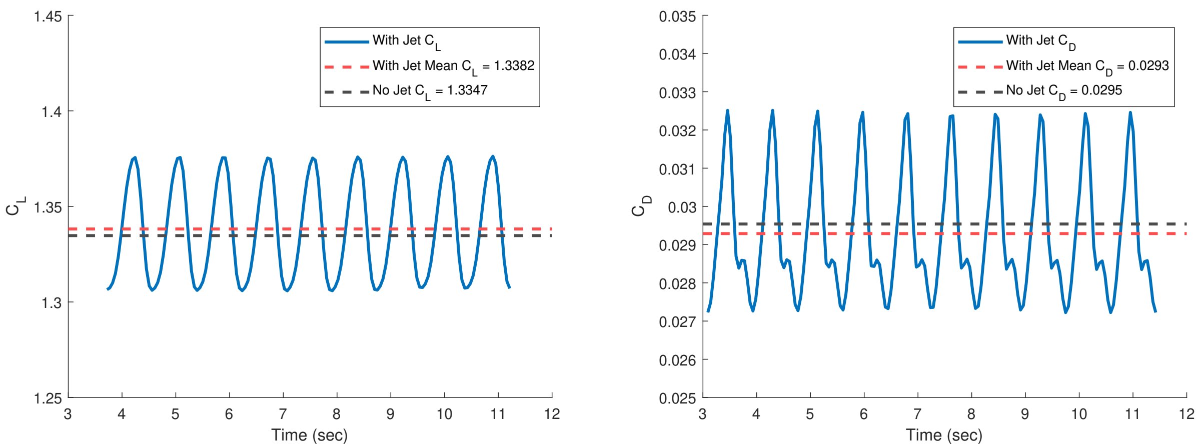

(a) Lift Coefficient **(b)** Drag Coefficient

Figure 23: Aerodynamic Coefficients at $\alpha = 14°$ for F_{jet} = 1.2 Hz and A = 3.0

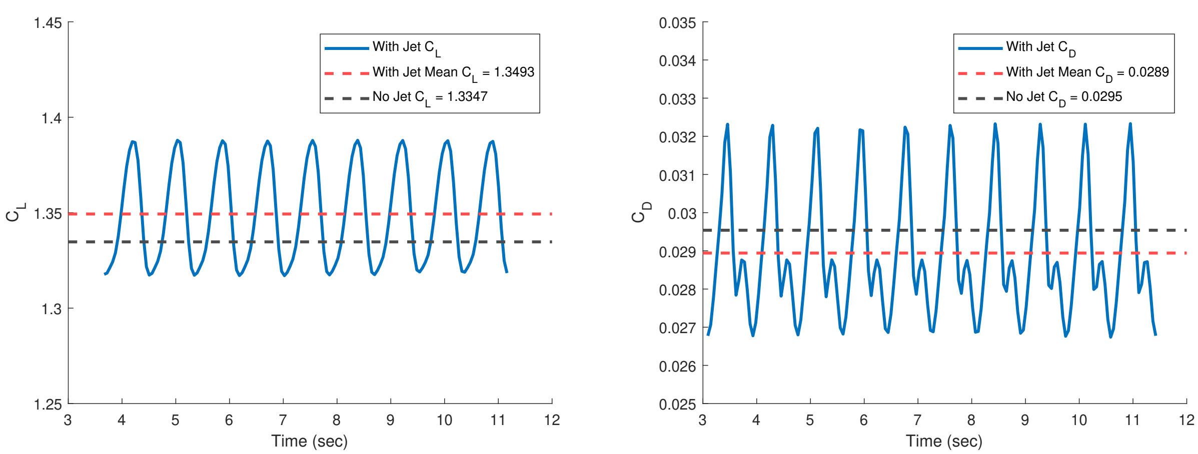

(a) Lift Coefficient **(b)** Drag Coefficient

Figure 24: Aerodynamic Coefficients at $\alpha = 14°$ for F_{jet} = 1.2 Hz and A = 3.5

Vita

Satyam Anil Mistry was born in Gujarat, India. In 2009, he and his family migrated to the United States, and ever since then, he has lived in Knoxville, Tennessee. At a young age, he was fascinated by airplanes and always wanted to learn how they fly. He attended Central High School, and upon graduating from there, he attended Pellissippi State Community College to earn his Associate of Science degree. He then transferred to the University of Tennessee, Knoxville to complete his Bachelor of Science in Aerospace Engineering. During his undergraduate studies, Satyam was introduced to computational fluid dynamics which became his research focus while he pursued a Master of Science in Aerospace Engineering under the guidance of Dr. Kivanc Ekici. After graduation, he plans to find a career in the industry focusing on computational fluid dynamics and aerodynamics. He is deeply grateful for all the support his mentors, family, and friends provided throughout his journey.